PERMANENT MAGNET SYNCHRONOUS MOTOR DRIVES FOR ELECTRIC VEHICLES

A DISSERTATION

Submitted in partial fulfilment of the
requirements for the award of the degree
of
MASTER OF TECHNOLOGY
in
ELECTRICAL ENGINEERING
(With Specialization in Power Apparatus and Electric Drives)

By

SIDDHAPURA KUMAN RANCHHODBHAI

DEPARTMENT OF ELECTRICAL ENGINEERING
INDIAN INSTITUTE OF TECHNOLOGY ROORKEE
ROORKEE-247 667 (INDIA)
JUNE, 2005

Candidate's Declaration

I hereby declare that the work, which is being presented in the dissertation, entitled **"Permanent Magnet Synchronous Motor Drives for Electric Vehicles"** in partial fulfillment of the requirements for the award of the degree of **Master of Technology** in Electrical Engineering with specialization in "Power Apparatus and Electric Drives", submitted in the Department of Electrical Engineering, Indian Institute of Technology, Roorkee, India is an authentic record of my own work carried out during the period from September 2004 to May 2005, under the supervision of Dipl.-Ing. Uwe Vollmer, Department of Electrical Energy Conversion, University of Stuttgart, Germany and kind guidance of Prof. Dr.-Ing. Uwe Schäfer, Head, Department of Electrical Energy Conversion, University of Stuttgart, Germany and Dr. Pramod Agrawal, Professor, Department of Electrical Engineering, Indian Institute of Technology, Roorkee, India.

The matter embodied in this dissertation has not been submitted by me for the award of any other degree or diploma.

Place: Stuttgart

Date: 09 May 2005

(Siddhapura Kuman Ranchhodbhai)

This is to certify that the above statement made by the candidate is correct to the best of our knowledge.

Dipl.-Ing. Uwe Vollmer
Department of Electrical Energy Conversion,
Inst. for Power Electronics and Electric Drives,
University of Stuttgart, 70569-Stuttgart,
Germany.

Prof. Dr.-Ing. Uwe Schäfer
Head,
Department of Electrical Energy Conversion,
Inst. for Power Electronics and Electric Drives,
University of Stuttgart, 70569-Stuttgart,
Germany.

Dr. Pramod Agrawal
Professor,
Department of Electrical Engineering,
Indian Institute of Technology,
Roorkee-247667,
India.

Acknowledgements

Abstract

Permanent magnet synchronous motor (PMSM) drives have been successfully developed to fulfil the special requirements for electric vehicles such as high power density, high starting torque and high cruising speed. The present thesis is based on three main topics; a design of permanent magnet synchronous motor, design verifications with finite element method and simulation of drives and control with constant torque and flux-weakening region.

Permanent magnet synchronous motor is designed for electric vehicles (EVs). The rotor configuration considered in this study is the inset/interior permanent magnet (IPM-spoke) type. An analytical software (SPEED) is used to design geometrical dimension of machine and to simulate the machine and drives static and dynamic behaviour. To verify design and get finer results, finite element method (FEM) software ANSYS is used for electromagnetic analysis. The designed PMSM model is transferred to finite element analysis (FEA) program. This work also deals with the coupling of the two software tool - SPEED and ANSYS. The coupling of simulation tools allows to simulate the behaviour of more complex geometries like that of a conventional electric machine. The simulation parameters depending on the geometry of the machine can be adjusted. The modelled machine's parameters, obtained from the analytical method and FEM, are compared and verified by experimental results.

To enable drive for electric vehicle application, a new current regulation control algorithm proposed that provides drives to operate in constant torque and flux-weakening region with optimum current. The control adjusts q- and d-axis current command based on commanded torque considering speed and dc link voltage. Time domain simulation of the behaviour of the drive including inverter with control algorithm is carried out in Matlab/Simulink. The designed parameter of the machine from analytical and FEM tool has been used in the time domain simulation. Simulation results are presented for the drives operating in low speed high torque, high speed and change in speed/torque conditions to demonstrate the drive performance with proposed control algorithm.

Table of Contents

List of Figures

Chapter 1

Introduction

1.1 Motivation and Objectives

The growing number of internal combustion engine vehicles (ICEV) increases the global air pollution. Furthermore the world's petroleum resources are limited. As a partial solution of the problem the alternative energy sources (e.g. LPG, CNG, and hydrogen) for conventional ICEV's are taken into account. The electric propulsion system is the other more promising technology, which appears in three main groups of electric vehicles (EV): Battery Electric Vehicles (BEV), Fuel Cell Electric Vehicles (FCEV) and Hybrid Electric Vehicles (HEV).

Electric motors, used in electric drive of an EV, should fulfill special requirements, such as: high power to weight ratio, high efficiency, wide field weakening range, high torque at standstill and at low speeds, regenerative braking possibilities, overload capability, ability to maintenance-free operation. In the new designed EV's the most prospective seems to be the permanent magnet synchronous motor (PMSM) - the AC version of permanent magnet motor (PMM). The advantages of PMSM compare to other types of motor are high and constant torque even at stillstand, high efficiency, wide speed range and better cooling conditions resulting from very low rotor losses; the main drawback is the relatively high cost. With the recent progress of permanent magnet performance, there is ever increasing attention to applying interior permanent magnet motors (IPMM) to electric vehicles for high efficiency and weight reduction.

The electric drive system of an electric vehicle is very important part of the EV. To implement the new system it is necessary to verify the complete system right from designing of machine to control strategy. With the advent of high speed digital computers, the analysis and design of complex drive systems are usually done using modern simulation software which can provide accurate predictions of the system's behaviour in reality. Consequently, computer modelling of such systems at a desired level of accuracy becomes an essential part of the design process. A satisfying system model usually serves as a prototype for the system behaviour simulations, as well as the small

signal analysis and control design. The computer-aided design has become indispensable for the electric machine design. In the practical designing, however, we have to consider many kinds of objective physical quantities to be improved simultaneously under the several constraints. Additionally, IPMM often has a complicated structure and the complex physical phenomena with magnetic saturation. Therefore finite element analysis (FEA) is used in this work for precise computation of the motor parameters and performance.

For the drive of an EV, this work has started with designing of PMSM; same design is verified with FEA. PMSM is required to operate in both constant torque and field weakening modes for an EV. The performance of PMSM drive with new control algorithm for constant torque and field weakening has been simulated with the designed machine parameter calculated from analytical and FEA methods. The proposed control adjusts q- and d-axis current reference toward the operating point with a reduced field magnitude along the constant torque curve. The q- and d-axis current reference moving along the constant torque curves in field weakening region to insure maximum torque production with varying voltage, which is normally the case in EV.

1.2   Literature Review

The complete thesis can divide in three different areas as following:

- Design of PMSM
- Finite Element Analysis of PMSM
- PMSM Drive

Literature is reviewed for each section and general guidelines are reviewed from the books [1-10]. Review of research papers for different section is discussed in the following sections.

1.2.1   Design of PMSM

Permanent magnet synchronous motor (PMSM) and Brushless DC motor (BLDC or BDCM) are most common terms used in the literature for permanent magnet motor (PMM). The PMSM and BDCM have many similarities; they both have permanent magnet (PM) on the rotor and require alternating stator current to produce constant torque. The difference in these two machines is that PMSM and the BDCM have

2

sinusoidal and trapezoidal back emfs, respectively [11]. Here in the present thesis, PMSM is taken for study because less torque ripple and higher speed range characteristic.

The paper by TJE Miller et al. [12] explains the calculation of torque in a brushless permanent-magnet line-start AC motor by means of the flux-MMF diagram in combination with the finite-element method. In [13] G.R. Slemon considers the major design factors which constrain the maximum acceleration capability of surface-mounted neodymium-iron-boron permanent magnet motors as used in servo drive. Expressions are derived for typical achievable values of the air-gap flux density and the linear current density around the stator periphery. The paper derives general approximate expressions for maximum torque and acceleration limits, and shows graphs from which the range of acceleration capability of a permanent magnet motor in a given application can be assessed.

Longya Xu et al. [14] proposes a new design concept of permanent magnet machine for flux weakening operation in which the feasibility of strong flux wakening capability without permanently demagnetizing the permanent magnet is investigated. Results from finite element analysis on the proposed PM machine structure are presented to verify the new design concept. The paper by Yong Li, Jibin Zou and Yongping Lu [15] deals with the optimum design of magnet shape in PMSMs. In order to improve the efficiency of PMSM, this is closely related to its magnet shape. A parallel top sine wave design gives to be an optimum plan is shown in the paper.

The paper [16] presents an unified approach to the analysis and design of an AC (Induction, reluctance or PM synchronous) motor drive able to meet a desired torque versus speed characteristics including a flux-weakening region. Field-weakening performance of interior permanent magnet (IPM) is explained in paper [17]. This paper presents theoretical and practical limitations to the field-weakening performance of surface permanent magnet, synchronous reluctance motor (SRM) and interior permanent magnet motors when driven from an inverter with a limited volt-ampere rating.

1.2.2 Finite Element Analysis of PMSM

Prediction of motor parameter and performance is necessary for evaluation of motor design. With advent of high-speed computing power and more powerful numerical methods in recent years, it has become to use finite-element methods (FEMs) to compute

the electrical machines in both steady state as well as under transient and dynamic condition. Numerical simulations of electrical machines will be based on fewer assumptions to give a higher accuracy at the expense of computing requirements.

Gyu-Hong Kang et al. [18], presents an investigation of the parameter modeling on the basis of an improved FEA in which the variable frequency characteristic in field weakening is considered in Interior Permanent Magnet Synchronous Motors (IPMSM). The parameters of IPMSM have a nonlinear characteristic under variable load conditions and due to the current phase angle in a system fed inverter have been verified using FEM.

In [19] and [20] M.A. Jabbar et al., discusses time-stepping FEA for the PMSM. Where electromagnetic field equation, the stator circuit equation, and the motion equation are solved simultaneously at each time step; so all the physical quantities relating to the circuit as well as the field solution has been taken in account simultaneously. A new outer-rotor PM brushless dc drive is designed and analyzed in [21]. To enable the drive applicable to electric vehicles, its transient performances at both normal and flux weakening operations are particularly focused. Whereas in [22], a new PM brushless dc machine with a unique feature of flux regulation is proposed. In this, the originality is that the air-gap flux of the machine is generated by both the PM excitation and the specially controlled stator current under the same PM pole.

S. L. Ho et al. in [23] describes a sub-block algorithm for the time-stepping finite element solution of problems in which sets of electromagnetic field equations, circuit equations and mechanical equation are coupled together for induction motor model. This algorithm is applicable to any machine and it also reduces the computational time. These are the main features of new algorithm. In [24], S. L. Ho et al. presents a time stepping finite element model for analyzing the performance of BDCM. Here, the control loop is coupled into the system equations and the eddy-currents in the PM are also taken into account in the circuit-field coupled method.

1.2.3 PMSM Drive

In the last few years, there has been a growing interest in the development of electric motor drives for electric vehicles. PMSM has numerous advantages over other machines that are conventionally used for AC drives. Particularly IPMSM becomes more popular because it has a mechanically robust construction, a rotor saliency, and the low

4

effective airgap. These features permit this machine to be operated not only in the constant torque region but also in the constant power region up to a high speed by flux weakening [3, 4, 5, 10]. The basic block diagram of PMSM drive is shown in Fig.1.1.
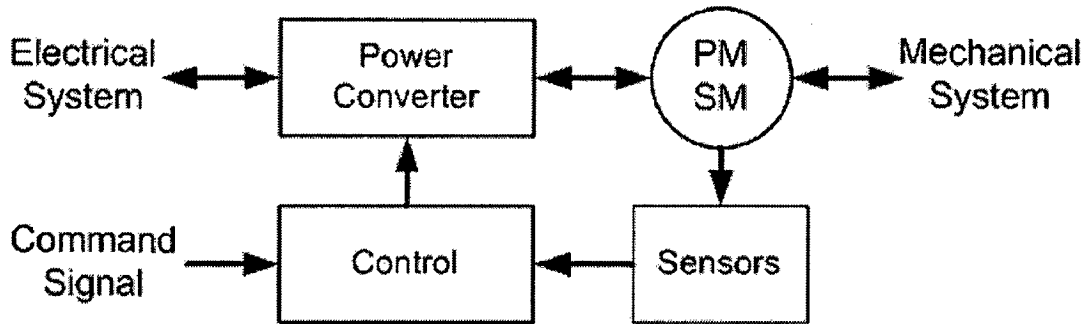
Fig. 1.1 PMSM Drive

G. Gallegos-Lopez et al. [25] proposes a novel current regulation algorithm for permanent magnet AC machines that provides maximum torque per ampere (MTPA) capability in the entire field weakened region. This algorithm provides robust current regulation with maximum efficiency and torque capability for permanent magnet AC machines despite significant changes in the voltage source and machine parameters. In [26], a field weakening technology of IPMM for the extended torque control capability has been proposed. This method controls the magnitude of flux according to the speed and dc link voltage without losing the ability to regulate the command torque. The control adjusts the q- and d-axis current reference toward the operating point with a reduced field magnitude along the constant torque curve.

B.K. Bose in [27] describes a high-performance fully operational four-quadrant control scheme for an interior PM synchronous machine. In this scheme, Control in the constant-torque region is based on the vector stator flux, whereas constant-power region control is implemented by orientation of torque angle of the impressed square-wave voltage through the feed forward vector rotator. The application of vector control to the PMSM and complete modelling, simulation, and analysis of the drive system is given in [28]. In this, state-space models of the motor and speed controller and real-time models of the inverter switches and vector controller are included.

Another flux-weakening scheme for IPMSM is proposed in [29]. This is implemented based on the output of the synchronous PI current regulator-reference voltage to the PWM inverter. The onset of flux weakening and flux level are adjusted

inherently by the outer voltage regulation loop to prevent saturation of current regulator. A DSP based torque control strategy for IPMSM with wide speed range has been discussed in [30]. Influence of DSP controller on performance of a permanent magnet brushless AC drive in flux-weakening mode provides in [31].

The paper by S. Morimoto et al. examines the current vector control method of PM motors to expand the operating limits considering the inverter capacity. This control method is optimum in the sense of deriving maximum output torque within the voltage and current constraints. The effects of motor parameters are examined by the computer simulation. Most of the drives are controlled by current-controlled voltage source inverter (VSI) systems. Because of its ease implementation, fast current control response and inherent peak current-limiting capability, hysteresis current control is considered as the simplest technique used to control the motor currents for an ac machine [32].

1.3   Outline of the Report

This master's thesis presents design and analysis of PMSM and control strategy of PMSM drives for electrical vehicles. This report is divided in 6 different chapters. The content of each chapter is outlined below.

Chapter 1, "Introduction," introduces the PMSM motor application for modern EVs. The recent research in PMSM design, analysis and drive has been discussed here in brief in literature review.

Chapter 2 is titled as "Modelling and Design of PMSM". Initial section of this chapter gives the background of permanent magnet material and properties of different permanent magnet material with BH characteristics. Next the basic rotor configuration used in PMSM is shown and q-d model of PMSM in rotor reference frame has derived. In last section, PMSM designed with analytical motor design software SPEED*.

Chapter 3, "Finite Element Analysis of PMSM", analyses the PMSM by finite element method with modern FEA software ANSYS. Initially the basic Maxwell's equation used for electromagnetic analysis discussed then PMSM is modelled mathema-

---

* SPEED (Scottish Power Electronic and Electric Drives) is analytical electromagnetic software for electric motor design developed by the SPEED Laboratory at Glasgow University, UK.

-tically and formulized for FEM. The general step by step method to simulate the FEA in modern software tool is given in the next section. The PMSM is modelled in FEA software and simulation results are shown in the last section.

Chapter 4, "Co-simulation-based Design", describes the utility of different software tools and interlinking of these tools. Initially, the basic design procedure used for the design is discussed where more than one tool has to be use is shown. In first part, fundamental of application manager is discussed. Later how SPEED and ANSYS are integrated in Matlab is shown for iterative simulations. Transfer of model from one tool to other is given in third section. Results of analytical tool, FEM tool and experimental are compared in the section 'Result Comparison'.

Chapter 5, "Simulation of PMSM Drive", starts with the basic philosophy behind the PMSM control and drive, where control of drive under constant torque and flux-weakening has been explained in section 5.2 with the use of constant torque loci, voltage limit ellipses and current limit circle. The control algorithm to operate drive in operational speed range is discussed in section 5.3 and in followed section, implementation of this algorithm in Matlab programming environment has been described with simulated results.

Chapter 6, "Conclusions and Future Work", concludes whole thesis with the design and analysis of PMSM and control algorithm. Work extensions and expectations are explained in future work.

7

Chapter 2

Modelling and Design of PMSM

2.1 Introduction

Along with the development of power electronics and magnetic materials, Permanent Magnet Synchronous Motors (PMSMs) are now widely used in many areas of modern industry. The PMSM servo systems have many advantages such as high efficiency, large peak torque, easy control of speed and reliable working characteristics. The structure of the motor is also simplified compared with an ordinary DC motor because of the use of permanent magnets. If equipped with an angle, speed, and/or current measuring element, a PMSM servo driving system can accomplish very accurate driving torque, speed, or position control.

There are several different configurations of PMSMs which use rotating permanent magnets and stationary phase coils. The main reason for so many different variations has to do with the utilization of different magnet grades in addition to wide range of applications. The motor designer has the control over several variables such as magnet material and configuration, the number of poles and the placement of winding. The choice of magnet type and rotor configuration is the some of the most fundamental design decision. Proper selection of magnetic material is important from both economical as well as performance consideration.

2.2 Permanent Magnet Materials

Advances in permanent magnetic materials over the last several years have had a dramatic impact on electric machines. Permanent magnet materials have special characteristics which must be taken into account in machine design. For example, the highest performance permanent magnets are brittle ceramics; some have chemical sensitivities, all have temperature sensitivity, and most have sensitivity to demagnetizing fields. Proper machine design requires understanding the materials well.

8

The portion of the curve of B-H loop in which permanent magnets are designed to operate in motors is the top left quadrant. This segment is referred to as the "demagnetizing curve" and is shown on the Fig 2.1. The remanent flux density B_r will be available if the magnet is short-circuited. However, with an air gap there will be some demagnetization resulting in the no-load operating point, which is crossover point of the characteristic and no load line. Slope of no-load line is smaller with a larger air gap. With current flowing in the stator, there is further demagnetization of the permanent magnet causing the operating point to shift to at full load.
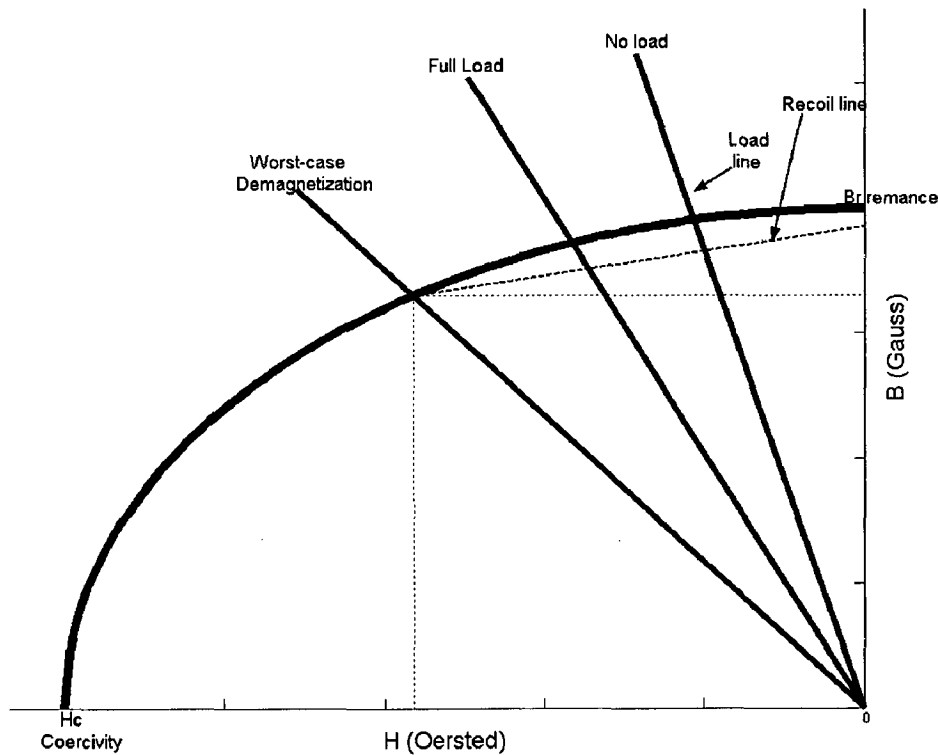
Fig 2.1 Permanent magnet machine operating points on B-H curve

There are three class of PMs currently used for electric motors:

- Alnico (Al, Ni, Co, Fe),

- Ceramics (ferrites), e.g. barium ferrite $BaO \times 6Fe_2O_3$ and strontium ferrites $SrO \times 6Fe_2O_3$,

- Rare-Earth materials, i.e. samarium-cobalt SmCo and neodymium-iron-boron NdFeB.

Demagnetization curves of the above PM materials are given in Fig 2.2 [03]. Alnico has high service temperature, good thermal stability, and high flux density, but the

disadvantage is low coercive force coupled with squarish B-H characteristics, which makes the permanent demagnetization high so that it is practically unsuitable for a PM machine.
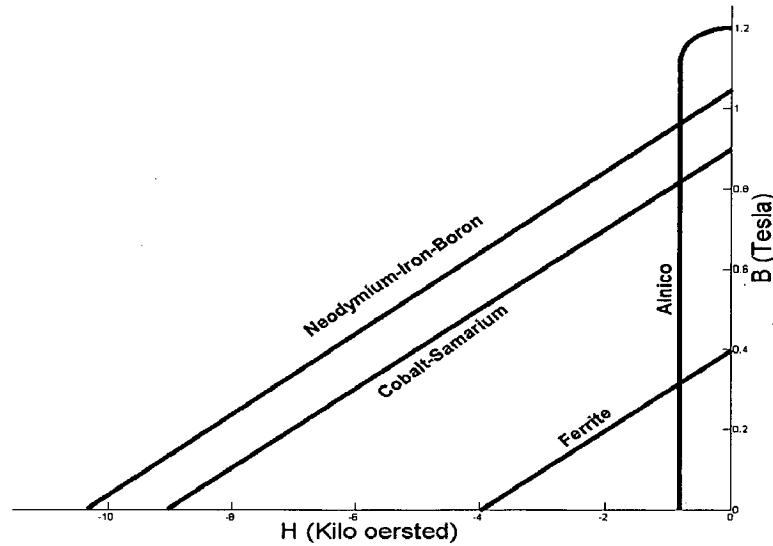
Fig 2.2   Permanent magnet characteristics

A brief summary of magnet properties is also given in Table 2.1. Barium and strontium ferrites are widely used as permanent magnet. Ferrites have the advantages of low cost and plentiful supply of raw material and are easy to produce. This magnet has practically linear demagnetization curve, but its remanence (B_r) is low. The Cobalt-Samarium magnet is made of iron, nickel, cobalt, and rare-Earth Samarium. It has the advantage of high remanence, high energy density defined by $(BH)_{max}$, and linear demagnetization characteristics. The service temperature is also high but the material is very expensive because of an inadequate supply of Samarium and Cobalt. The Neodymium-Iron-Boron magnet has highest energy density, highest remanence, and very good coercivity (H_{ci}). The disadvantages are low service temperature and susceptibility to oxidation unless protected by a coating. This material is expensive compared to ferrite, but because of high energy density, the machine weight is reduced. The application of Neodymium-iron-boron magnets is growing in PM machines.

The characteristic of all permanent magnet vary with temperature to a greater or lesser degree. Remanent flux density B_r of PM decreases with temperature. This effect is specified in terms of reversible temperature coefficient of B_r, specified in Table 2.1. The initial prediction that Nd-Fe-B materials would displace Ferrite in many applications has

10

not yet materialised. This is mainly due to the fact that Nd-Fe-B is more costly than ferrite and that current grades of Nd-Fe-B have a limited operating temperature range and are relatively susceptible to corrosion. These factors have helped ferrite to remain the magnet of choice for most of automotive applications, and rare-earth Sm-Co for most of aerospace application and high-performance servomotors [01]. However, Nd-Fe-B is also used in many motor applications where the corrosion is controlled by suitable coatings.

Table 2.1 Magnet Properties ($20\,^{\circ}C$)

Property	Units	Alnico	Ferrite	Sm-Co	Nd-Fe-B
Remanence B_r	T	0.6 to1.35	0.35 to 0.43	0.7 to 1.05	1.0 to 1.3
Intrinsic Coercivity H_{ci}	kA/m	40 to 130	180 to 400	800 to 1500	800 to 1900
Recoil Permeability μ_{rec}		1.9 to 7	1.05 to 1.15	1.02 to 1.07	1.04 to 1.1
$10^4\,(BH)_{max}$	kJ/m³	20 to 100	24 to 36	240 to 220	180 to 320
Magnetizing Force	kA/m	200 to 600	600 to 1700	1600 to 4000	2000 to 3000
Resistivity	μΩcm	47	$>10^4$	86	150
Thermal Expansion	$10^{-6}/^{\circ}C$	11.3	13	9	3.4
B_r Temperature coefficient	$\%/^{\circ}C$	-0.01 to -0.02	-0.2	-0.045 to -0.05	-0.08 to -0.15
H_{ci} Temperature coefficient	$\%/^{\circ}C$	-0.02	0.2 to 0.4	-0.2 to -0.25	-0.5 to -0.9
Max. working temperature	$^{\circ}C$	500 to 550	250	250 to 350	80 to 200
Curie temperature	$^{\circ}C$	850	450	700 to 800	310 to 350
Density	kg/m³	7300	4900	8200	7400

11

2.3 Permanent Magnet Synchronous Motor

2.3.1 Types of Rotor Configuration

There are numbers of rotor configurations are possible, typical configurations of rotor are shown in Fig. 2.3. The different rotor geometries make the PMSM divided into two types. They are exterior or surface permanent magnet motors (EPM motors) shown in Fig. 2.3 (a), (b) and interior or buried permanent magnet motors (IPM motors) shown in Fig. 2.3 (c), (d). Because of the electromagnetic and the mechanic constraints, the four architectures in Fig. 2.3 have different advantages and disadvantages when used in high-speed application.

(a) Surface $L_d = L_q$

(b) Inset $L_d < L_q$

(c) Spoke $L_d < L_q$

(d) Buried $L_d < L_q$
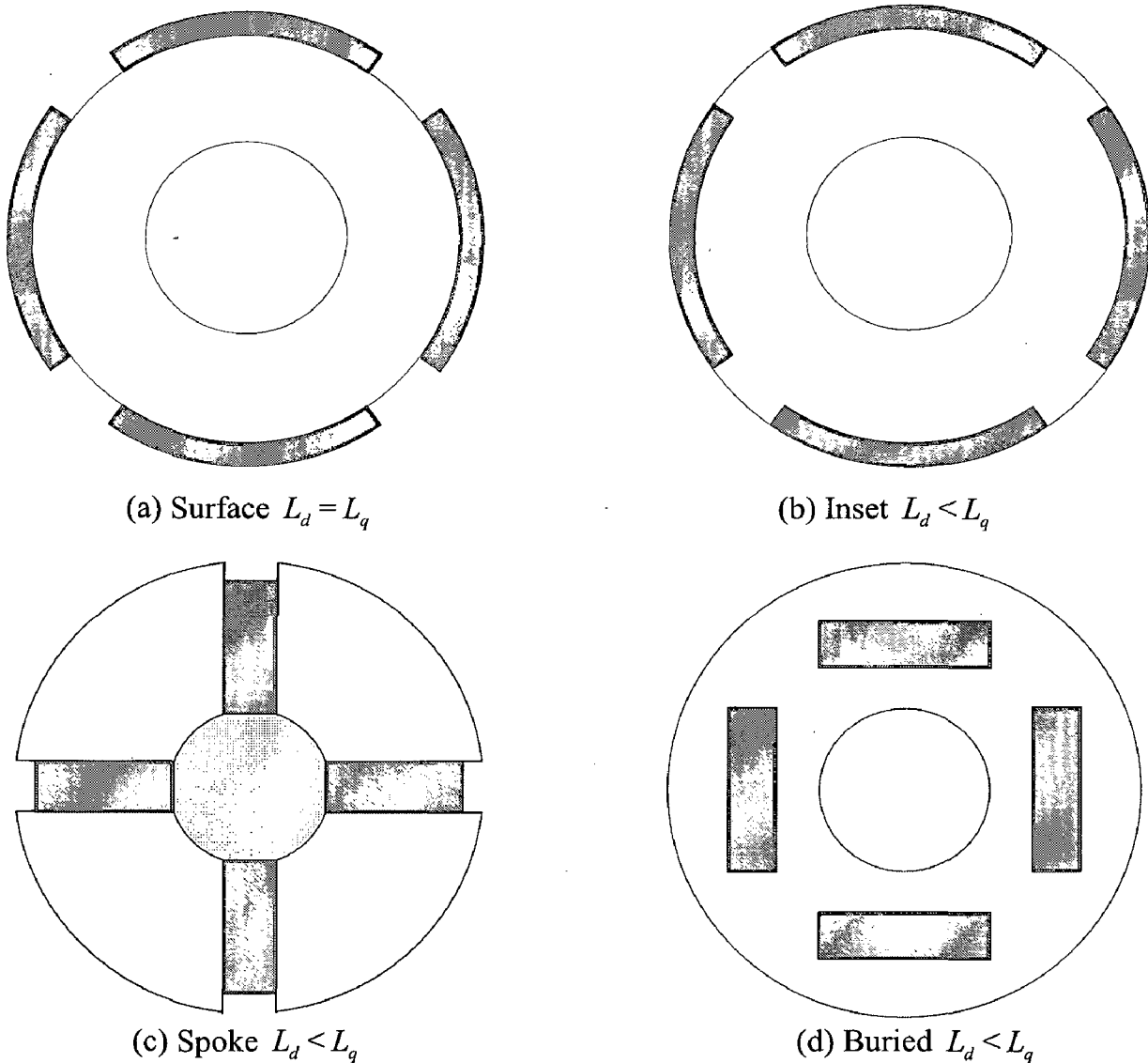
Fig. 2.3 Cross section of different rotor configuration

Exterior Permanent Magnet Motors (EPM)

In this machine, the stator has a 3-Φ sinusoidal winding as in induction motor, which creates a synchronously rotating air-gap flux. The Permanent Magnets (PMs) are glued on the rotor surface using epoxy adhesive or carbon fibre bandage is pressed onto rotor with force for high speed application. The rotor has an iron core, which may be solid or made of punched laminations for simplicity of manufacture. Line start motor may have a squirrel-cage winding to start as induction motor. Since relative permeability of PM is very close to one ($\mu_r > 1$), and magnets are mounted on the rotor surface, the effective air gap of the machine is large and machine is nonsalient pole ($L_{md} = L_{mq}$). This contributes to a low armature reaction effect due to low magnetizing inductance.

Interior Permanent Magnet Motors (IPM)

Unlike an EPM, in an interior permanent magnet motors, the magnets are mounted inside the rotor. The stator has usual 3-Φ sinusoidal winding. The difference in the geometry gives the following characteristics to the IPM machine: (1) the machine is more robust permitting a much higher speed of operation, (2) the effective air gap in the d^e- axis is larger than that in the q^e-axis, which makes the machine a salient pole with $L_{md} < L_{mq}$ (unlike a standard wound field synchronous machine (SM)) , and (3) with the effective air gap being low, the armature reaction effect becomes dominant [3].

Table 2.2 Comparison of EPM and IPM rotor configuration

	EPM		IPM	
	Surface	**Inset**	**Spoke**	**Buried**
Saliency	$L_d = L_q$	$L_d < L_q$	$L_d < L_q$	$L_d < L_q$
Airgap Flux Density	$B_{gap} < B_{residual}$	$B_{gap} < B_{residual}$	$B_{gap} > B_{residual}$	$B_{gap} < B_{residual}$

2.3.2 Machine Model in Rotor Reference Frame

The stator of the PMSM and the wound rotor SM are similar. The permanent magnets used in the PMSM are of a modern rare-earth variety with high resistivity, so induced currents in the rotor are negligible. In addition, there is no difference between the

13

back EMF produced by a permanent magnet and that produced by an excited coil. Hence the mathematical model of a PMSM is similar to that of the wound rotor SM. The following assumptions are made in the derivation.

1) Saturation is neglected although it can be taken into account by parameter changes.

2) The induced EMF is sinusoidal.

3) Eddy currents and hysteresis losses are negligible.

4) There are no field current dynamics.

5) There is no cage on the rotor.

With these assumptions, the stator d-q equations of the PMSM in the rotor reference frame are

$$V_{qs}^r = r_s i_{qs}^r + p\lambda_{qs}^r + \omega_r \lambda_{ds}^r \tag{2.1}$$

$$V_{ds}^r = r_s i_{ds}^r + p\lambda_{ds}^r - \omega_r \lambda_{qs}^r \tag{2.2}$$

$$V_{0s}^r = r_s i_{0s}^r + p\lambda_{0s}^r \tag{2.3}$$

where,

$$\lambda_{qs}^r = L_q i_{qs}^r \tag{2.4}$$

$$\lambda_{ds}^r = L_d i_{ds}^r + \lambda_m^{'r} \tag{2.5}$$

$$\lambda_{0s}^r = L_{ls} i_{0s}^r \tag{2.6}$$

$$\omega_r = \frac{d\theta_r}{dt} \tag{2.7}$$

$$L_q = L_{ls} + L_{mq} \quad \text{and} \quad L_d = L_{ls} + L_{md}$$

V_{qs}^r and V_{ds}^r are the q-, d-axis voltage in rotor reference frame, i_{qs}^r and i_{ds}^r are the q , d axis current in rotor reference frame, L_q and L_d are the q, d axis inductances, λ_{qs}^r and λ_{ds}^r are the q-, d-axis stator flux linkages in rotor reference frame, r_s stator resistance, $\lambda_m^{'r}$ flux linkage due to the rotor magnet linking the stator, L_{mq} and L_{md} are the q-, d-axis mutual inductances, L_{ls} leakage inductance and ω_r rotor frequency.

The equation (2.1), (2.2) and (2.3) can be written in matrix form as

$$V_{qd0s}^r = r_s i_{qd0s}^r + \omega_r \lambda_{dqs}^r + p\omega_r \lambda_{qd0s}^r \tag{2.8}$$

14

where,

$$(\lambda_{dqs}^r)^T = \begin{bmatrix} \lambda_{ds}^r & -\lambda_{qs}^r & 0 \end{bmatrix} \tag{2.9}$$

$$\lambda_{qd0s}^r = \begin{bmatrix} L_{ls} + L_{mq} & 0 & 0 \\ 0 & L_{ls} + L_{md} & 0 \\ 0 & 0 & L_{ls} \end{bmatrix} \begin{bmatrix} i_{qs}^r \\ i_{ds}^r \\ i_{0s}^r \end{bmatrix} + \lambda_m^{'r} \begin{bmatrix} 0 \\ 1 \\ 0 \end{bmatrix} \tag{2.10}$$

Substituting equation (2.4) – (2.6) in equation (2.1) – (2.3) and $p\lambda_m^{'r} = 0$ (considering magnet flux linkage remains constant), we can write,

$$V_{qs}^r = (r_s + pL_q)i_{qs}^r + \omega_r L_d i_{ds}^r + \omega_r \lambda_m^{'r} \tag{2.11}$$

$$V_{ds}^r = (r_s + pL_d)i_{ds}^r - \omega_r L_q i_{qs}^r \tag{2.12}$$

$$V_{0s}^r = (r_s + pL_{ls})i_{0s}^r \tag{2.13}$$

The voltage and flux linkage equations suggest the equivalent circuits shown in Fig. 2.4.

(a)

(b)

15

(c)
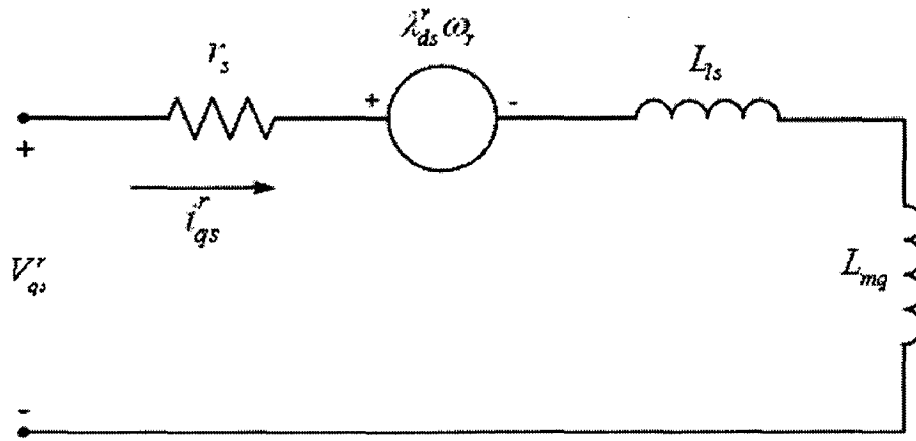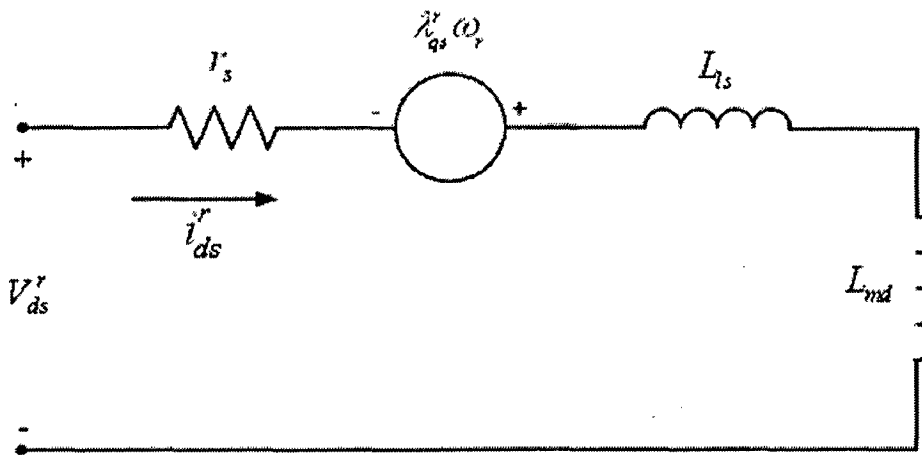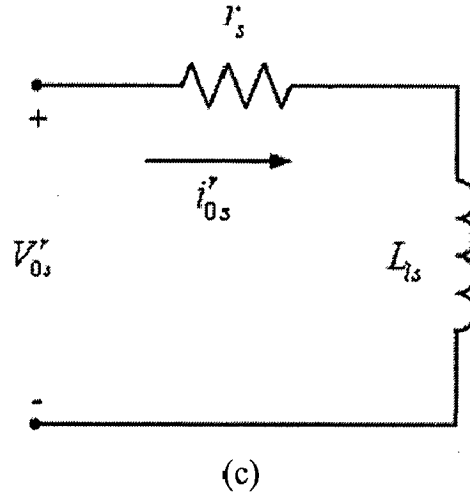
Fig. 2.4 Equivalent circuit of permanent magnet synchronous motor in rotor reference frame: Park's equation

The expression for the electromagnetic torque can be written as,

$$T_e = \left(\frac{3}{2}\right)\left(\frac{P}{2}\right)(\lambda_{ds}^r i_{qs}^r - \lambda_{qs}^r i_{ds}^r) \tag{2.14}$$

rewriting above equation as,

$$T_e = \left(\frac{3}{2}\right)\left(\frac{P}{2}\right)(\lambda_m^{'r} i_{qs}^r - (L_q - L_d)i_{qs}^r i_{ds}^r) \tag{2.15}$$

and the equation for the motor dynamics is

$$T_e = T_L + B\omega_r + Jp\omega_r \tag{2.16}$$

In the above equations P is total number of poles, T_e is electromagnetic torque, T_L is load torque, B is damping coefficient and J is moment of inertia.

The inverter frequency is related to the rotor speed as

$$\omega_i = \left(\frac{P}{2}\right)\omega_r \tag{2.17}$$

For dynamic simulation, the equations of the PMSM presented in (2.10)-(2.12) must be expressed in state-space form as shown in below

$$pi_{qs}^r = (V_{qs}^r - r_s i_{qs}^r - \omega_r L_d i_{ds}^r - \omega_r \lambda_m^{'r})/L_q \tag{2.18}$$

$$pi_{ds}^r = (V_{ds}^r - r_s i_{ds}^r + \omega_r L_q i_{qs}^r)/L_d \tag{2.19}$$

$$p\omega_r = (T_e - T_L - B\omega_r)/J \tag{2.20}$$

The d-q variables are obtained from a, b, c variables through Park transform as defined below:

$$f_{qd0s} = K_s f_{abcs}$$ (2.21)

where,

$$(f_{qd0s})^T = \begin{bmatrix} f_{qs} & f_{ds} & f_{0s} \end{bmatrix}$$ (2.22)

$$(f_{abcs})^T = \begin{bmatrix} f_{as} & f_{bs} & f_{cs} \end{bmatrix}$$ (2.23)

$$K_s = \frac{2}{3} \begin{bmatrix} \cos(\theta) & \cos\left(\theta - \frac{2\pi}{3}\right) & \cos\left(\theta + \frac{2\pi}{3}\right) \\ \sin(\theta) & \sin\left(\theta - \frac{2\pi}{3}\right) & \sin\left(\theta + \frac{2\pi}{3}\right) \\ \frac{1}{2} & \frac{1}{2} & \frac{1}{2} \end{bmatrix}$$ (2.24)

It can be shown that for the inverse transformation we have

$$(K_s)^{-1} = \begin{bmatrix} \cos(\theta) & \sin(\theta) & 1 \\ \cos\left(\theta - \frac{2\pi}{3}\right) & \sin\left(\theta - \frac{2\pi}{3}\right) & 1 \\ \cos\left(\theta + \frac{2\pi}{3}\right) & \sin\left(\theta + \frac{2\pi}{3}\right) & 1 \end{bmatrix}$$ (2.25)

In the above equations, f can represents either voltage, current, flux linkage, or electric charge. The subscript T denotes the transpose of a matrix. The s subscript indicates the variables, parameters, and transformation associated with stationary circuits.

The total instantaneous input power to the machine in terms of the a, b, c variable may be expressed as

$$P_{abcs} = v_{as}i_{as} + v_{bs}i_{bs} + v_{cs}i_{cs}$$ (2.26)

This can be written in q, d variables for 3-Φ balance system as

$$P_{qds} = \frac{3}{2}(v_{qs}i_{qs} + v_{ds}i_{ds})$$ (2.27)

2.4 Design of PMSM

A PMSM motor is made available with the specification 37 kW, 9000 rpm, 8 poles which has the stator core of induction motor IEC 160/8.170. The motor was designed using SPEED software tool. The Basic design steps are discussed below.

2.4.1 Basic design steps

Before PMSM design begins, several important decisions have to be made. A step-by-step procedure is provided as a rough guide for a typical PMSM motor design.

01.   Determine application requirements

02.   Interior-rotor, exterior-rotor, or axial-gap configuration?

03.   Select magnet grade

04.   Select number of poles

05.   Number of slots and phases

06.   Perform rough sizing estimate

07.   Select air gap length and determine magnetic loading

08.   Design rotor and determine flux/pole

09.   Lay out of stator laminations

10.   Calculate numbers of conductors and turns/coil

11.   Calculate wire size, resistance and inductance/phase

12.   Calculate performance

13.   Check temperature rise, current density, flux densities, demagnetisation

14.   Modify design and reiterate until objectives are met

PC-BDC 6.5 of SPEED software has been used here to the design PMSM. The basic rotor type chosen here is so-called spoke type where magnets are mounted inside the rotor which gives a more robust performance of the machine, permitting a much higher speed of operation which is required for electric vehicles.

2.4.2 Machine Specification

The design specifications for the PMSM comprise of the required power output P_{kw} in kw, speed n in rps, allowable peak phase current I_S in Amps, and available dc supply voltage at dc link is V_{DC} in volts for the system. Knowing the speed and power output will automatically fix the torque to be developed by the machine as

18

$$T_{req} = \frac{P_{kw}}{2\pi n} \, N.m \qquad\qquad (2.28)$$

2.4.3 Stator Geometry

When the design procedure of a PMSM is started, a good starting point as regards the physical dimensions of the machine would be a comparison with an equivalent induction motor [IEC 160/8.170]. A comparison with an equivalent induction motor will fix the frame size of the PMSM to be designed. This is advantageous as in many applications, a PMSM may be used to replace other machines. The IEC standards fixes dimensions for all electrical machines made internationally according to the International Standards Organization (ISO) regulations. During the progression of the design, if the machine size is found to be too large or too small, a different frame size can be used. The preliminary selection of frame size automatically fixes the outer diameter of the stator.

The PMSM design in this study is based on the existing induction motor stator geometry IEC 160/8.170, the stator outside diameter is 240mm and the machine active length is 200mm. The induction motor 2D geometry is shown in Fig. 2.5. The steel material quality type is M330-35A ISOL20 can be referred in Appendix A.
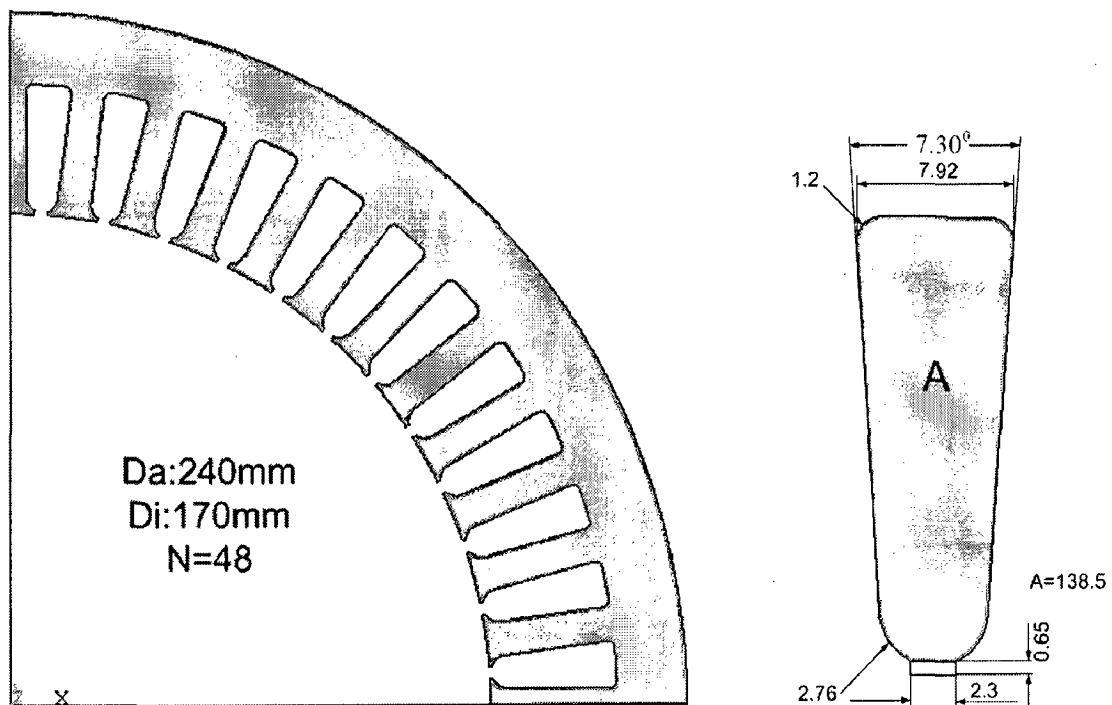
Fig. 2.5 2D Stator Lamination Geometry and slot dimensions

2.4.4 Number of Pole Selection

After deciding stator geometry dimension, first step in rotor design is the number of pole selection. There are many possible combinations for the number of poles. The advantages and disadvantages have been explored in detail in [01]. For the fixed number of slot and fixed number of phase, there will be fix number of pole will suited for PMSM rotor. In this case, for 48 numbers of slots and 3-Φ, the possible numbers of poles combinations are 2, 4, 8, 10, 14, 16, 20, 32, 34, 38, and 40. The next step would be selecting one of the combinations out of possible combinations. For this winding pitch and minimum cogging torque combination [01] can be helpful to decide proper number of poles. Here selecting one of popular combination of poles 8 with 48 numbers of slots.

2.4.5 Winding

The winding of brushless permanent-magnet with interior rotors can be similar to those of three-phase induction motors, including lap winding and concentric windings. In present case, considering single layer winding with full pitch as shown Fig 2.6. In the design, there are total 24 coils so 8 coils/phase. The each coil has 4 turns which means 4 conductors/slot. Each conductor side is stranded with 14 conductors of 0.710mm diameter and 18 conductors of 0.750mm diameter, which can be considered as a single conductor of 4.1452mm diameter.
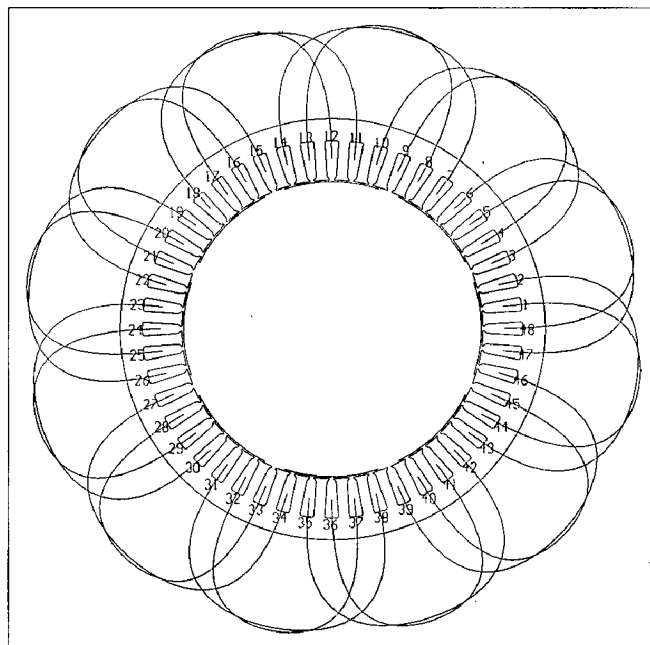
Fig 2.6 Winding layout of all three phase

2.4.6 Magnet Material and Rotor Core

As a DC Motor, the induced voltage E and the electromagnetic torque can be related with speed and current as follows:

$$E = k_E N \tag{2.29}$$

$$T_e = k_T I_a \tag{2.30}$$

So, focusing on to the how to obtain a higher torque coefficient to same motor dimensions and limited electromagnetic torque. To a large extent, the characteristic of a PMSM depends on the amplitude and waveform of its induced voltage in the stator winding, and the waveform is directly determined by the gap magnetic field. Indirectly one should try to increase k_E and k_T at the design stage. Considering these things and as mentioned above about advantage of interior permanent magnet as a rotor configuration in which flux is concentrated in airgap, which means flux density will be higher in the gap than in the magnet. The stator core is used of induction motor so it should be designed for lower flux density with this lamination, selecting magnet type of Ferrite material of HF 28/26 type which is also cheaper than other rare-earth magnet materials. The magnet material HF 28/26 characteristic is shown in Appendix A. Rotor core is considered as same stator metal steel quality. With this rotor configuration and magnet type, the designed stator and rotor geometry in SPEED is shown in Fig. 2.7
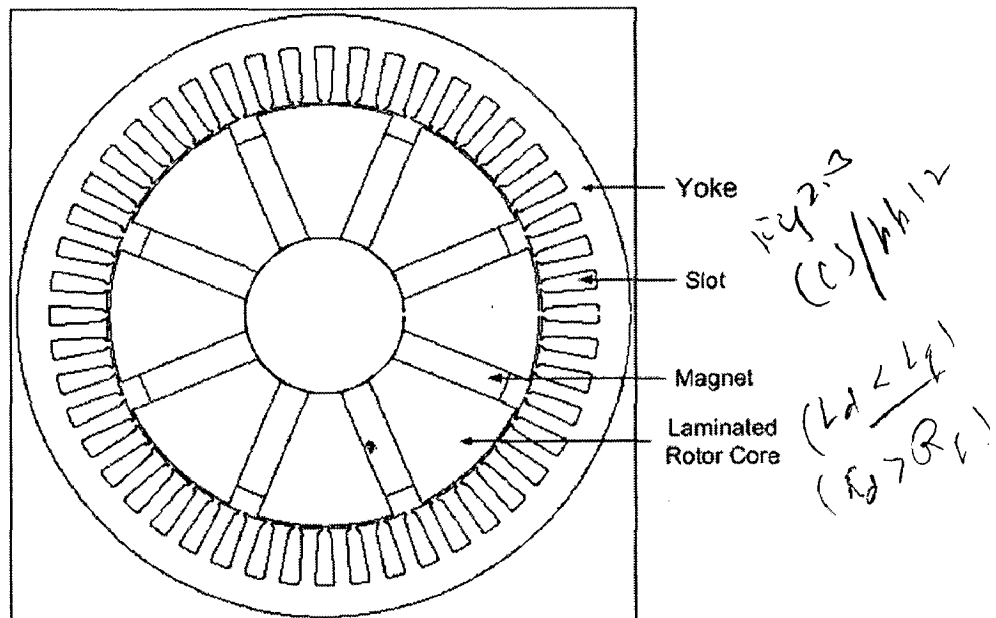
Fig. 2.7 Cross sectional view stator and rotor geometry

2.4.7 Armature Reaction and Demagnetization

Current flowing in the stator tends to distort the magnetic field set up by the permanent magnets. The larger the stator current, the larger the distortion of the field. In DC motors this effect is known as armature reaction. In EPM this effect is weak, however in IPM the distortion due to stator current is higher. This effect is calculated more accurately using FEM in chapter 3.

2.4.8 Analytical Design Output

The geometrical dimension of stator and rotor of the designed machine is shown in Table 2.3. The calculation is based on analytical software tool in which static simulation has been performed and some of the results are also shown in Fig. 2.8. The complete design sheet can be referred in Appendix B.

Table 2.3

Stator Data	
Stator Lamination OD (StatorOD)	240.00 mm
Stator Lamination ID (StatorID)	170.00 mm
Radial thickness of Stator Yoke (SYoke)	12.5 mm
Stator tooth width (TWS)	6.152 mm
Slot opening depth (TGD)	0.650
Slot bottom fillet radius (filSB)	1.2 mm
Stack length (Lstk)	200.00 mm
Lamination Stacking factor (Stf)	0.970
Stator skew [slot pitch] (Skew)	1.60

Rotor Data	
Rotor OD (RotorOD)	168.00 mm
Length of Magnet (LM)	12.00 mm
Width of Magnet (MagWid)	45.00 mm
Radial thickness of Rotor Yoke (RYoke)	23.57 mm
Magnet inset (Inset)	7.685 mm
Slits	none
Effective rotor length (Lrotor)	200.00 mm
Poles	8
Pole arc/pole pitch ratio (pupa)	0.818

Current vs. Rotor position

(a)

E.M.F. vs Rotor position

(b)

23

Torque vs Rotor position

(c)

Airgap Magnet Flux-density
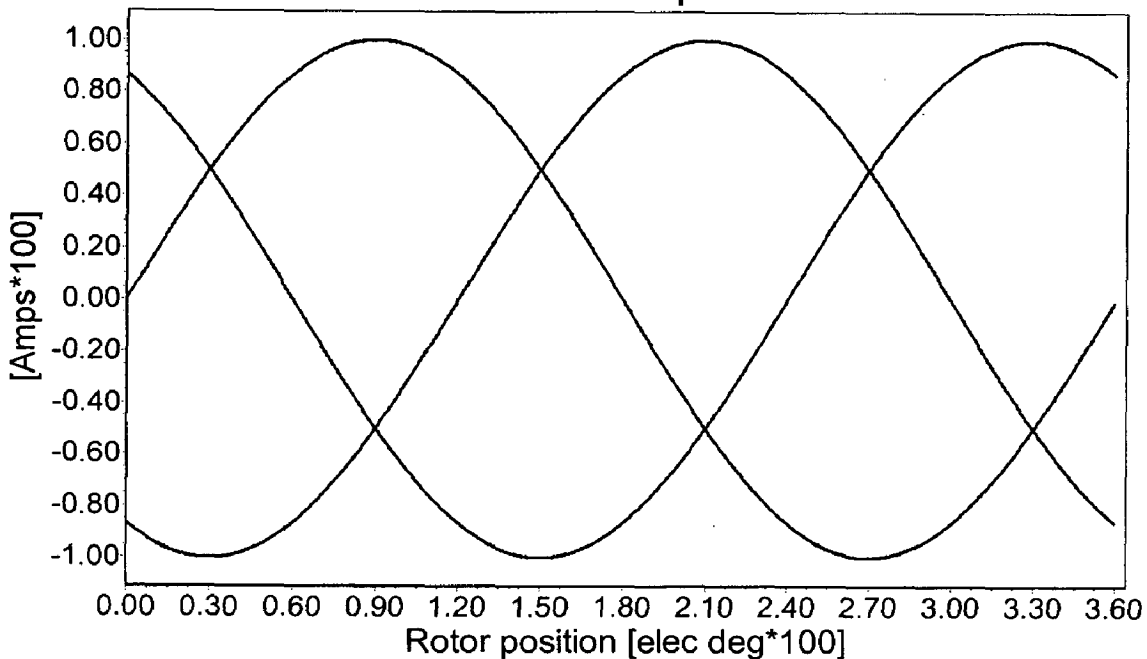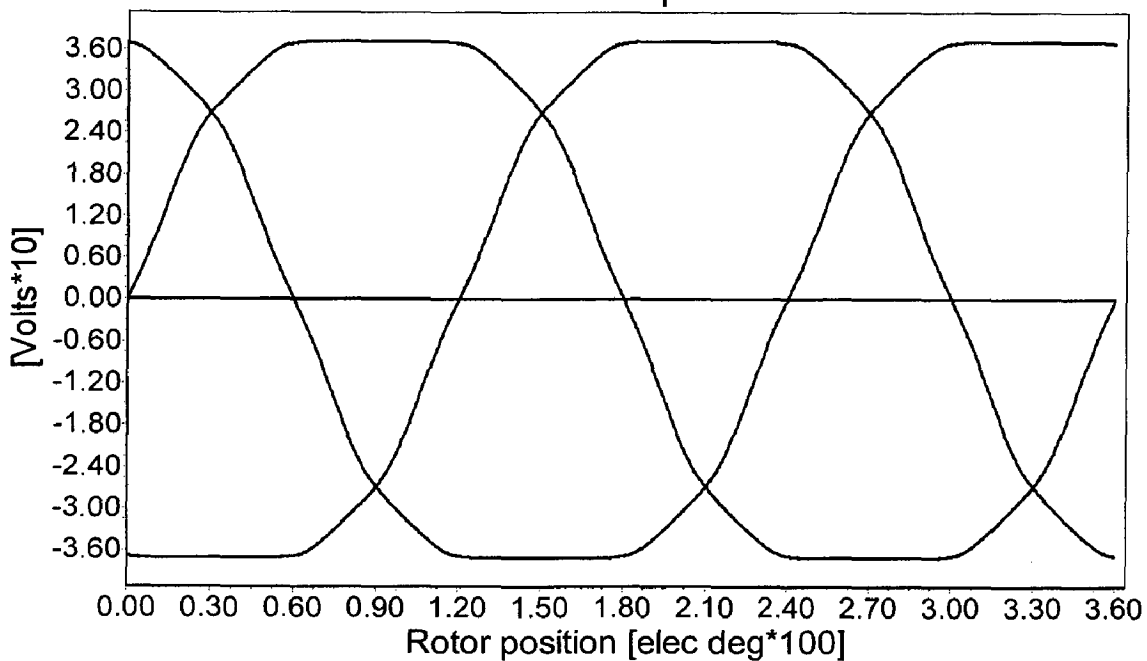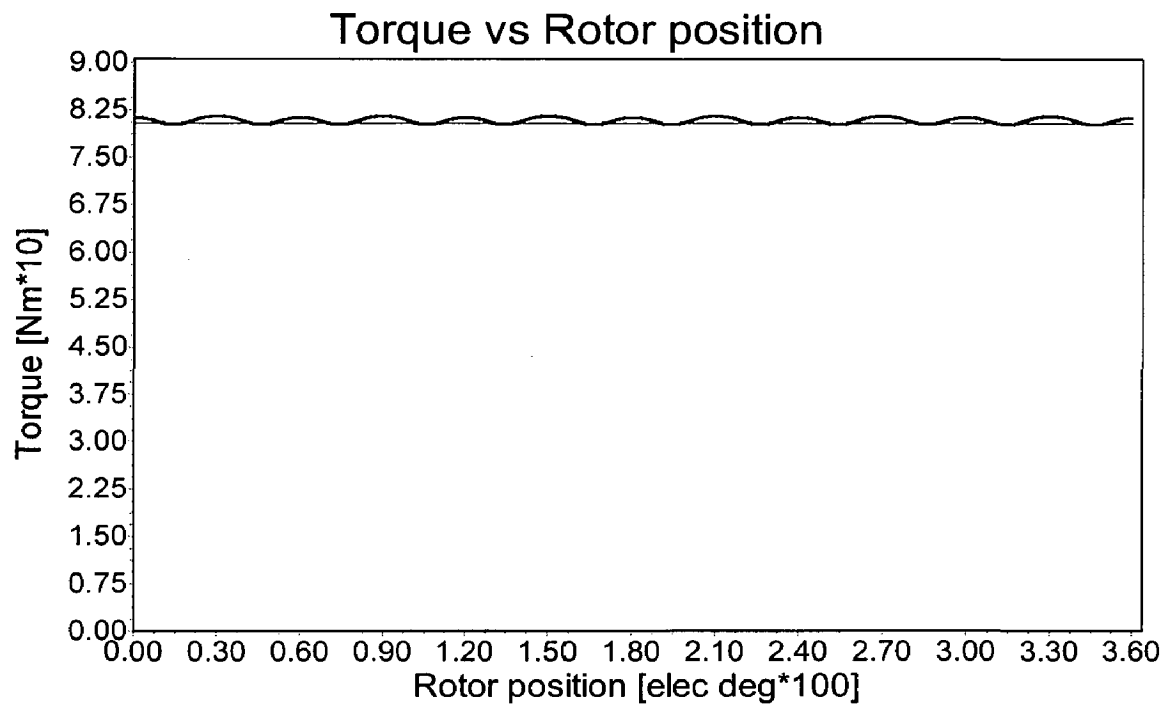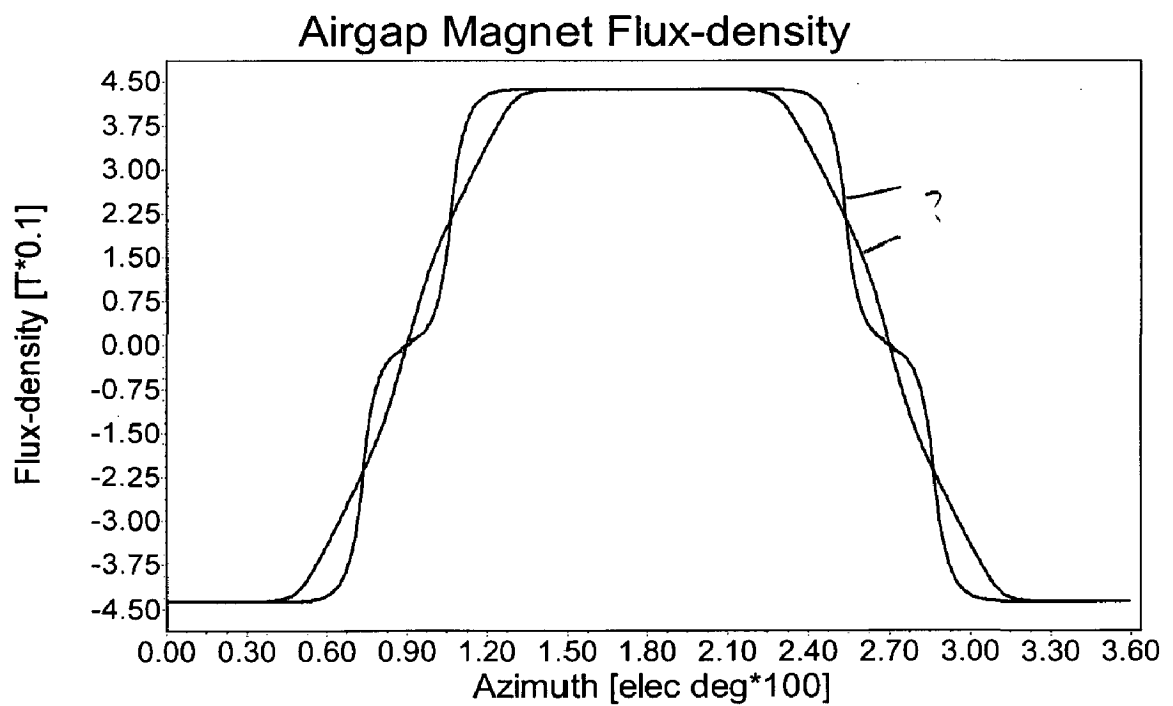
(d)

Fig. 2.8 Static simulation result output of current, voltage, torque and flux-density Vs rotor position (electrical degree)

(a)   (b)
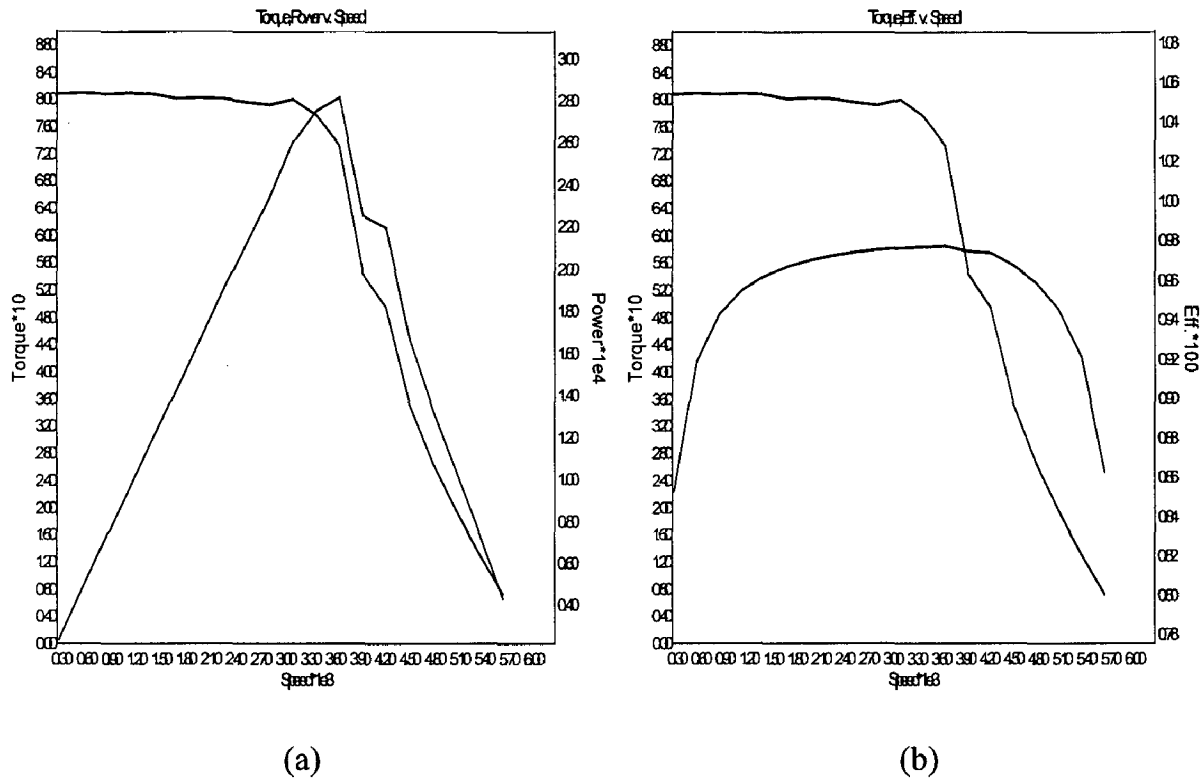
Fig. 2.9 Simulation result output of torque, power and efficiency Vs speed

2.4.9 Parameter Study

As mentioned previously, the possibility of using an existing induction motor stator geometry is explored in this study. The winding of PMSM is also being similar to the 3-Φ induction motor. Once the basic design has been completed, then, the parameter variations are observed using simulations in SPEED. During simulation, main focus has been placed on the variation of following geometric parameters variations.

a)   Airgap variation

b)   Magnet width variation

c)   BetaM (pole arc) variation

d)   Shaft radius variation

Here, the varying parameters variation simulation has been done through the interlinking with Matlab, which is explained in chapter 4. The influences of these parameters on the performance characteristic like torque, airgap flux density, and inductances are illustrated in following figures.

(a) Airgap variation

(b) Magnet width variation

26
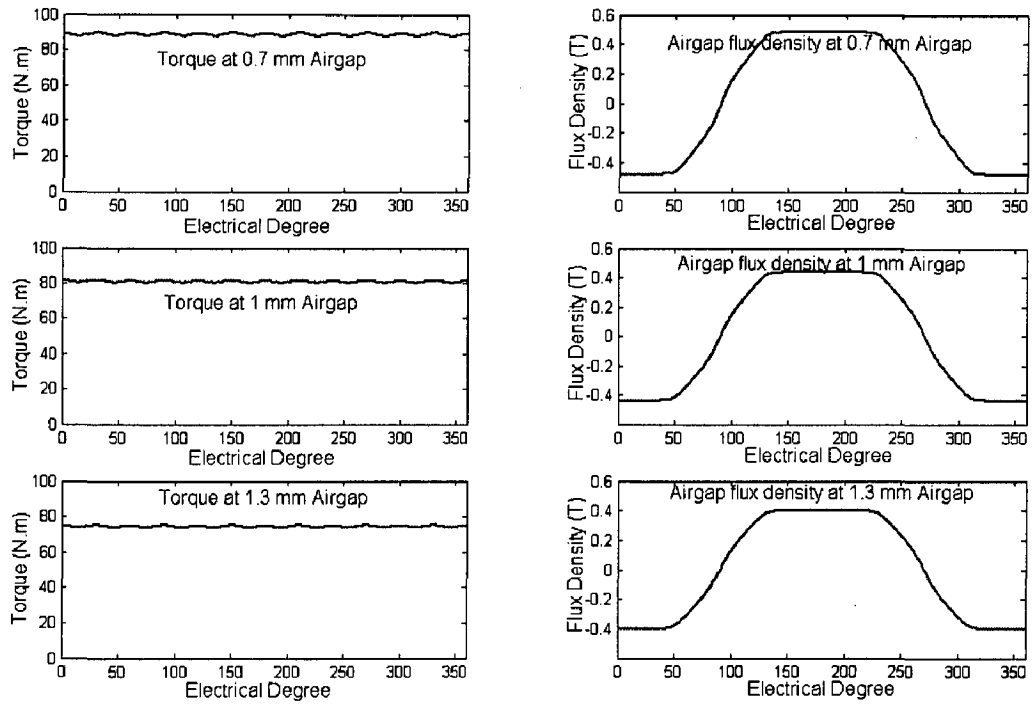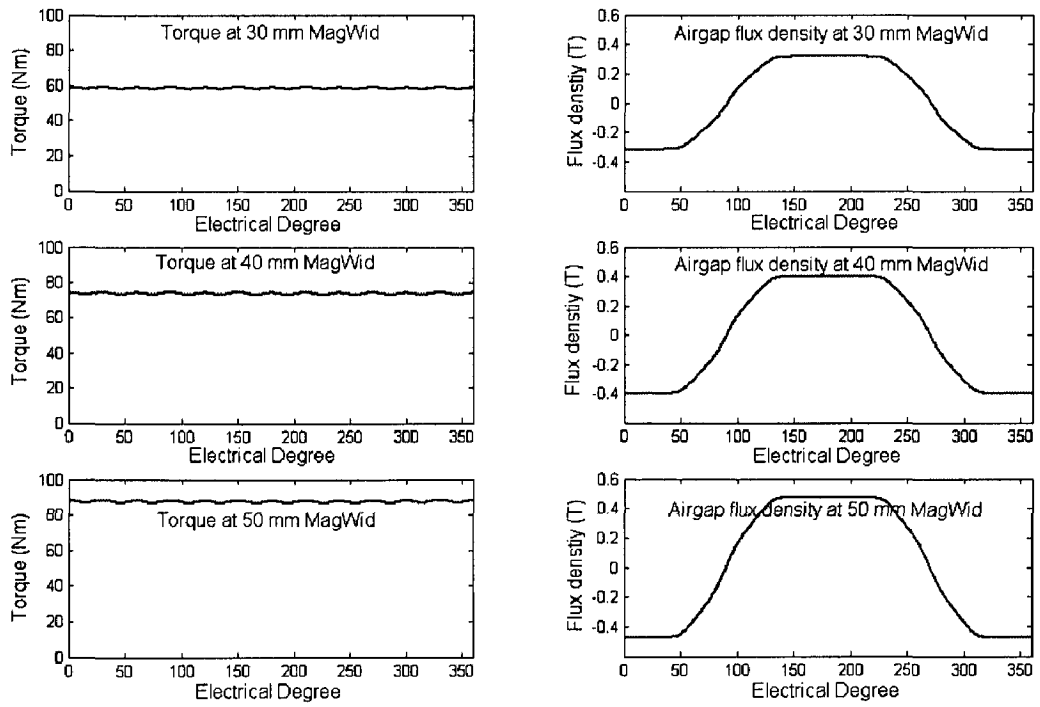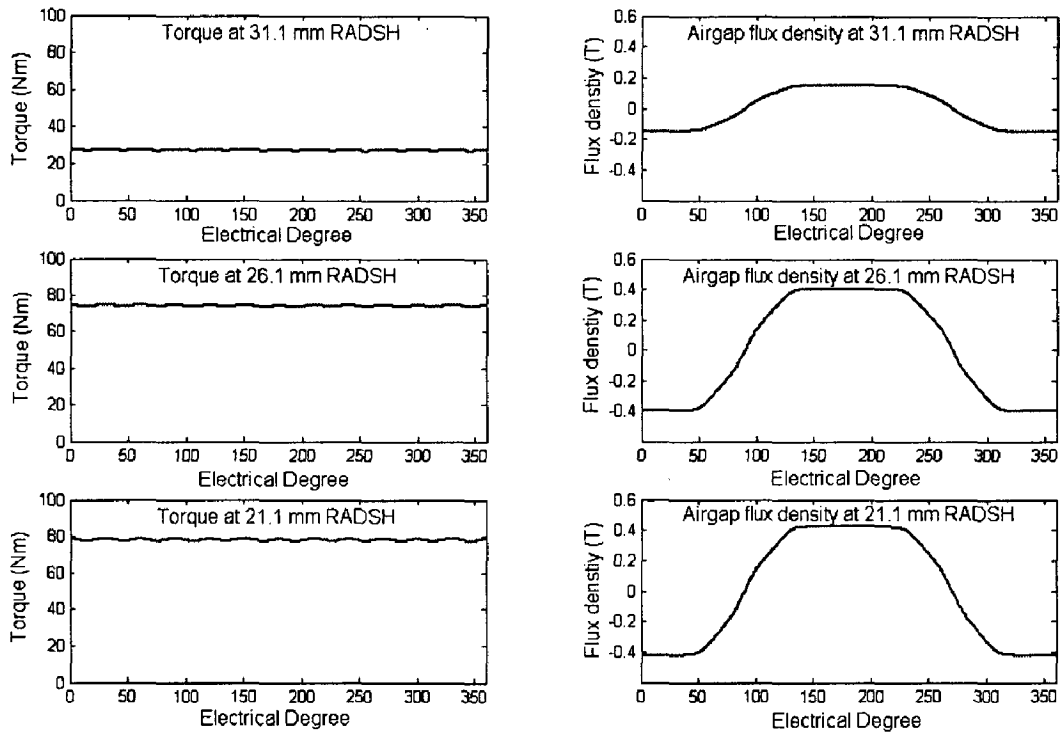
(c) Shaft radius variation
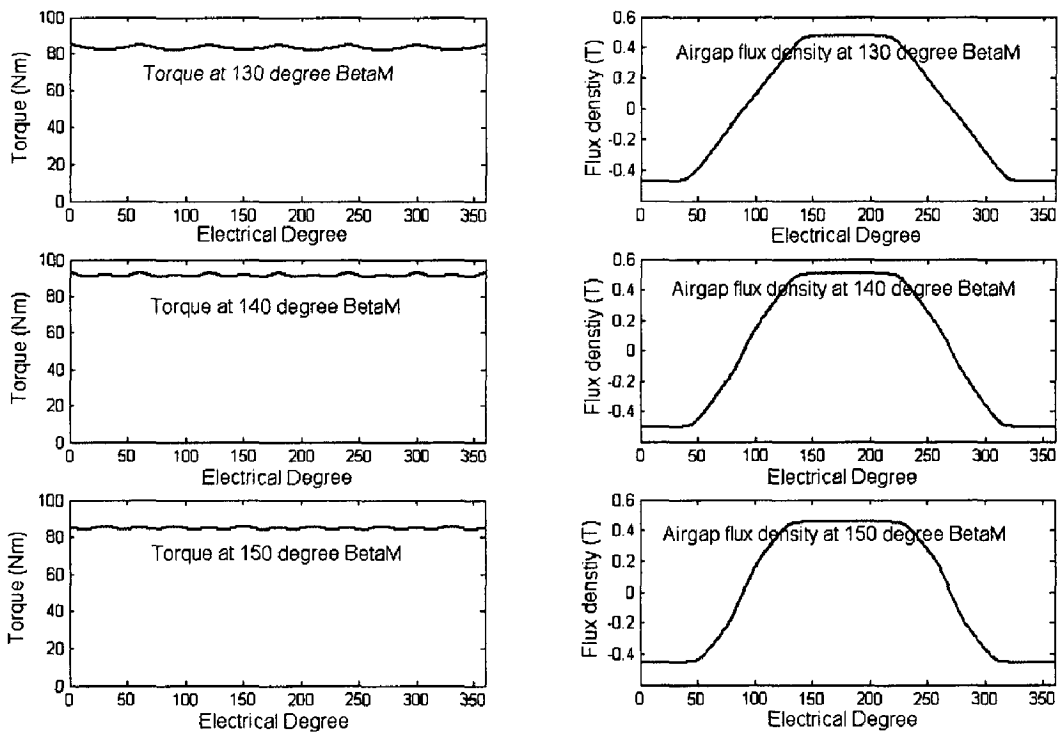
(d) BetaM variation

Fig. 2.10 Torque and flux density variation with parameter variation
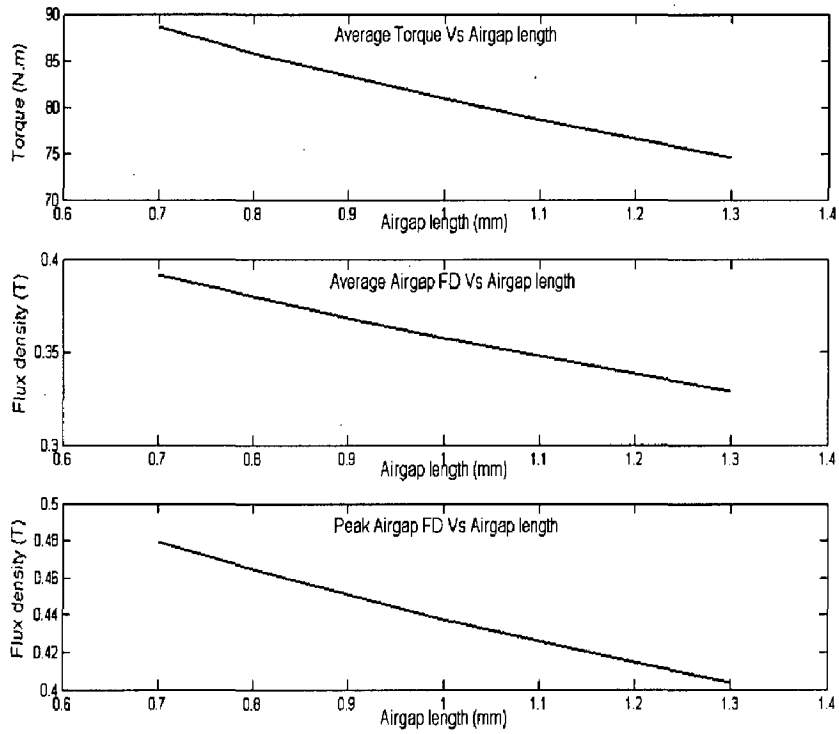
(a)
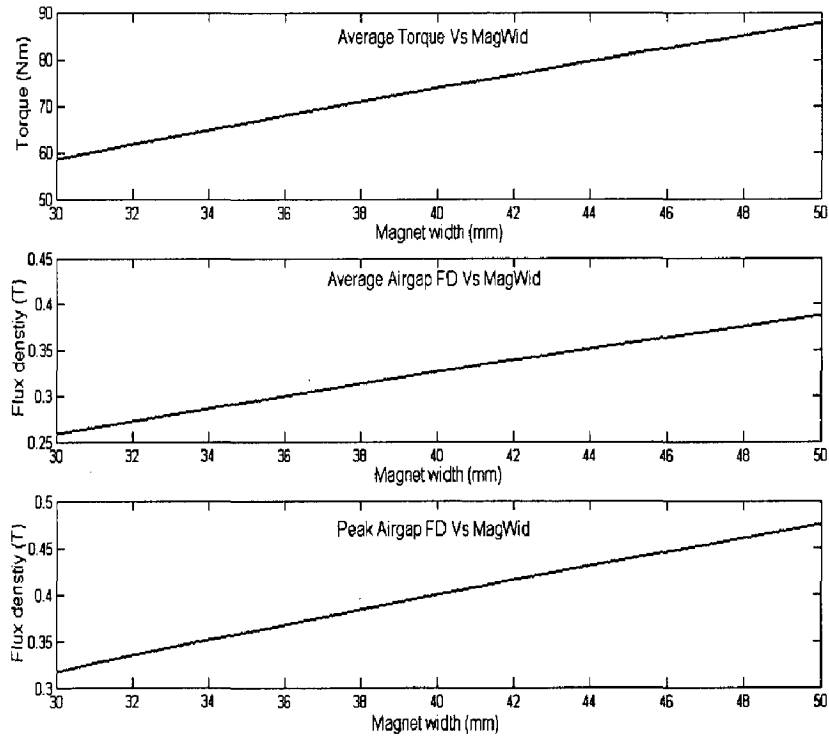
(b)
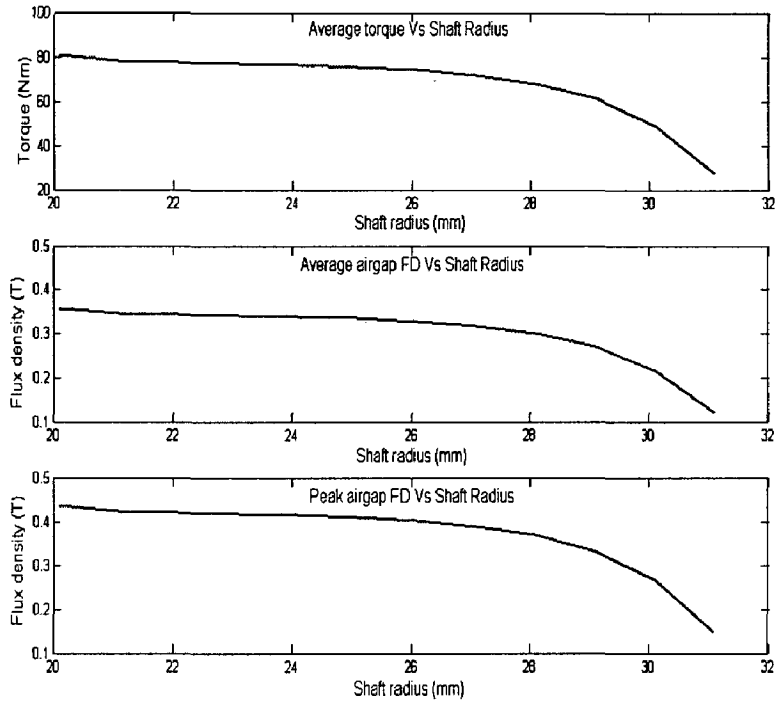
(c)
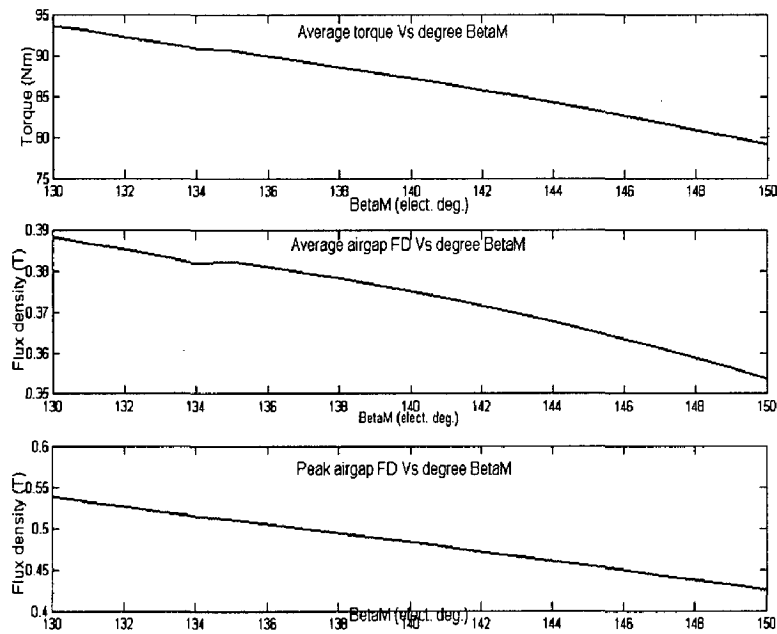
(d)

Fig. 2.11 Average torque, average flux density, and peak flux density variation with (a) Airgap (b) Magnet width (c) Shaft radius and (d) BetaM
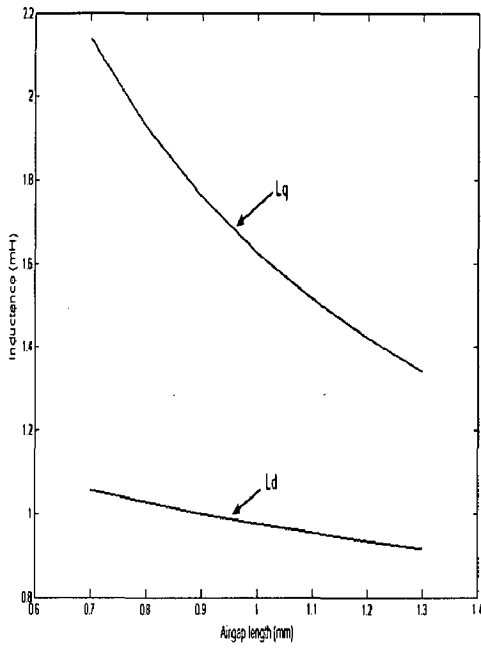
(a)
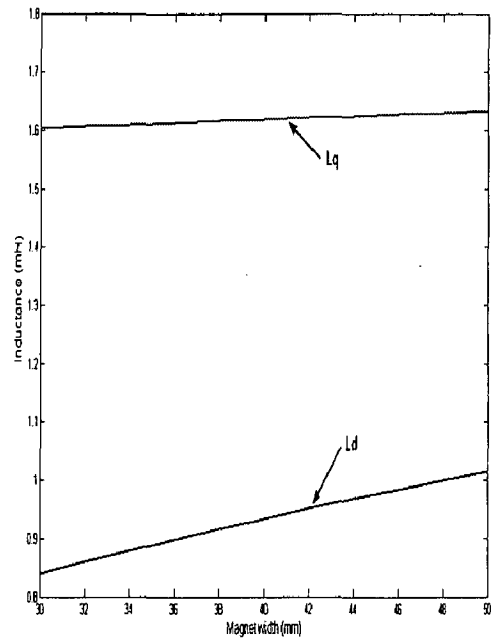
(b)
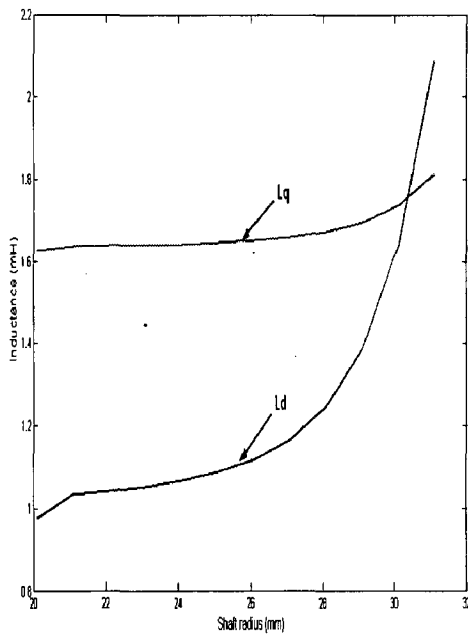
(c)
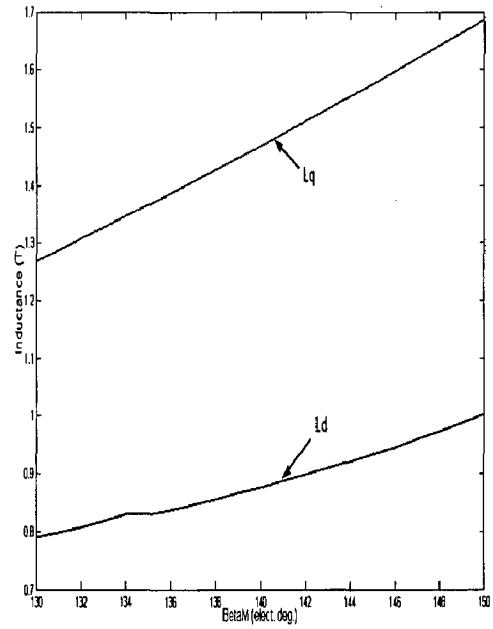
(d)

Fig. 2.12 L_q and L_d variation with (a) Airgap (b) Magnet width (c) Shaft radius and (d) BetaM

30

The influence of the parameter variation on the torque, flux density and q-, d-axis inductance are illustrated in Fig. 2.10 - 2.12. With the airgap length increasing, the torque developed is reduces and flux density in the airgap is also reduces. Here in analytical design saturation effect is neglected, where q- and d-axis inductance reduces as airgap length increases. Influence of magnet width is clear from the torque curve, where torque is more for more magnet width which in turn more magnet area increases cost and saturation in rotor core. The shaft radius has to be decided more precisely. It can be observed that as shaft radius increases, the torque and flux density reduces because shaft material considered as iron which permit path to flux lines through shaft. This allows less flux lines to pass through the airgap which can be said as leakage flux also. Shaft radius has to design with minimum flux lines pass through shaft; this can be decided with Fig. 2.11 (c). BetaM variation effect decides the magnet pole area and shape of flux density in the airgap. Airgap flux density wave should have minimum harmonic content which is observed in harmonic analysis of flux density wave. BetaM variation does not affect more on torque, which can also observe from the above figures.

In order to get finer results, the designed motor model in SPEED software transferred to FEM software tool. The analytical results and FEM results are compared experimentally with the existing motor in chapter 4.

Chapter 3

Finite Element Analysis of PMSM

3.1 Introduction

The finite element method (FEM) is a numerical method for solving electromagnetic field problems, which are too complex to be solved using analytical techniques, especially those involving non-linear material characteristics and complex geometrical design. The method basically involves the discretization of the motor cross-section (or volume in the case of 3-D analysis) into smaller area/volumes called finite elements. The spatial variation of a magnetic potential (vector or scalar) throughout the motor is described by non-linear partial differential equation derived from Maxwell's equations.

The advancement in computer technology enables us to solve even larger system of equations, to formulate and assemble the discrete approximation, and to display the results quickly and conveniently. This has also helped the finite element method become a powerful tool.

3.2 Basic Equations and Mathematical Model

3.2.1 Maxwell's Equations

Maxwell's equations are a set of fundamental equations governing all macroscopic electromagnetic phenomena. The equations can be written in both differential and integral form, but here taken them in differential form since they lead to differential equations to be dealt with by the finite element method.

For general time-varying fields, Maxwell's equations in differential form can be written as

$$\nabla \times E = -\frac{\partial B}{\partial t} \qquad \text{(Faraday's law)} \qquad (3.1)$$

$$\nabla \times H = J + \frac{\partial D}{\partial t} \qquad \text{(Maxwell's-Ampere law)} \qquad (3.2)$$

$$\nabla \cdot D = \rho \qquad \text{(Gauss's law)} \qquad (3.3)$$

$$\nabla \cdot B = 0 \qquad \text{(Gauss's law-magnetic)} \qquad (3.4)$$

where the basic variable

E	Electric field strength (volt/meter)
H	Magnetic field strength (ampere/meter)
D	Electric flux density (coulomb/meter^2)
B	Magnetic flux density (weber/meter^2)
J	Electric current density (ampere/meter^2)
ρ	Electric charge density (coulomb/meter^3)
t	Time

When the field quantities do not vary with time, we have a static magnetic field. In this case,

$$\nabla \times E = 0 \qquad\qquad (3.5)$$

$$\nabla \times H = J \qquad\qquad (3.6)$$

$$\nabla \cdot B = 0 \qquad\qquad (3.7)$$

Maxwell's equations become definite when constitutive relations between the field quantities are specified. The constitutive relations describe the macroscopic properties of the medium being considered. For a simple medium, they are

$$D = \varepsilon E \qquad\qquad (3.8)$$

$$B = \mu H \qquad\qquad (3.9)$$

$$J = \sigma E \qquad\qquad (3.10)$$

where the constitutive parameters ε, μ, and σ denote, respectively, the permittivity (farads/meter), permeability (henrys/meter), and conductivity (siemens/meter) of the medium.

In the finite element formulation of electromagnetic field problems, magnetic vector potential A can play an important role. It is commonly used in the solution of two-dimensional magnetic field, because in that case it reduces to a single component variable. To satisfy the non-divergence of the magnetic field, the vector potential is defined so that its curl is equal to the magnetic field density

$$B = \nabla \times A \qquad\qquad (3.11)$$

Accordingly $\nabla \cdot (\nabla \times A) = 0$ is satisfied for any A. However, to define the vector potential uniquely, Equation (3.11) alone is not enough. In magnetostatic field problems the Coulomb gauge is usually used to specify the magnetic vector potential

$$\nabla \cdot A = 0 \qquad\qquad (3.12)$$

The discussions above are pertinent for weak coupling.

3.2.2 Mathematical Model

Here in electromagnetic analysis of PMSM, only the steady-state solution may be of interest, which will disappear many cycles of starting and transients. For starting and transients analysis time-stepping of FEM solver can be used. Finite Element Analysis (FEA) is used to predict the torque produced at various currents, current phase angle and rotor positions as well as to calculate the phase inductances. The following assumptions are made in determining the magnetic field distribution inside the motor for 2-D (x, y plane) model:

a)   The outer periphery of the stator stamping can be treated as a zero magnetic vector potential line as the magnetic field outside the stator stamping is negligible.

b)   Magnetic materials of the stator and rotor stampings are isotropic and the magnetization curve is single valued (hysteresis effects are neglected).

c)   Magnetic vector potential A and current density J have only z-directed components.

d)   The magnetic field distribution inside the motor is constant along the axial direction of the motor.

e)   End effects are neglected.

For the steady-state time harmonic case, the field equation in terms of magnetic vector potential is given by

$$\frac{1}{\mu}\frac{\partial^2 A}{\partial x^2} + \frac{1}{\mu}\frac{\partial^2 A}{\partial y^2} = -J + j\omega\sigma A \qquad\qquad (3.13)$$

The first term on the right-hand side is the applied source current density and the last term is induced eddy-current density. By solving the diffusion equation (3.13) using traditional FEM procedure, one can get the magnetic vector potential A for all the nodes in the solution region.

The governing equation of the electromagnetic field is given by

34

$$\nabla \times (\nu \nabla \times A) = J \qquad (3.14)$$

where ν is the reluctivity of the material.

In the area of stator conductor, the magnetic field equation can be represented as

$$\nabla \times (\nu \nabla \times A) + \frac{i_s}{S} = 0 \qquad (3.15)$$

In the iron cores and air-gap area, the magnetic field can be expressed as

$$\nabla \times (\nu \nabla \times A) + \sigma \frac{\partial A}{\partial t} = 0 \qquad (3.16)$$

In the air gap and laminated stator iron core (which is the case considered in current design) $\sigma \dfrac{\partial A}{\partial t}$ is zero. It can only exist in the solid rotor iron core where eddy currents cannot be ignored.

In the rotor PM area, the field equation can be expressed as

$$\nabla \times (\nu \nabla \times A) = \nabla \times (\nu B_r) \qquad (3.17)$$

For circuit-field-torque coupled time-stepping FEM, one should use the circuit equations and which can be coupled with mechanical motion equation.

3.2.3 Finite Element Formulation

The two most popular methods of deriving the finite element equations are the variational approach and Galerkin approach, which is a special case of the method of weighed residuals (MWR). In this study, Galerkin's method is used for the finite element formulation. According to the Galerkin's method, magnetic vector potential can be expressed as

$$A = \sum_{i=1}^{m} N_i(x, y) A_i \qquad (3.18)$$

where m is number of nodes in the element which is 3 for triangular element in current case, N_i are the element shape function which may be linear, quadratic, or higher order function, and the A_i are the approximations to the vector potentials at the nodes of the elements.

Now applying Galerkin's formulations for each of the model derived above, for stator conductor field equation is

35

$$\iint \left[\frac{\partial N_i}{\partial x} \frac{\partial}{\partial x} v \sum_{j=1}^{3} N_j A_j + \frac{\partial N_i}{\partial y} \frac{\partial}{\partial y} v \sum_{j=1}^{3} N_j A_j + N_i \frac{i_s}{S} \right] dxdy = 0 \qquad (3.19)$$

Writing above equation in matrix form,

$$\left[v[G]\{A\} + \{Q\}\frac{i_s}{S} \right] = 0 \qquad (3.20)$$

For laminated stator iron and air gap,

$$\iint \left[\frac{\partial N_i}{\partial x} \frac{\partial}{\partial x} v \sum_{j=1}^{3} N_j A_j + \frac{\partial N_i}{\partial y} \frac{\partial}{\partial y} v \sum_{j=1}^{3} N_j A_j \right] dxdy = 0 \qquad (3.21)$$

In matrix form,

$$\left[v[G]\{A\} \right] = 0 \qquad (3.22)$$

For the rotor iron core,

$$\iint \left[\frac{\partial N_i}{\partial x} \frac{\partial}{\partial x} v \sum_{j=1}^{3} N_j A_j + \frac{\partial N_i}{\partial y} \frac{\partial}{\partial y} v \sum_{j=1}^{3} N_j A_j \right] dxdy + \iint \left[\sigma N_i \left(\frac{\partial A_i}{\partial t} \right) \right] dxdy = 0$$

$$(3.23)$$

In matrix form,

$$\left[v[G]\{A\} + \sigma[T]\left\{ \frac{\partial A}{\partial t} \right\} \right] = 0 \qquad (3.24)$$

For the permanent magnet,

$$\iint_\Omega v \left(\frac{\partial A}{\partial x} \frac{\partial N_i}{\partial x} + \frac{\partial A}{\partial y} \frac{\partial N_i}{\partial y} \right) dxdy = \iint_\Omega \left(v\mu_0 \left(M_x \frac{\partial N_i}{\partial x} - M_y \frac{\partial N_i}{\partial y} \right) \right) dxdy$$

$$(3.25)$$

In matrix form,

$$v[G]\{A\} = \frac{v}{2}\left(B_{rx}[c_i] - B_{rx}[b_i] \right) \qquad (3.26)$$

By solving above equations with the given motor geometry, material properties, input currents and magnetization of PM, the vector potential values A in the nodes of FE meshes can be found. During assembly process, cubic splines used to approximate B-H curve of the nonlinear material. Maxwell stress tensors are used to calculate the torque. After getting the global system of equation, Newton-Raphson iteration method is used to find the roots. During each iteration, a preconditioned iterative method, such as biconjugate gradient can be used to solve the nonsymmetrical linear matrix.

3.3   FEM Simulation steps

There are number of steps in the solution procedure using finite element methods. All finite element packages require the user to go through these steps in one form or another.

1) Specifying Geometry - First the geometry of the structure to be analyzed is defined. This can be done either by entering the geometric information in the finite element package through the keyboard or mouse.

2) Specify Element Type and Material Properties - Next, the material properties are defined. This involves defining the types of elements corresponding to each material type and size of element depends on region importance, size of area etc.

3) Mesh the Object - Then, the structure is broken (or meshed) into small elements. Specifying how the structure will be subdivided into elements (how it will be meshed) into the different areas. It is useful to have high element densities, with small elements, in critical regions of the solution domain.

4) Apply Boundary Conditions and External Loads - Next, the boundary conditions (e.g. Vector Potentials) and the external loads (e.g. Current densities) are specified.

5) Generate a Solution - Then the solution is generated based on the previously input parameters.

6) Post processing - Based on the initial conditions and applied loads, data is returned after a solution is processed. This data can be viewed in a variety of graphs and displays.

7) Refine the Mesh - Finite element methods are approximate methods and, in general, the accuracy of the approximation increases with the number of elements used. The number of elements needed for an accurate model depends on the problem and the specific results to be extracted from it. Thus, in order to judge the accuracy of results from a single finite element run, you need to increase the number of elements in the object and see if or how the results change.

8) Interpreting Results - This step is perhaps the most critical step in the entire analysis because it requires that the modeller use his or her fundamental knowledge of electromagnetics to interpret and understand the output of the model. This is critical for applying correct results to solve real engineering problems and in identifying when modelling mistakes have been made (which can easily occur).

In general these eight steps can be grouped in three stages as:

(A) Pre-Processing, (B) Field Solution and (C) Post-Processing

3.4 Simulations Results

3.4.1 Geometry of Model and Mesh Generation

First stage for FE simulation is building a finite element model, in which more of the time requires than any other part of the analysis in modern FEM softwares. The motor geometry designed in analytical tool is modelled. Each region of 2-D geometry is defined as different components, for example, the stator lamination, rotor core, permanent magnet, airgap, shaft, etc. Modern mesh generation is carried out using the internal specialist drafting facilities of the finite element software itself. Fig. 3.1 shows the model 2-D geometry with 8 poles, 48 slots.
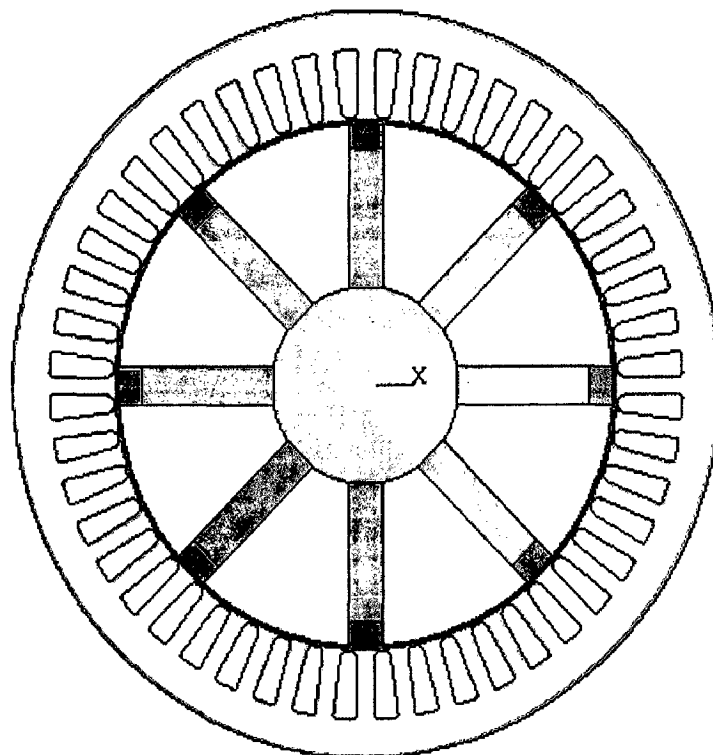
Fig. 3.1 Motor 2-D Geometry

The different colours in the above figure represent the different material assignment for different areas. It can be seen that winding is single layer full pitch winding and winding slot area is current cross section area. The rotor iron core material is same as stator steel core; airgap and shaft material is nonmagnetic material. Magnet is magnetizing perpendicular to the magnet length at any given position of rotor. Modern mesh generation is carried out using the internal special drafting facilities of the finite element software itself. Fig. 3.2 shows the finite element subdivisions. The close segment edges and airgap gives detailed data.
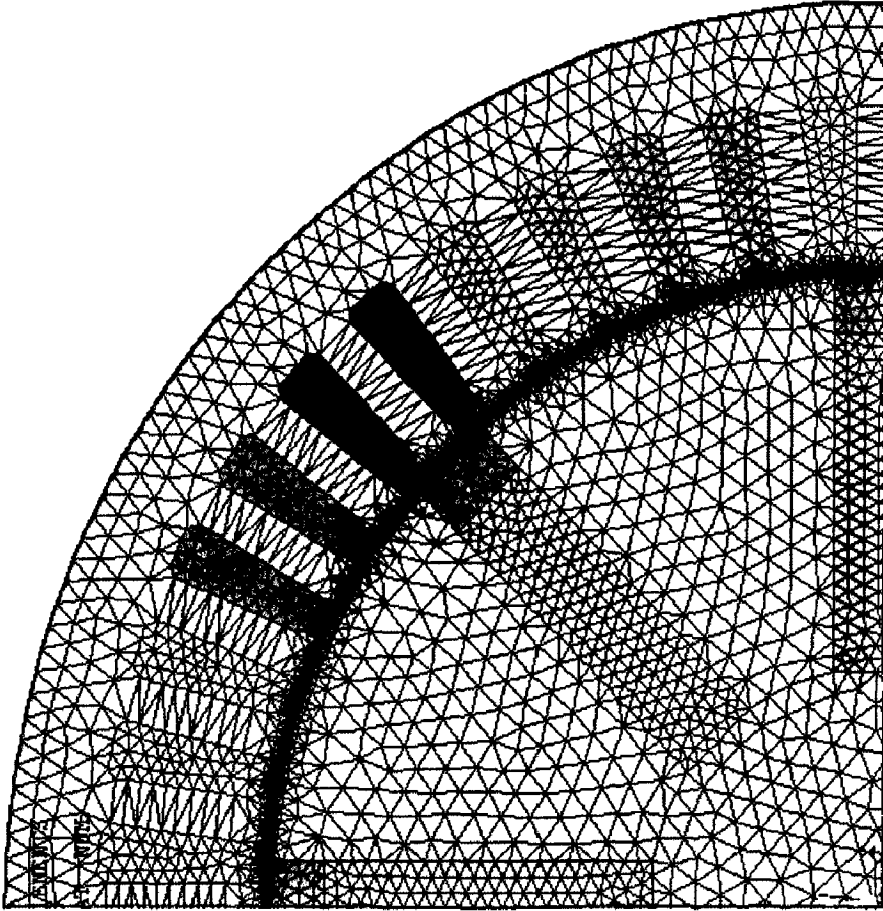
(a) Mesh model of 1/4th geometry
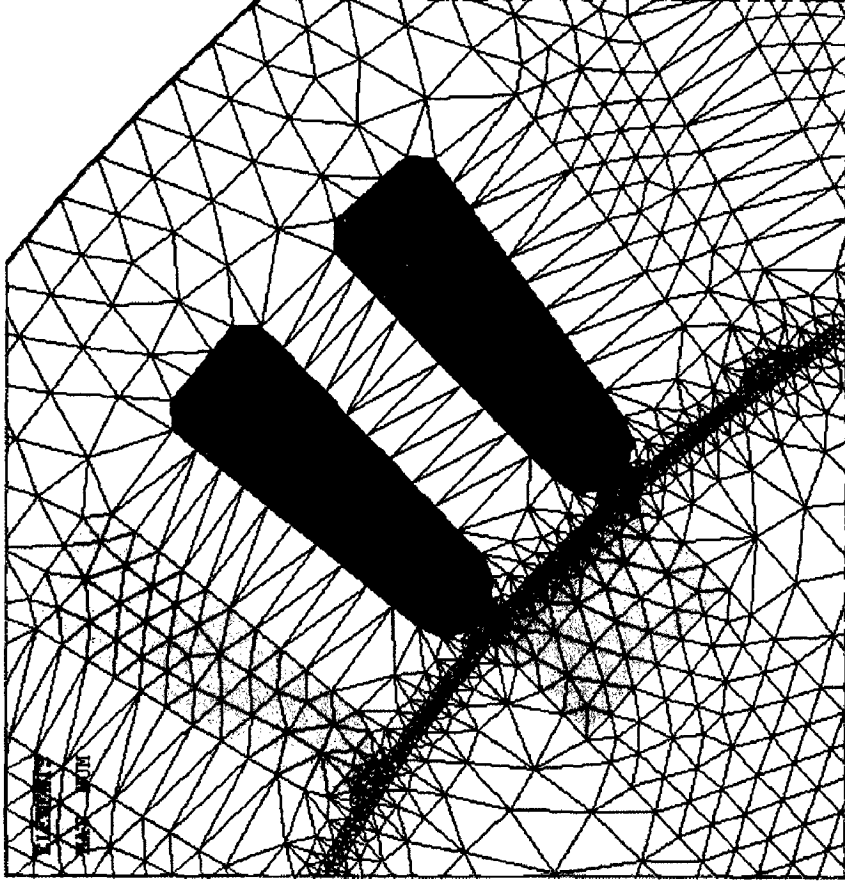
(b) Mesh showing details of airgap, slot and magnet elements

Fig. 3.2 FEM mesh

39

In the second stage of field solution the partial differential equation uses specialized mathematical algorithm. The discretization transforms the partial differential equation into a large number of simultaneous nonlinear algebraic equations containing the unknown node potentials. With linear elements, the potential is assumed to vary linearly between nodes and the flux density is constant within each element associated with a winding. Iteration is used for nonlinear magnetic characteristics, Newton-Raphson method is used to find the solution with provided inbuilt facility in FEM software tool.

3.4.2 Post-Processing

Post-processing is the third stage which is use to review analysis results over the entire model, or selected portions of the model, for a specifically defined combination of loads at a single time. The field solution is in terms of magnetic vector or scalar potential, but the main area of interest is in flux densities, torque, and inductance. The extraction of these quantities from the potential solution is called post-processing.

3.4.2.1   No Load Condition

Flux distribution, flux density contour, and field intensity contour

Fig. 3.3 shows the flux distribution created by the rotor magnets alone. The contour plots of B and H are as shown in Fig. 3.4. With these plots magnetization of Magnet, flux concentration in teeth and airgap, variation of flux density in rotor and stator core can be observed.
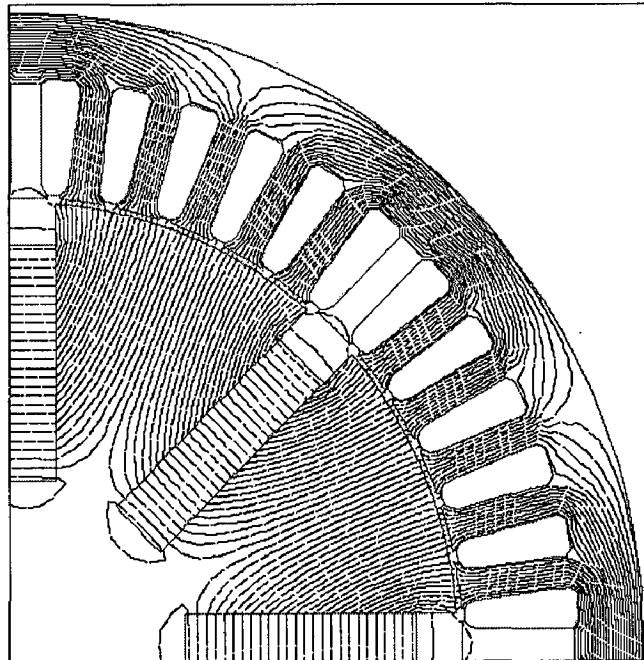
Fig. 3.3 Flux distribution due to magnets acting alone (open-circuit condition)

NODAL SOLUTION
HSUM   (AVG)

☐ .243674
☐ 44957
☐ 89913
☐ 134870
☐ 179826
☐ 224783
☐ 269740
☐ 314696
☐ 359653
☐ 404609

Fig. 3.4 (b) Field intensity distribution

NODAL SOLUTION
BSUM   (AVG)

☐ .158E-04
☐ .117992
☐ .235967
☐ .353943
☐ .471919
☐ .589895
☐ .707871
☐ .825846
☐ .943822
☐ 1.062

Fig. 3.4 (a) Flux density distribution

41

Flux density vectors

In this form of display, arrows of a size related to element stresses and indicating the direction of the stress appear on a plot of the geometry. This form of plot is helpful to understanding effect of fields and direction of magnetic field strength. Fig. 3.5 shows the flux density vectors on no load condition.

VECTOR
B

.370E-05
.13599
.271977
.407964
.543951
.679937
.815924
.951911
1.088
1.224
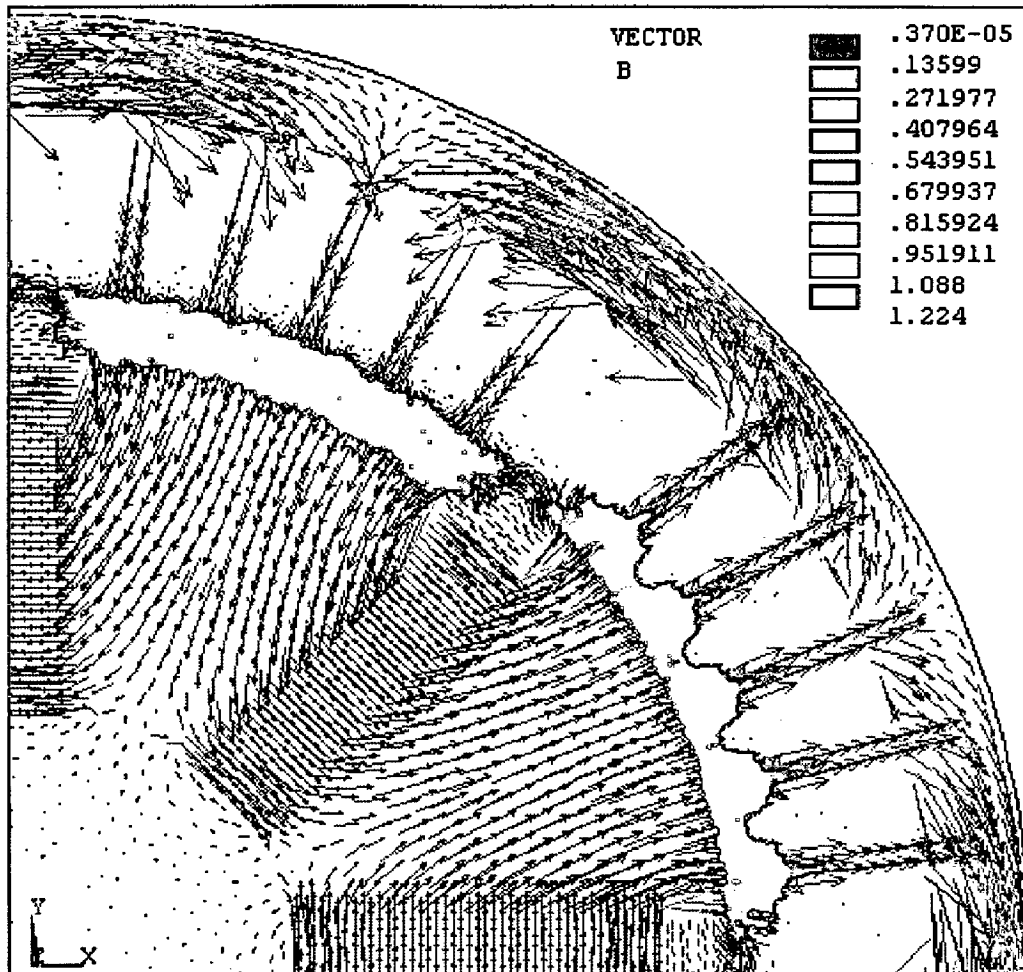
Fig. 3.5 Flux density vectors (no load)

Airgap flux density

From Fig. 3.3, we can obtain airgap flux density where we can see the exact flux density variation in the airgap effect of slotting which is as shown in Fig. 3.6 (a) under one pole area. Using this data of airgap path, integrating the flux density w.r.t. distance we can obtain average flux density through airgap. The integration of airgap flux density is as shown in Fig. 3.6 (b).

42
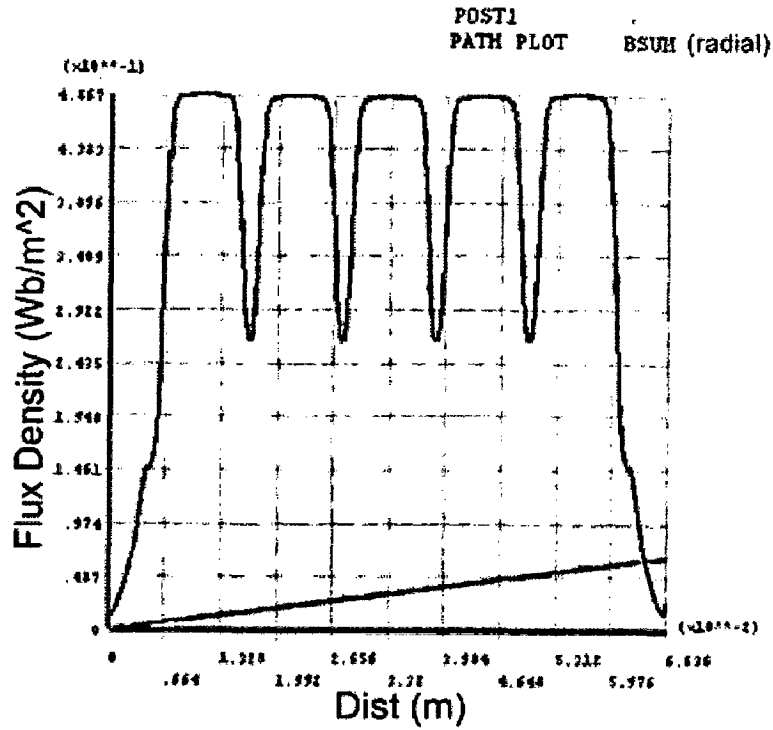
(a) Airgap flux density (no load)
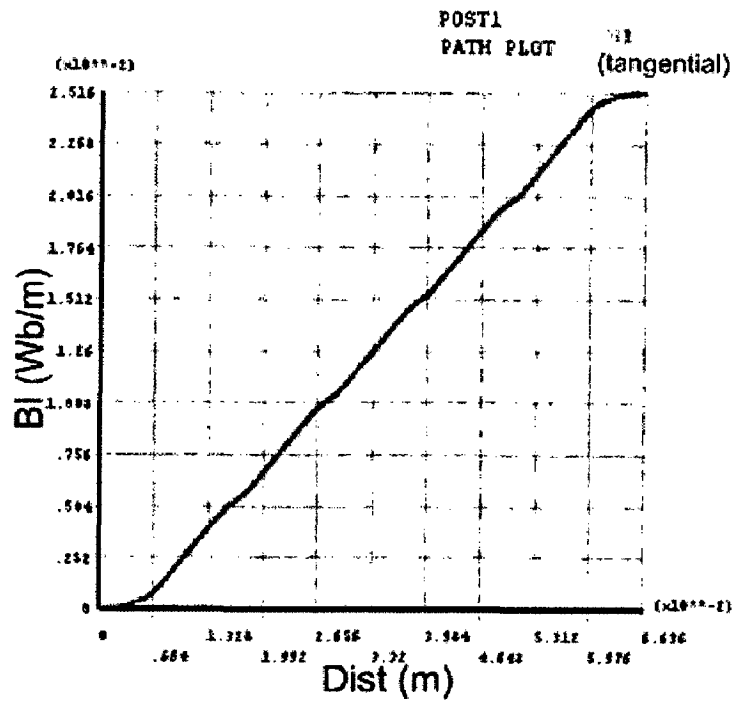
(b) Integration flux density path over distance under one pole

Fig. 3.6 Airgap flux density variation and integration

Average Flux density under one pole is $\dfrac{2.516^{-2}\ (Wb/m)}{6.636^{-2}\ (m)} = 0.379\ Wb/m^2$ on no

load condition.

3.4.2.2 Armature Reaction

The effect of armature reaction can be observed, while applying current load in armature conductors. The armature conductors are considered as 4 conductors per slot. By applying current with each conductor and dividing by slot area, current density load in one slot area can be determined. The current distribution is considered as sinusoidal and can be varied based on q or d-axis current. In the following figures, the current vector is considered as peak in q-axis, i.e. q-axis current of 80A amplitude. 80A current is chosen for the study to observe the effect of machine for 80% loading, which is considered as average loading.
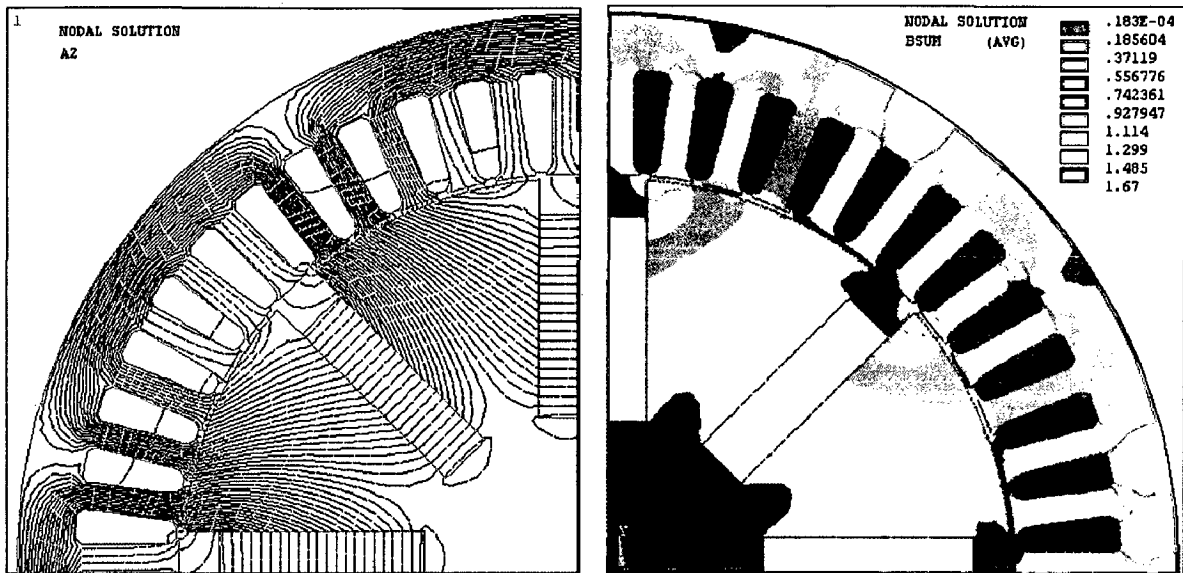
(a) Flux lines   (b) Flux density contour
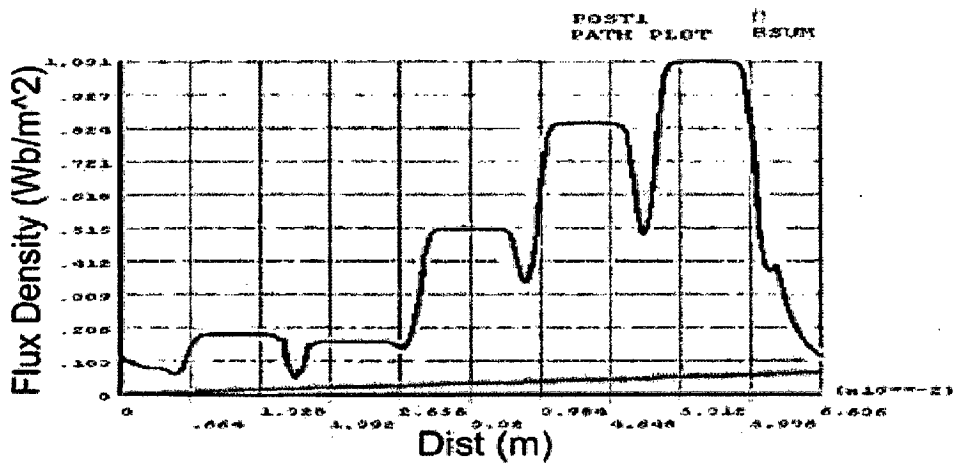
(c) Variation of flux density under one pole

Fig. 3.7 Armature reaction due to q-axis current

3.4.2.3   Calculation of Torque and Inductance

It is natural to calculate the torque and inductance of the machine using finite element results, since these quantities are most important to observe the characteristic of machine. The designed PMSM motor is a motor, in which synchronous and reluctance torque produces simultaneously corresponding to stator current phase angle w.r.t. q-axis. The magnitude of reluctance torque is also depending on the ratio of q- to d- axis inductance, i.e. L_q/L_d . Based on designed machine geometry, q- and d-axis inductances are calculated. The torque is calculated using a Maxwell Stress Tensor approach [06] in ANSYS. In Fig. 3.8, the calculated torque is shown with the current phasor rotating from 0 to 90 electrical degrees in the negative d-axis direction from q-axis. It is evident that the reluctance torque magnitude is higher at higher current amplitude. The maximum torque at each current is achieved at phase angles in between 0 and 40 electrical degrees; this can be used to find maximum torque line in current q-d plane.
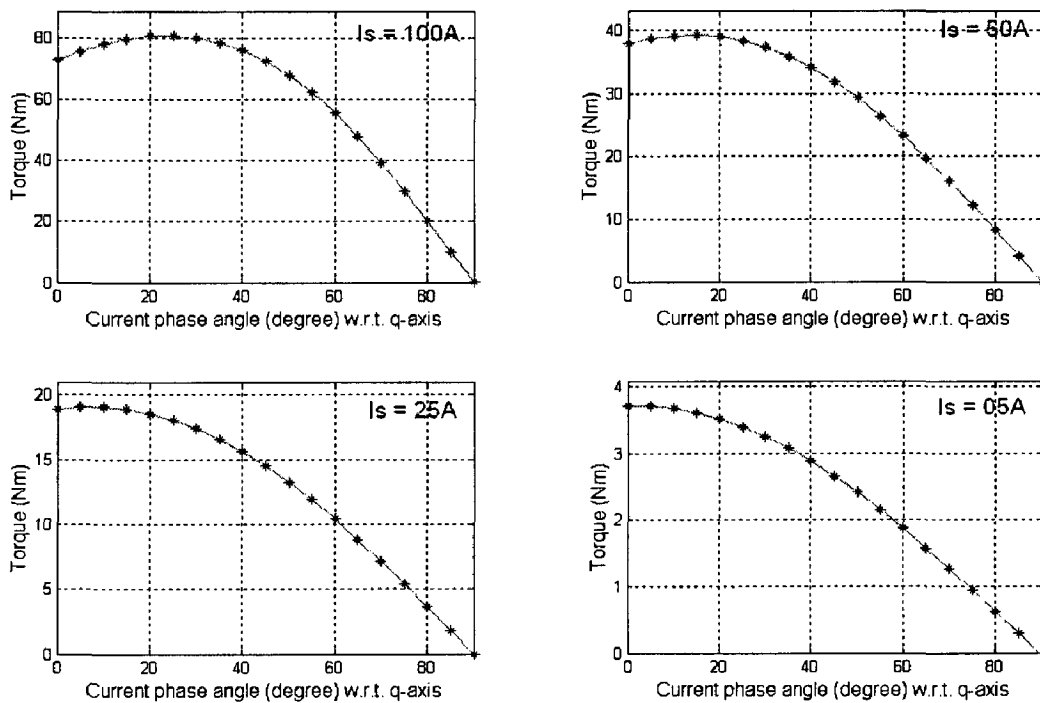
Fig. 3.8 Torque characteristics with current phase angle

45

For the calculation of the inductance, currents are distributed sinusoidally in the stator winding such that the field produced peaks at the direct axis for d-axis inductance and field peaks at the quadrature axis for q-axis inductance. The current, therefore, peaks at the quadrature axis for d-axis inductance and the PM are left unenergized. In this case, L_d is the inductance of the winding. The machine has to be modelled for the single winding and winding has to be energized based on the inductance to be calculated. Following figures shows flux distribution for the calculation of q- and d-axis inductance.

(a) q-axis flux   (b) d-axis flux
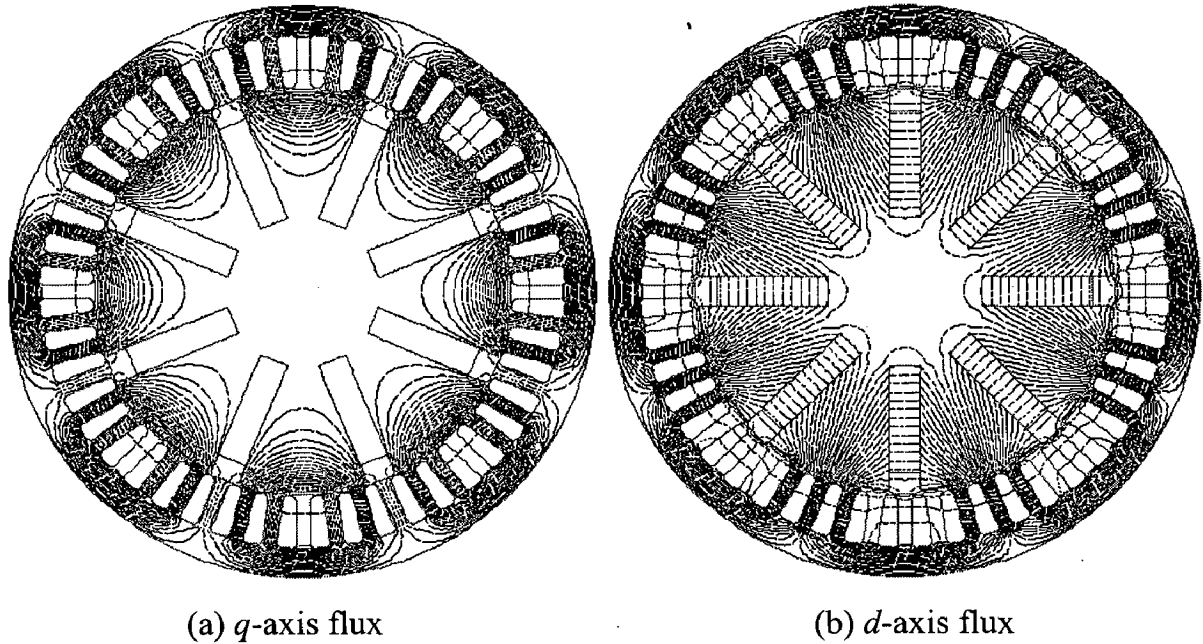
Fig. 3.9 Magnetic flux distribution in the q- and d-axis

The calculated value of q- and d-axis inductance for different value of current is summarized in the Table 3.1.

Table 3.1 q- and d-axis inductance

S No	Ia (A)	q-axis (H)	d-axis (H)
01	0.10	1.7840 e-03	0.95724 e-03
02	01	1.8202 e-03	0.96481 e-03
03	10	1.8830 e-03	0.98061 e-03
04	25	1.8978 e-03	0.98744 e-03
05	50	1.8960 e-03	0.98972 e-03
06	75	1.8724 e-03	0.98991 e-03
07	100	1.5030 e-03	0.98888 e-03

46

Chapter 4

Co-simulation-based Design

Rotating electrical machinery presents a uniquely complicated system of non-linear, constrained, discrete and discontinuous relationships. The economical solution of the design of electrical machines can only be achieved by a marriage of various numerical and analytical adaptive techniques. Nowadays, various software packages are available, which are specialized in specific area. For example (1) SPEED and RMxprt are specifically designed for the Motor/Generator design using analytical relations, (2) FEMLAB, ANSYS and FLUX2D are used for numerical field analysis of electrical machine, and (3) Matlab and SIMPLORER are very good for simulation of machine, load and battery; and strategies that controls and regulate speed and torque. The machine design has different stage and different area of analysis, Basic block diagram of the machine design in which only analytical and numerical field solution is involved is shown in Fig. 4.1.
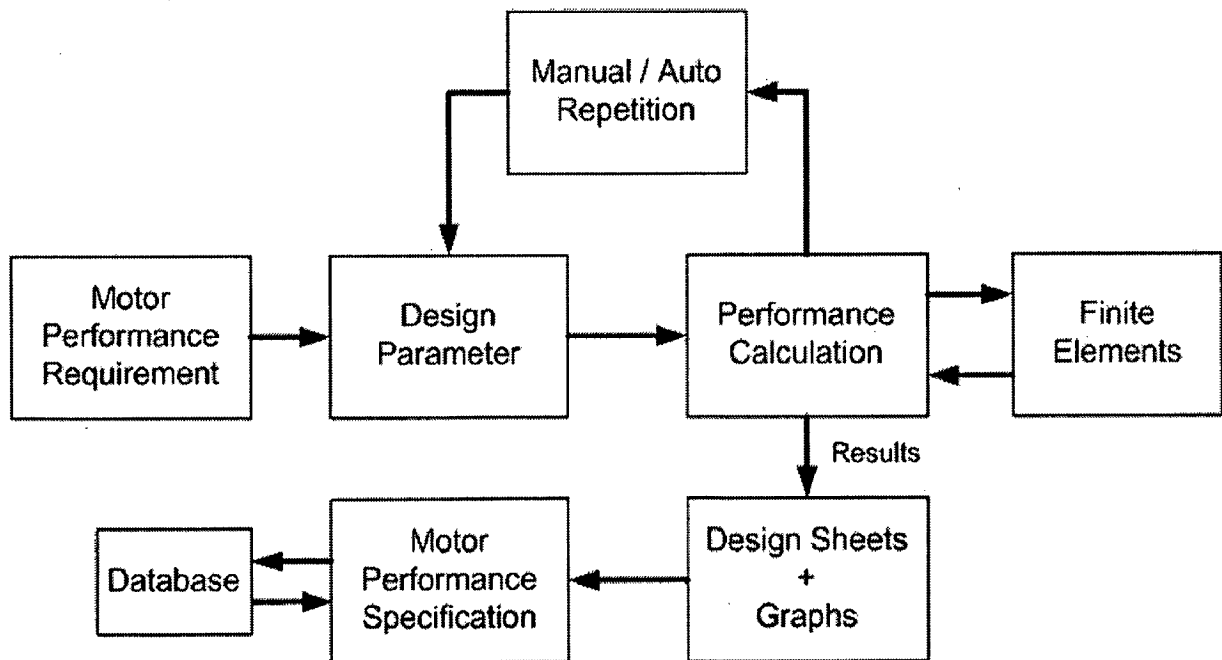
Fig. 4.1 Block diagram of basic design procedure

From the above diagram, it can be seen that more than one tool has to be used for the designing of machine. In current study of design of PMSM motor, SPEED and

ANSYS software package is used for analytical and numerical field calculation. In previous two chapters both analysis has done individually.

4.1 Application Management

Typically in multi disciplinary analysis deals with different software tools and correspondingly different models for each discipline. Therefore, an important aspect for the realization of multidisciplinary design is the integration of discipline specific software codes into a common analysis and optimization environment. This integration is done using a application management concept. The application manager is responsible for the data management, job administration and execution. Such an application management conceptual block diagram is shown in Fig. 4.2.

Matlab provides a flexible environment for the integration of other software tools. Furthermore, it provides a broad spectrum of functions and algorithms for wide range of purposes (e.g. control system analysis, data storage, visualization) and also offers a highly flexible environment for implementing self developed algorithms. Hence, here Matlab is chosen as the application manager. The task carried out in this section is the integration of the FEM-program ANSYS and the CAD tool SPEED using Matlab.
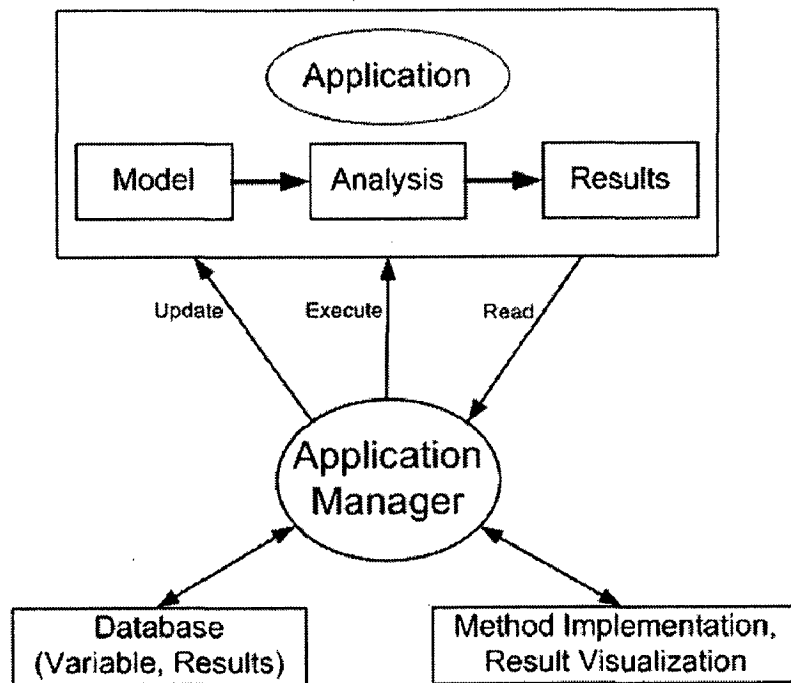

Fig. 4.2 Application Manager

4.2 Integrating SPEED and ANSYS into Matlab environment

Using ActiveX in Matlab for SPEED

As Matlab is a cross-platform application, available on SUN, HP, IBM and SGI workstations (amongst others) as well as on MS-Windows based PCs it can not be too closely tailored for one specific platform feature. Whereas VB and MS-Windows versions of other languages such as Delphi and C++ have been extended to directly support ActiveX, Matlab has taken a much more conservative approach. By using this ActiveX one can add/modify ActiveX controls that are registered on the system in the User Interface Editor and program them in their own programs. Additional language support for ActiveX can take one of two forms: additional or extended commands (the Set or New commands in VB for example) and syntax support (extending the "." operator to access object properties and methods). The latter is a particularly common enhancement. In Matlab basic ActiveX support can be performed by four new commands although there are several others that are not necessary for straightforward work. By using *actxserver* in Matlab with *invoke* command here SPEED's PC-BDC has been executed and same design can be executed by changing different parameters and at same time, required waveforms can be accessed in Matlab [34]. With help of the above commands the simulations can be repeated and results have been shown in section 2.4.9. The flow chart of the algorithm is shown in Fig. 4.3 (a).

Using ANSYS Batch Mode from Matlab

In batch mode, one can submit a file of commands to the ANSYS program. On some operating system, a batch job can be run in the background while doing other work on the computer [35]. Batch job can be started in Windows by issuing the ANSYS execution command directly from the MS-DOS command prompt. The same system level command has been executed through Matlab for a batch run. At the end of batch run an ASCII result file is created by ANSYS, which is then read in by Matlab. In section 3.4.2.3 torque has been calculated using this algorithm with repeated simulation at one time. The program flow chart of FEM analysis is shown in Fig. 4.3 (b).
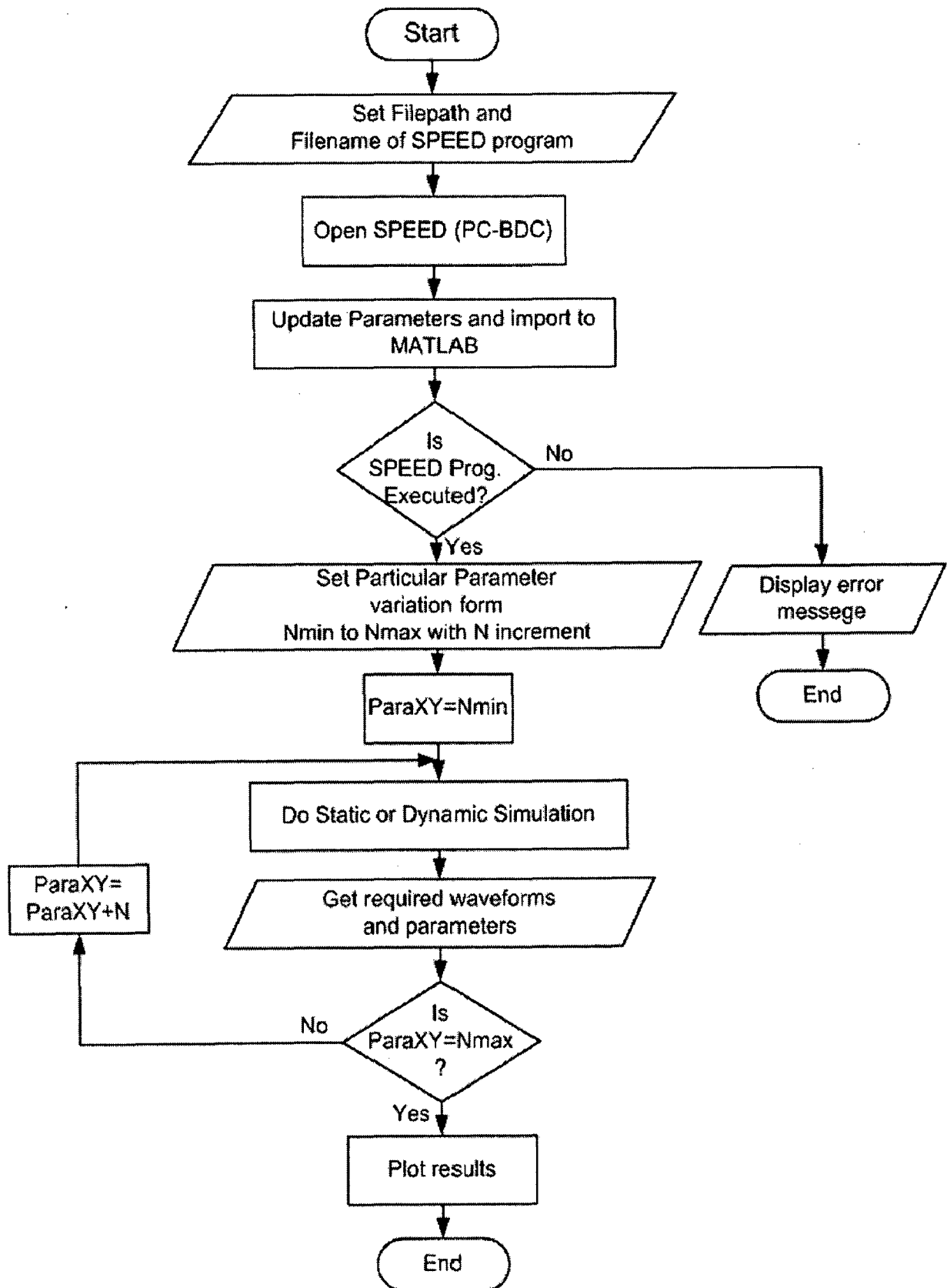
Fig. 4.3 (a) Flow chart of machine design repetition with parameter variation

50
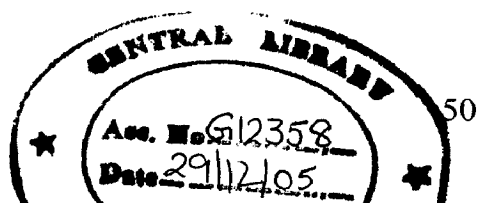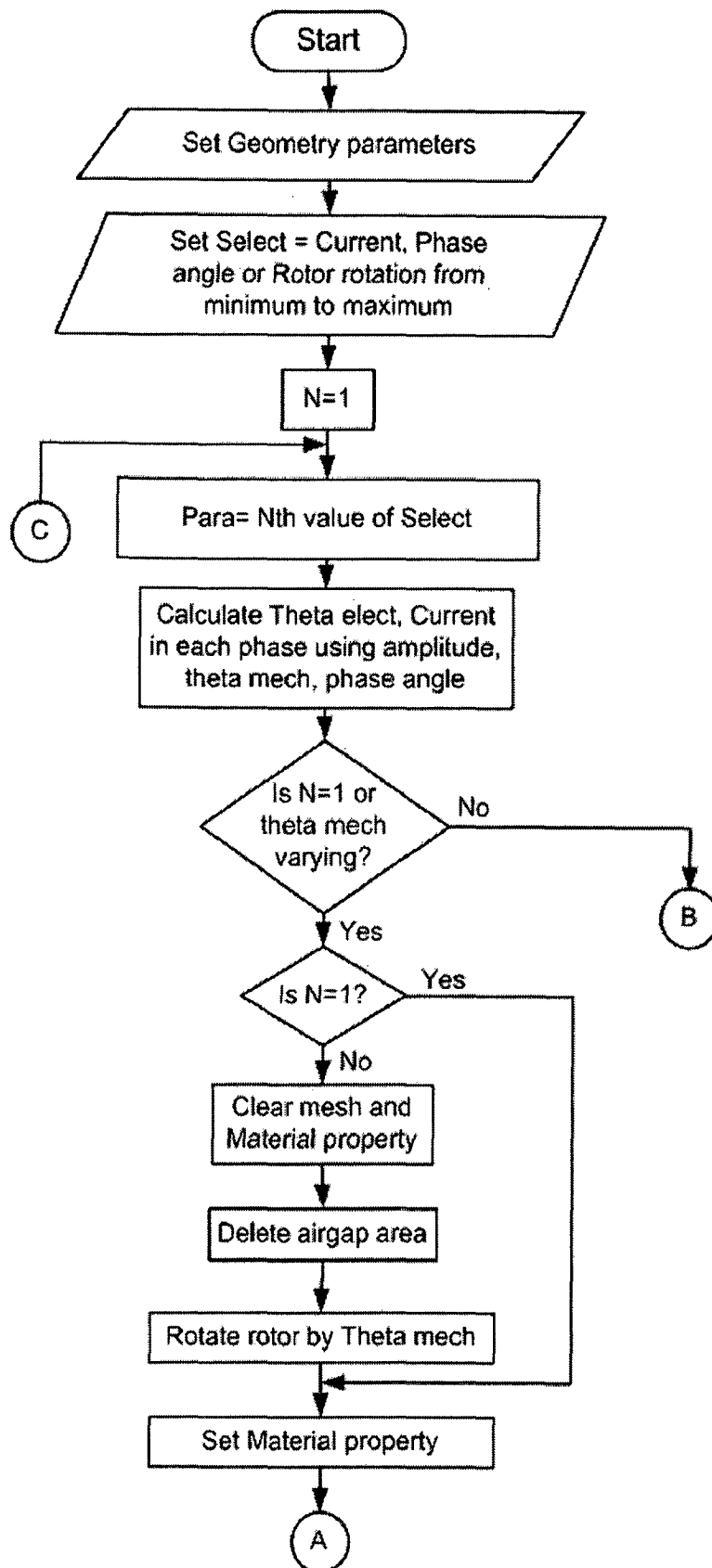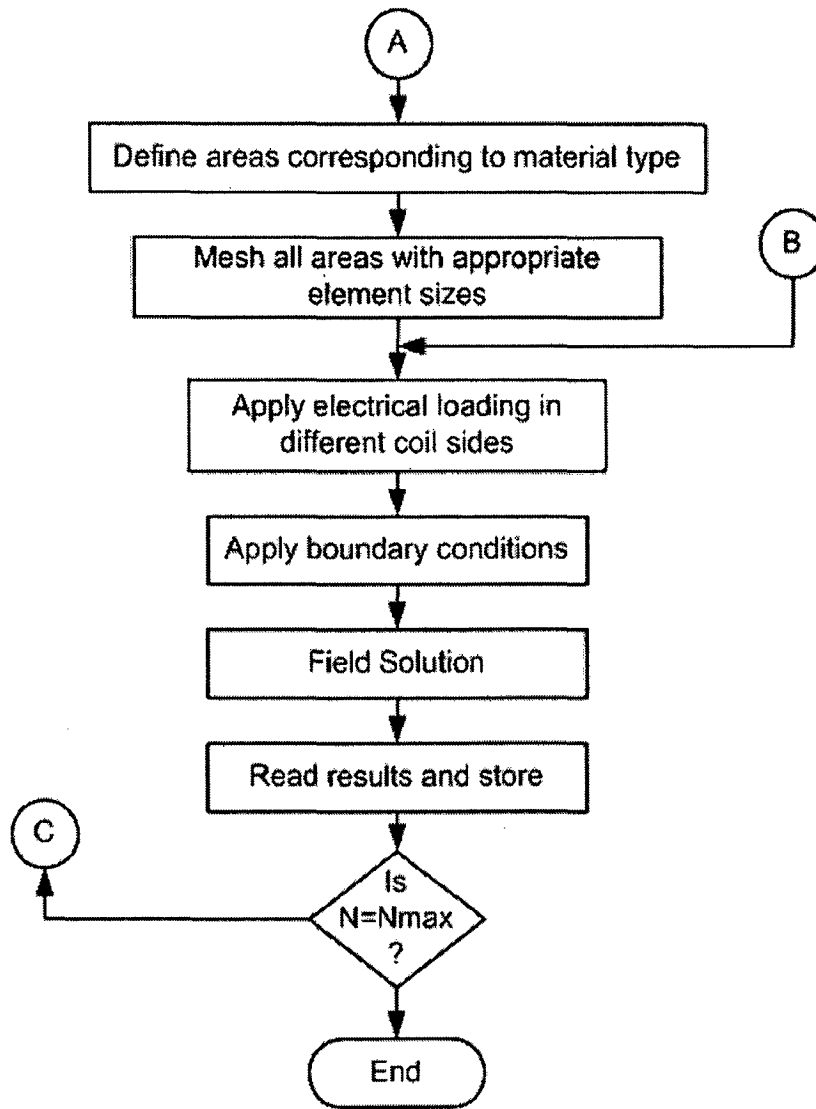
Fig. 4.3 (b)

Fig. 4.3 (b) FE program for repeated analysis flow chart

4.3 Integrated Design Flow

The machine is designed in analytical software tool, to get better result on torque and inductance value considering saturation, we have to simulate same machine in finite element software tool. For this it is necessary to transfer machine model to finite element calculation tool. Another aspect of integrated design flow is that it is also necessary to simulate machine with drive and control module, where also it is necessary to transfer model to this simulation tool for control and drive module. The design flow diagram is shown in Fig. 4.4.
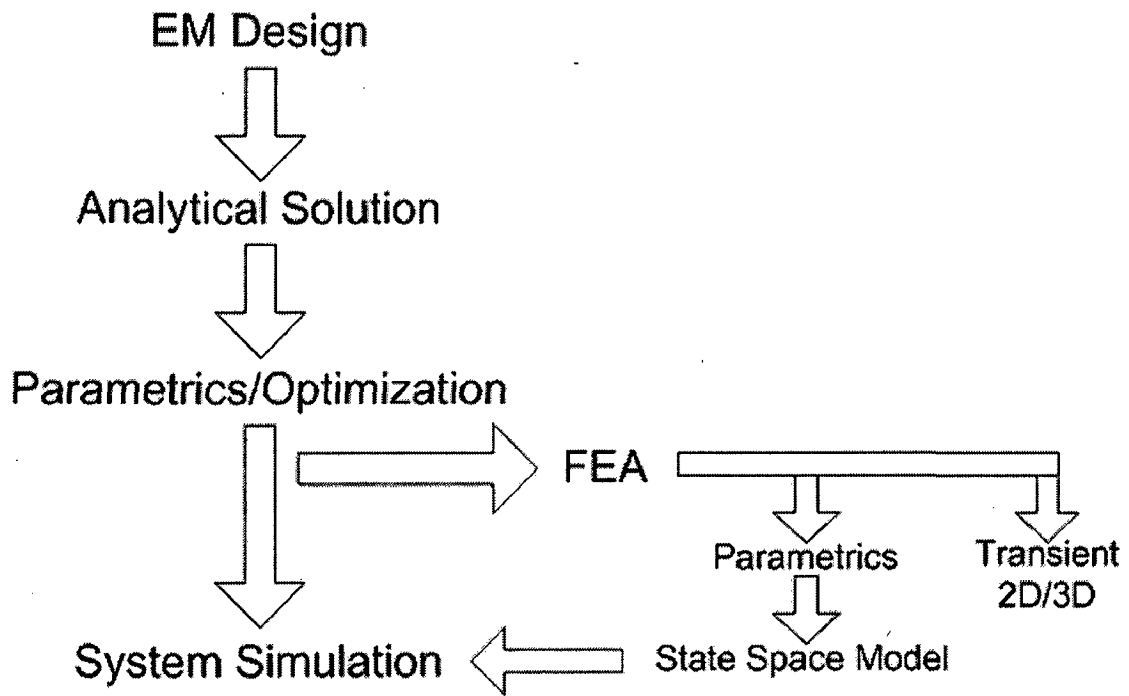
Fig. 4.4 Design Flow

4.4   Results Comparison

4.4.1 Analytical and FEM results comparison

Analytical calculation and finite element calculation results are compared for flux density, torque and inductance calculations. Fig. 4.5 shows the comparison of the airgap and yoke flux-density distribution, obtained by the finite-element tool and analytical calculation tool. The finite-element solution includes the effect of the slot-openings in airgap flux density and saturation effect in yoke flux density. These effects are absent in the analytical solution, which can be observed from the result.
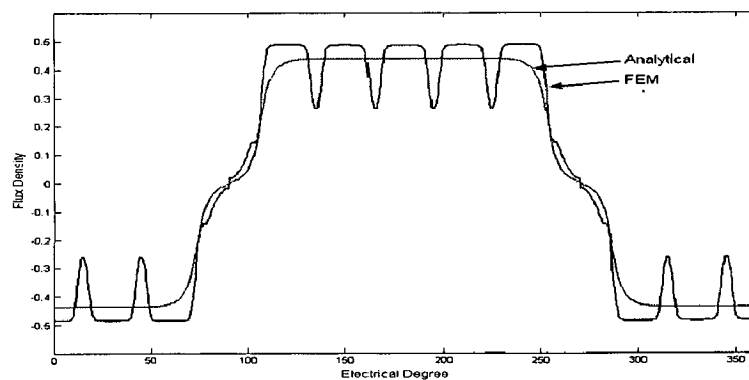
(a) Without skewing
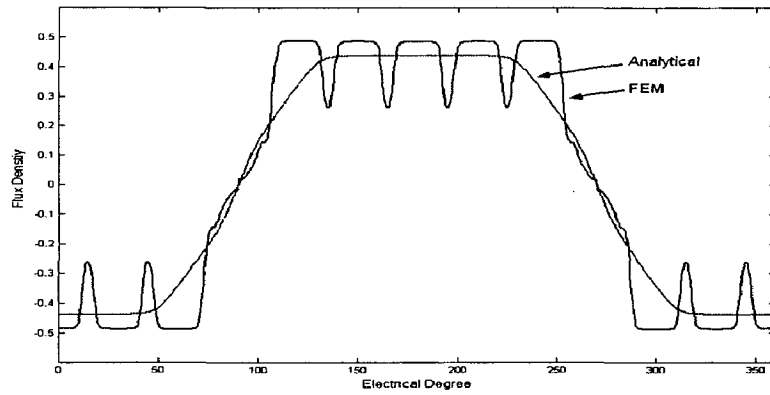
(b) Skewed slot in analytical tool
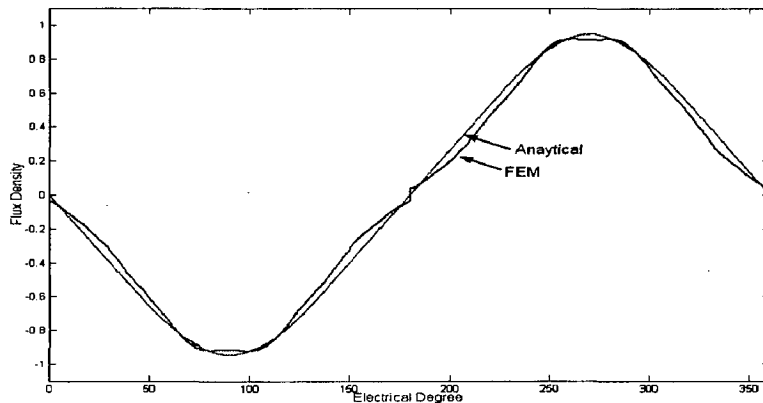
(c)Yoke flux density variation

Fig. 4.5 Comparison of finite-element and analytical flux density in airgap and yoke

It is observed that with skewed slot at 1.6 times slot pitch in the airgap, flux density wave shape is more sinusoidal. FEA is carried out for 2-D model, where skewing effect can not be observed. The yoke flux density with both the tools is observed; Yoke flux density variation is almost sinusoidal with analytical tool whereas it is flat toped from the FEM is seen from above figure.

Fig. 4.6 shows the torque calculation results, where analytical results have been calculated by considering a constant value of flux. It is seen that the finite element results, where saturation is also taken into consideration, gives less torque. This is the main reason to make torque results differ. Saturation is not only caused by the permanent magnets but also by load current and its angle vs. the q-axis [12].
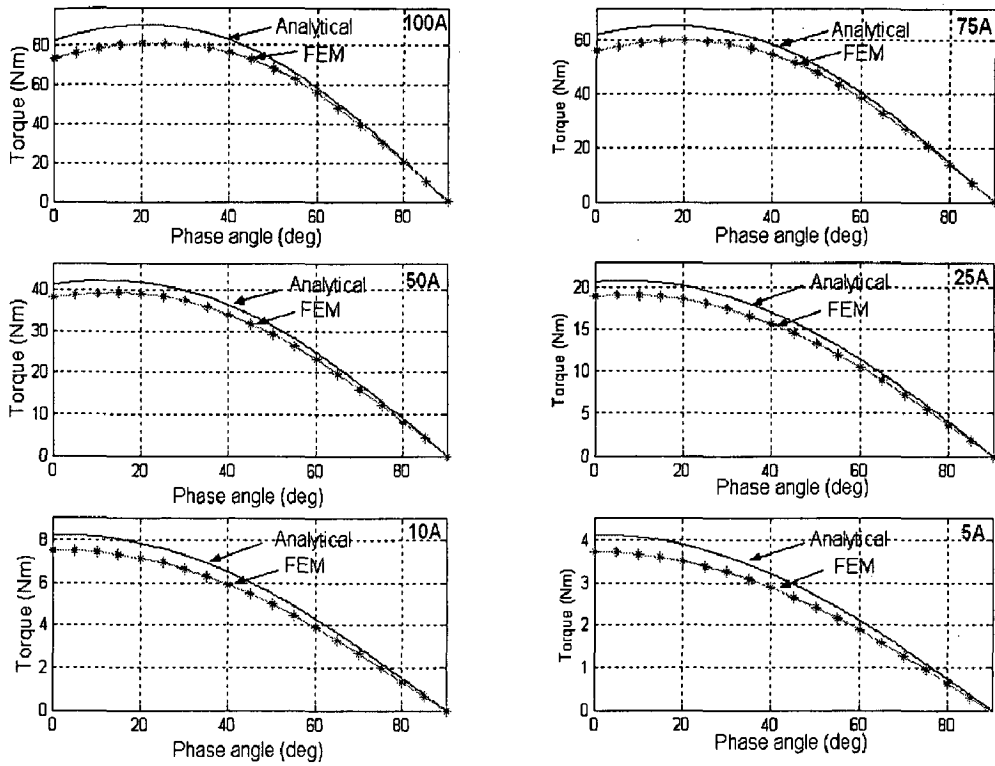
Fig. 4.6 Comparison of torque calculations

It should be noticed that L_d is slightly influenced by current phase angle and load condition and characterised by its linearity whereas L_q is severely affected by both factors due to saturation.

4.4.2 Comparison of Analytical and FEA to Experimental Results

The accuracy of the described results in the above section is examined in comparison to experimental results. Fig. 4.7 shows the vector diagram of the PMSM in the q-d co-ordinates. It is difficult to measure the inductance in load condition, thus an indirect method by the way of vector diagram is applied.

A method is used, where the induced EMF and the d-axis reactance are determined in a no-load test and the q-axis reactance is determined in a load test with different torques [13]. The load angle δ is determined from the load test by means of analytical method.
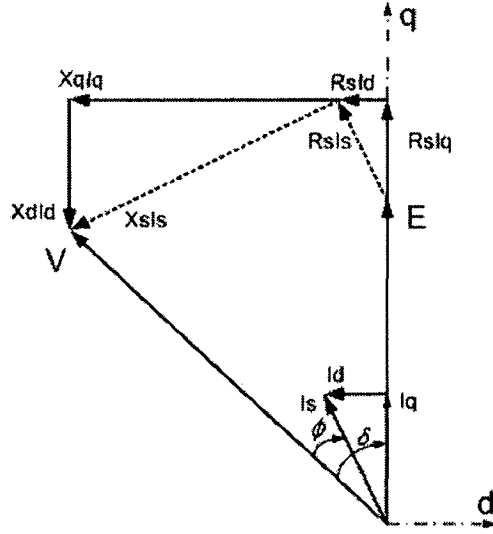
Fig. 4.7 Typical phasor diagram of a loaded PMSM

From the phasor diagram, it is obvious that

$$X_d = \frac{V\cos(\delta) - E - R_s I_q}{I_d} \tag{7}$$

$$X_q = \frac{V\sin(\delta) + R_s I_d}{I_q} \tag{8}$$

$$I_d = I_s \sin(\phi - \delta) \tag{9}$$

$$I_q = I_s \cos(\phi - \delta) \tag{10}$$

where E is the no load electromotive force, V is applied voltage, R_s represents the stator phase resistance, X_d and X_q are the reactances in the d and q directions, respectively, ϕ is the angle between the stator current I_s and voltage V, and I_d and I_q are the d- and q- axis components of the stator current.

The analytical and measured induced emf at 750 RPM is shown in Fig. 4.8. Table 4.1 summaries the different in results of analytical and FEM with measurement. Experimental set up and detail results can be referred in Appendix C.
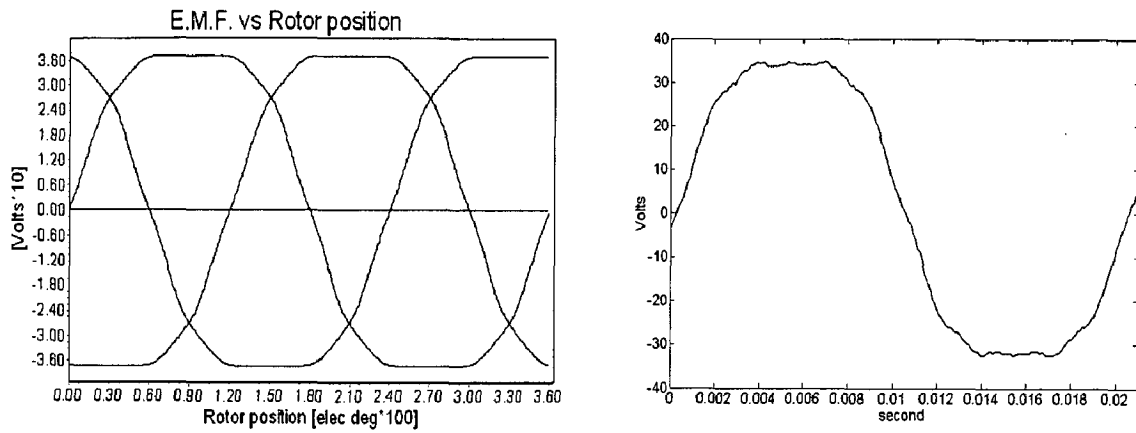
Fig. 4.8 Theoretical and experimental induced emf waveform

Table 4.1: Comparison of experimental results with Analytical and FEM calculations

	Analytical	FEM	Experimental
L_q (mH)	1.626	1.503	1.599
L_d (mH)	0.976	0.989	0.941
Torque (Nm) at $I_s = I_q = 90A$	74.296	66.249	70

Chapter 5

PMSM Drives

5.1 Introduction

Permanent magnet synchronous motors (PMSMs) are widely used due to their high torque to inertia ratio, higher power density and efficiency. There are a great variety of PMSM drives. Generally, these drives may be described by the block diagram in Fig. 5.1. The PMSM drive is seen to consist of four main parts: a power converter, a PMSM, sensors and a control algorithm. The power converter transforms power from source (such as battery in EV) to the proper form to drive the PMSM, which, in turn, converts electrical energy to mechanical energy. One of the salient features of the PMSM drive is the rotor-position sensor (or observer in sensor less drive). Based on the rotor position and a command signal(s), which may be a torque command, voltage command, speed command, and so on, the control algorithm determine the gate signal to each semiconductor in the power electronic converter.
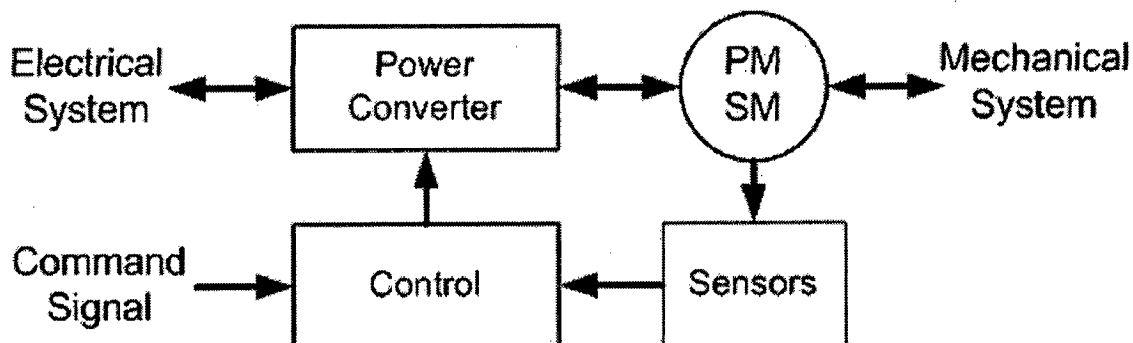
Fig. 5.1 PMSM Drive

Interior-permanent-magnet synchronous machines (IPMSM) are mechanically robust and thus allow high-speed applications. As discussed in Section 2.3.1, in these machines the effective air gap is small and therefore the effects of armature reaction are significant. This allows the control of the synchronous machine in the constant-torque region as well as in the flux-weakening (constant-power) region up to a high speed. Furthermore, in IPM machine the q-axis stator inductance L_q is larger than the d-axis stator inductance L_d and this is the distinct difference from the conventional electrically excited salient-pole synchronous machine. In practice, there can exist inductance ratios

L_q/L_d as high as five. The extra inductance can be helpful as it allow the use of lower switching frequencies for the IPMSM than those used with other inverter-fed machines. The PMSM without damper winding is controlled by self-controlled mode, in which inverter frequency is always controlled with the rotor frequency.

5.2 Control of IPMSM

The basic construction and mathematical model of IPM in rotor reference frame were discussed in Chapter 2. The torque developed in an IPM machine has two components: (1) the component due to the interaction of the magnet flux and q-axis stator current, and (2) the reluctance torque component, which is proportional to the difference of stator q- and d-axis inductances. The torque expression derived in Chapter 2 is rewriting here,

$$T_e = \left(\frac{3}{2}\right)\left(\frac{P}{2}\right)(\lambda_m^r i_{qs}^r - (L_q - L_d)i_{qs}^r i_{ds}^r) \tag{5.1}$$

This equation identifies two torque components. In surface permanent magnet (SPM) machine, the reluctance torque is practically zero, thus giving only the first components in equation (5.1). Equations (5.1) and (2.17) to (2.24) are used for the development of the vector-control system of the PMSM. There are many ways to implement of vector control of IPMSM, for example: (1) implementation of the stator-flux-oriented control of IPMSM (2) implementation of the rotor-oriented control of the IPMSM. Here, rotor-oriented control of the interior permanent magnet synchronous machine is described and implemented in Matlab Simulink in both constant-torque and flux-weakening regions.

5.2.1 Current Vector Control in Constant Torque Region

It is assumed that the d-axis of the special reference fame is aligned with the magnet flux (rotor oriented control) and the stator current components expressed in the rotor reference frame are controlled to control the torque. In constant torque region, it is possible to control the IPMSM with the maximum torque per ampere (MTPA) principle to minimize electrical losses, that is, to optimize the drive efficiency. This implies a minimum converter rating as well as its maximum efficiency.

To obtain generally applicable functions for the MTPA, for any IPMSM, a normalized torque-current relationship is obtained and used (in) as lookup table in the algorithm. Defining the base torque as

$$T_{eB} = \left(\frac{3}{2}\right)\left(\frac{P}{2}\right)(\lambda_m^{'r} I_B) \tag{5.2}$$

where T_{eB} and I_B are the base value of torque and current respectively. The base current I_B defined as

$$I_B = \frac{\lambda_m^{'r}}{L_q - L_d} = I_f \frac{L_{md}}{L_q - L_d} \tag{5.3}$$

Convenience

The fictitious field current I_f in the machine can be treated as a constant. The defined T_{eB} and I_B are for conventions only, and are not related to rated or maximum machine ratings. Substitutions of equations (5.2) and (5.3) in (5.1) yields

$$T_e(pu) = \frac{T_e}{T_{eB}} = \frac{i_{qs}^r}{I_B} - \frac{i_{ds}^r}{I_B}\frac{i_{qs}^r}{I_B} \tag{5.4}$$

$$T_e(pu) = i_{qs}^r(pu)[1 - i_{ds}^r(pu)] \tag{5.5}$$

where $i_{qs}^r(pu)$ and $i_{ds}^r(pu)$ are normalized values of the two-axis current in the rotor reference frame.

Thus, it is possible to plot the constant-torque loci of the IPMSM in terms of the normalized values of the two-axis stator currents $i_{qs}^r(pu)$, $i_{ds}^r(pu)$. This is shown in Fig. 5.2 with blue lines, where on every locus the point which nearest to the origin corresponds to the minimum stator current, so that the maximum torque per stator ampere curve (red line) is obtained by connecting points CBAOabc. For positive torque, the polarity of i_{qs}^r is positive, whereas the polarity of i_{ds}^r is negative. Negative i_{ds}^r contributes an additive reluctance torque component in the equation (5.1). The polarity of torque can be reversed by reversing the i_{qs}^r current. The Fig. 5.3 shows the plot of optimum $i_{qs}^r(pu)$ and $i_{ds}^r(pu)$ currents as functions of normalized torque $T_e(pu)$, which are derived from Fig. 5.2. The information from Fig. 5.3 can be used to develop the MTPA lookup table, which is implemented in Fig. 5.4.
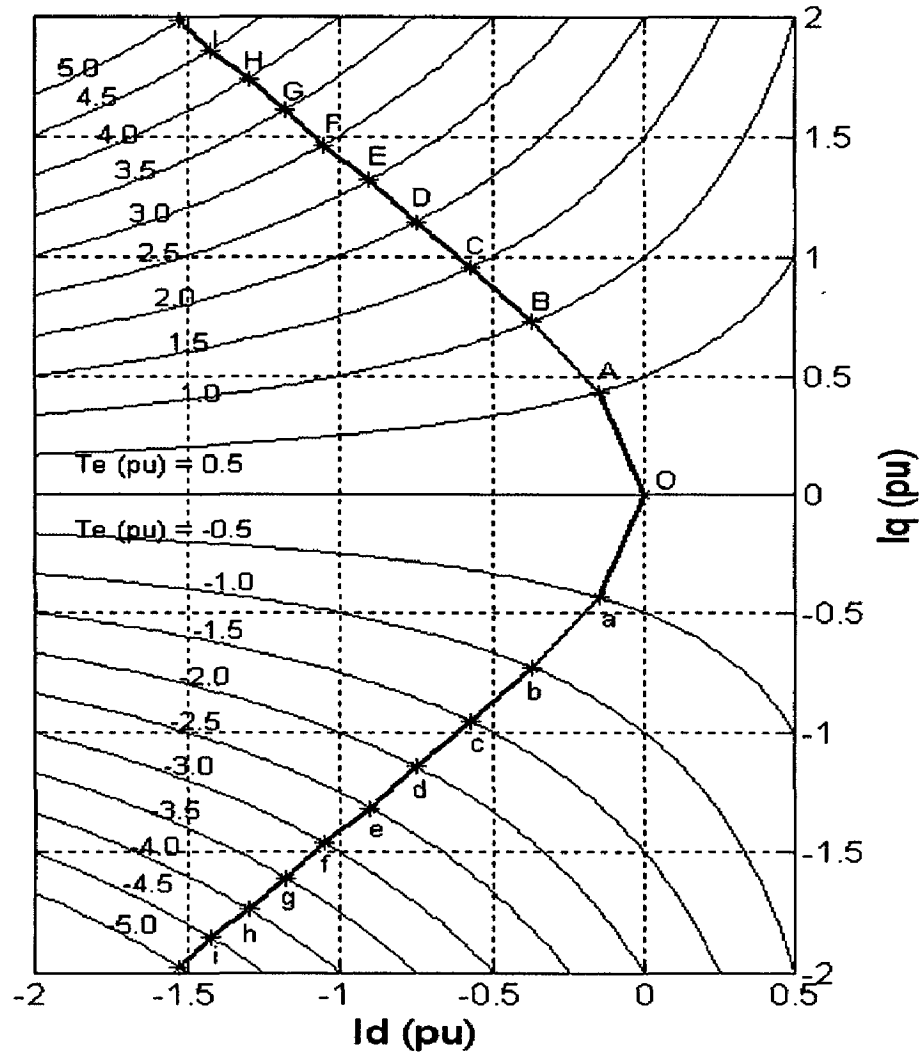
Fig. 5.2 MTPA trajectory on constant torque loci
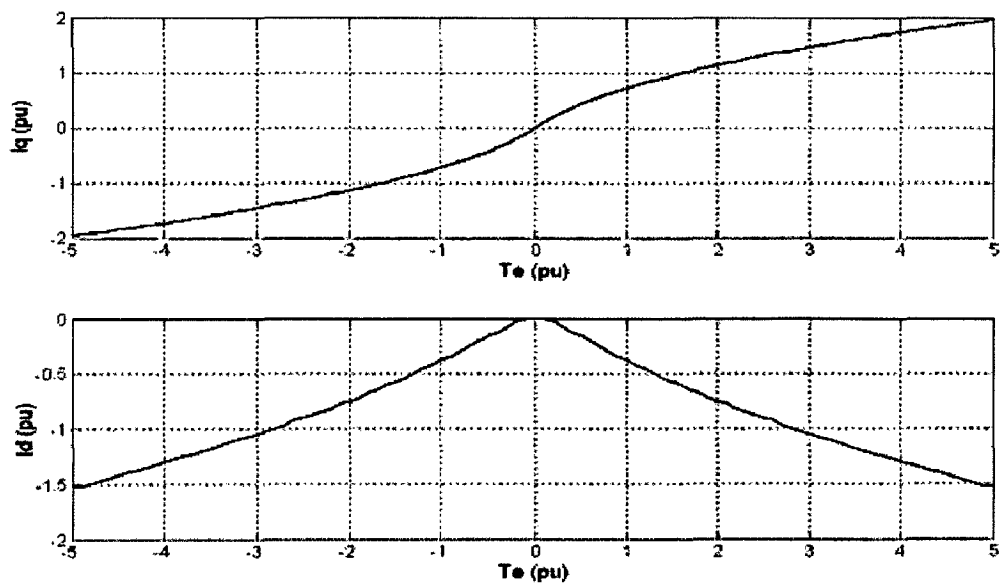
Fig. 5.3 $i_{qs}^{r}(pu)$ and $i_{ds}^{r}(pu)$ as function of $T_e(pu)$ for MTPA

61
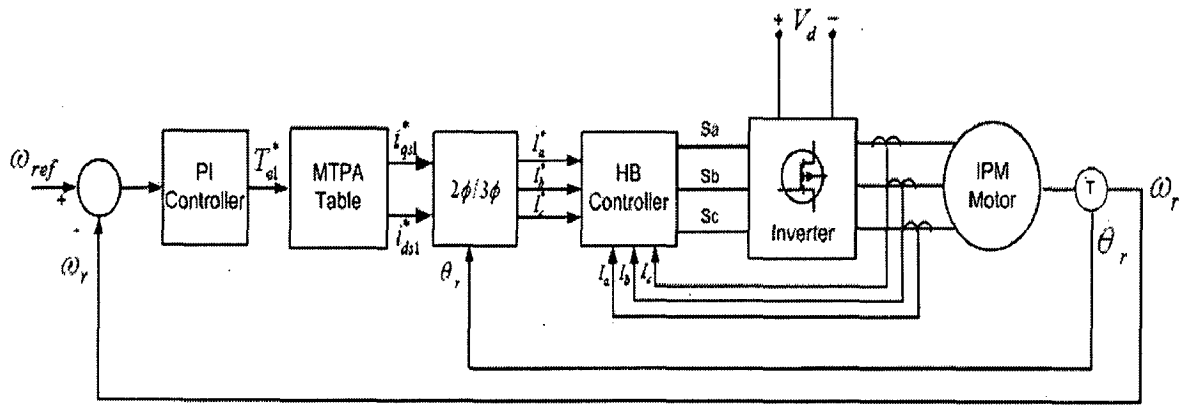
Fig. 5.4 Speed control of IPM motor with MTPA algorithm. (constant torque region only)

In Fig.5.4, the speed control loop generates the torque command T_{el}^*. From this command T_{el}^*, current command i_{qs1}^* and i_{ds1}^* are generated with the help of MTPA table. In MTPA table, the values from Fig. 5.3 are used. The actual value of torque command T_{el}^* first normalized with base torque based on machine parameter and then q-d current command are generated from the base torque. This q-d current command are again reformed to actual value by multiplying base current. The absolute position signal θ_r converts the rotor rotating frame signal i_{qs1}^* and i_{ds1}^* into stationary reference frame signal I_a^*, I_b^*, and I_c^*. Based on I_a^*, I_b^*, and I_c^* current command and the actual currents I_a, I_b, and I_c, the on and off status of each semiconductors is determined using the hysteresis band (HB) current control strategy.

Limitations:

1. The simple feedforward current control described above will work correctly if the machine parameter variation effect is neglected. In practice, the parameter variation (i.e. $\lambda_m^{'r}$, L_q and L_d) effect in MTPA table will cause incorrect distribution of $i_{qs}^r(pu)$ and $i_{ds}^r(pu)$ currents.

2. It is only possible to obtain satisfactory operating characteristics of the drive described above at low frequencies. The control algorithm valid in the constant torque region, where PWM control of the inverter permits control of the desired currents.

It is possible to achieve torque control at high speed, in the flux-weakening mode, by commanding the demagnetizing components of the stator currents to keep the PWM controllers from saturating completely. This operating mode is different from the MTPA conditions because of the voltage limitations of the inverter.

5.2.2 Current Vector Control in Flux-Weakening Region

As discussed above, saturation of the current controllers of the current-controlled PWM inverter occurs at higher rotor speeds when the terminal voltages of the motor approach the ceiling voltage of the inverter. The rotor speed and inverter dc voltage (in case of EV where DC voltage is not constant) is an important factor which determines the saturation of the current controllers, since both the motor reactances and the induced stator emfs are proportional to the excitation frequency, which is synchronized with the rotor speed in order to yield smooth responsive torque control.

Another reason to go for flux-weakening region is to utilize the IPM motors stronger armature reaction capabilities. IPM motors has less air gap, which makes the magnetizing inductance larger; this implies that in IPM machine stator current has a stronger effect in weakening the flux that link the stator winding. This flux-weakening capability permits the drive to operate in extended speed range, beyond the base speed (the rotor speed where inverter saturates), useful for EV application.

Based on the discussion above, the inverter has to be operated in different mode based on speed of operation. The PWM and square wave (SW) modes are inverter modes for constant torque and flux-weakening control respectively. In SW mode, the available peak value of fundamental stator voltage is $V_S = 2V_d/\pi$, where V_d is dc link voltage of the inverter. This is related to steady-state V_{qs}^r and V_{ds}^r components of stator phase voltage as

$$V_S = \sqrt{(V_{qs}^r)^2 + (V_{ds}^r)^2} \tag{5.6}$$

where

$$V_{qs}^r = \omega_r L_d i_{ds}^r + \omega_r \lambda_m^{'r} \tag{5.7}$$

$$V_{ds}^r = -\omega_r L_q i_{qs}^{'r} \tag{5.8}$$

and Stator current can be related as

$$I_S = \sqrt{(i_{qs}^r)^2 + (i_{ds}^r)^2}$$ (5.9)

Equations (5.7) and (5.8) are derived from (2.10) and (2.11), respectively, at steady-state condition and neglecting the stator resistance drop. Rewriting the equation (5.6) with substituting the values of V_S, V_{qs}^r and V_{ds}^r.

$$\frac{4V_d^2}{\pi^2} = (\omega_r L_d i_{ds}^r + \omega_r \lambda_m^{'r})^2 + (-\omega_r L_q i_{qs}^r)^2$$ (5.10)

which can be modified to form

$$\frac{\left(i_{ds}^r + \dfrac{\lambda_m^{'r}}{L_d}\right)^2}{\left(\dfrac{2V_d}{\pi\omega_r L_d}\right)^2} + \frac{\left(i_{qs}^r\right)^2}{\left(\dfrac{2V_d}{\pi\omega_r L_q}\right)^2} = 1$$ (5.11)

This is an equation of an ellipse in the form

$$\frac{\left(i_{ds}^r + C\right)^2}{\left(A\right)^2} + \frac{\left(i_{qs}^r\right)^2}{\left(B\right)^2} = 1$$ (5.12)

where

$$A = \frac{2V_d}{\pi\omega_r L_d} \quad \text{is the length of semi-major axis}$$ (5.13)

$$B = \frac{2V_d}{\pi\omega_r L_q} \quad \text{is the length of semi-minor axis}$$ (5.14)

$$C = -\frac{\lambda_m^{'r}}{L_d} \quad \text{offset of the centre on the Id axis}$$ (5.15)

For any value of the rotor speed, the stator current phasor is directed away from the origin of the complex q-d plane to a point on the ellipse, but because there is a maximal voltage, it must be always located inside the ellipse. Such an ellipse will be referred as a voltage-limit ellipse and is shown in Fig. 5.5, which is constructed using the designed machine parameter. For increasing rotor speed, there is a group of ellipses, where the axes of the ellipse are inversely proportional to the rotor speed.

To achieve maximum torque in flux-weakening region, the machine must be operated in both voltage and current limited mode simultaneously, which can be described as the intersection of the voltage and current limit.
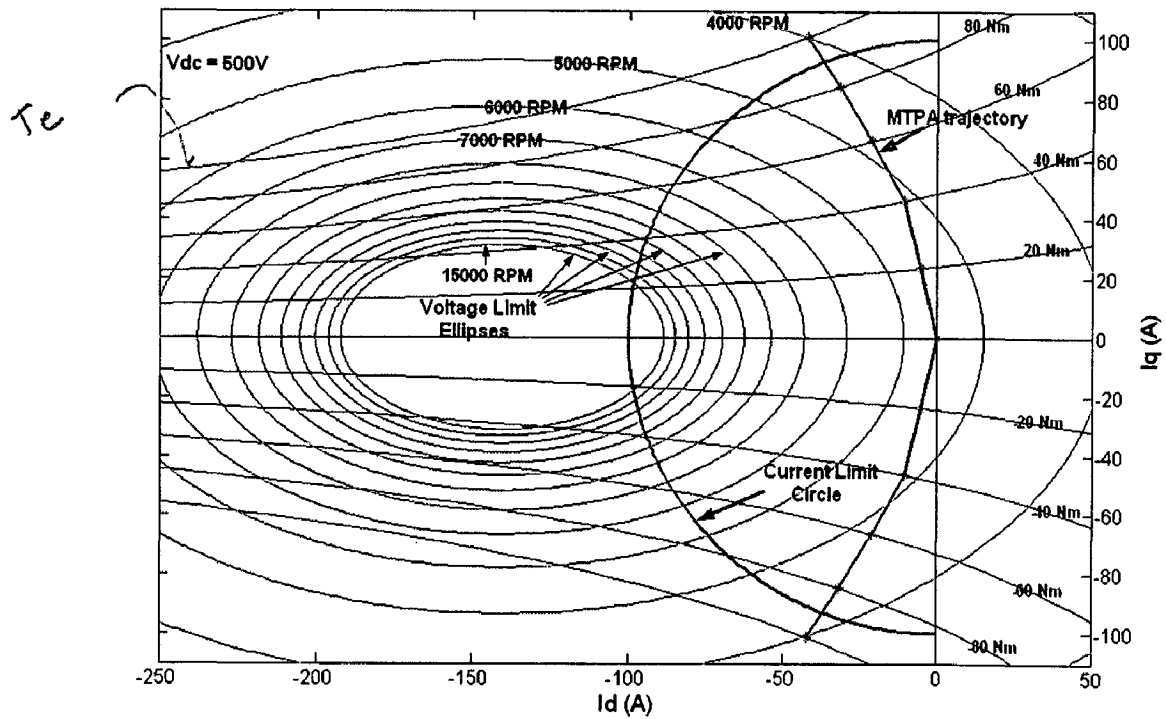
Fig. 5.5 Current and Voltage constraints regions

5.3 Implementation of proposed control algorithm

5.3.1 Torque Command Generation and Selection

It can be seen from Fig. 5.5 that in the flux-weakening mode of operation, the IPMSM has less maximum torque capability than constant torque mode and this maximum torque capability inversely proportional to the speed. Another factor depends on this is dc link voltage V_d. From equation (5.11), for a specific voltage, a set of q-d axis current value can be obtained, which forms an ellipse. Now, out of this set of q-d axis current value, the complex sum of q-d axis current is limited by maximum stator current (100A in the current case). For the available maximum stator current, relation of speed and torque using equations (5.1), (5.9) and (5.11) for different dc link voltage can be developed. The torque-speed curve for different voltage is shown in Fig. 5.6. From above discussion, it can be concluded that based on the current speed and available dc link voltage, how much maximum torque can be produced by the machine can be found out. These values from Fig. 5.6 can be stored in 2-dimensional table where speed and voltage will be input and torque T_{e2}^* will be output. The above calculations can also be simplified

by considering V_d/ω_r ratio, for a specific value of V_d/ω_r ratio, there will be a unique value of torque, so, instead of using 2-dimensional table, 1-dimesional table can also be used, where V_d/ω_r ratio will be input and torque T_{e2}^* will be output.
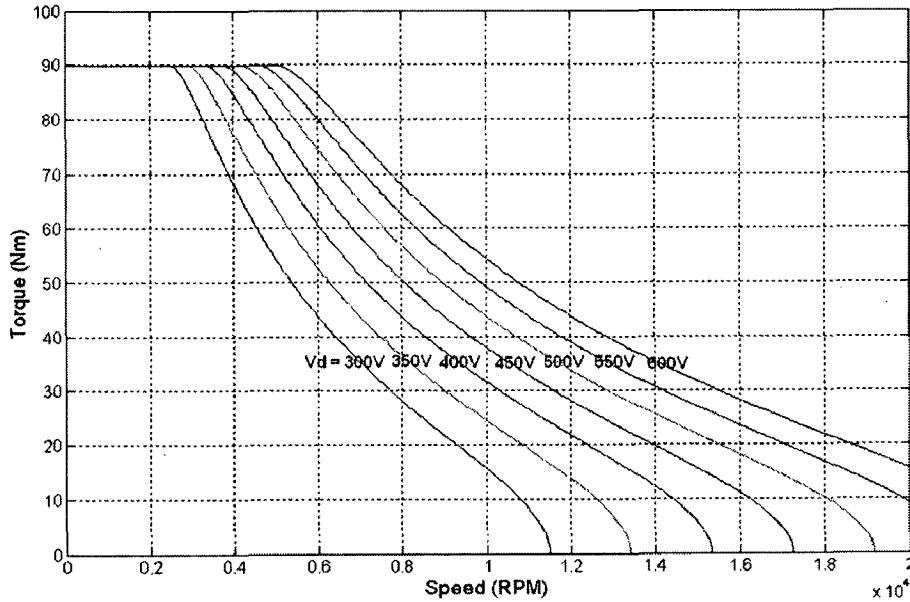
Fig. 5.6 Torque-Speed relation for different voltages

It is better to incorporate MTPA algorithm with flux-weakening algorithm. In this case, there will be two torque commands generated, one is T_{e1}^* (Fig. 5.4) from speed controller which does not depend on flux weakening and another is T_{e2}^* from speed and dc link voltage which look for the maximum torque capability in the complete operational range of speed. Out of these two torque commands, the T_{e2}^* will limit maximum allowable torque to maintain operation in flux-weakening mode. The block diagram of torque command generation and selection is as shown in Fig. 5.7.
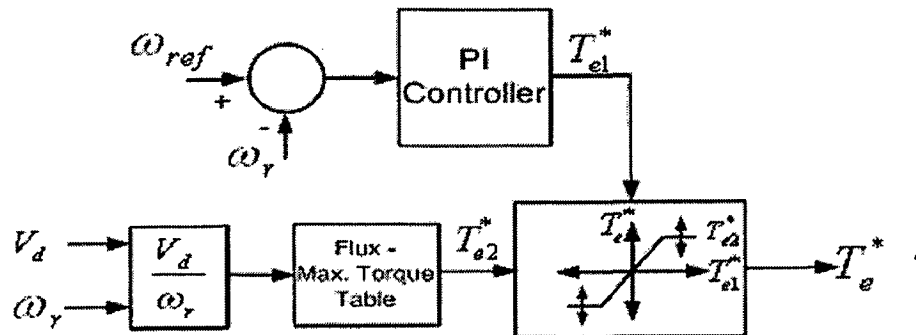
Fig. 5.7 Block diagram for torque command generation and selection

66

5.3.2 Current Command Generation and Selection

As discussed in Section 5.2.1, current commands are generated from the torque command T_{el}^*. These i_{qs1}^* and $i_{ds1}^*$ are based on MTPA table and valid till base speed and for constant torque. Above base speed, the torque can be generated from the machine that has to be reduced by the command of q-d axis current. That means the current vector has to be moved on left side in Fig. 5.5. In flux-weakening mode, q-d axis current can be precalcuated based on the speed, torque and dc link voltage. This implies that the crossover point of constant torque loci and voltage limited ellipse for a speed will give a set of q-d axis current. Of course the inputted torque will be inside current limited circle as implemented in Section 5.3.1. This q-d axis current can be used to produce I_a^*, I_b^*, and I_c^* current commands. Again, instead of considering dc link voltage and speed separately, V_d/ω_r ratio has been taken in account to reduce the 3-dimesional table to 2-dimsional table. A value of V_d/ω_r ratio will give a set of q-d axis current command, which forms an ellipse. The cross over of this ellipse and command torque T_e^* loci will give a value of q-d current which can be said as q-d axis current command i_{qs2}^* and i_{ds2}^* respectively.

At this stage, there are two q- and d-axis current commands, i_{qs1}^* and i_{qs2}^* for q-axis current and i_{ds1}^* and i_{ds2}^* for d-axis current. As we know, i_{qs1}^* and i_{ds1}^* are generated for constant torque operation below the base speed and i_{qs2}^* and i_{ds2}^* for flux-weakening mode above base speed. Out of these two sets of q-d axis current, one set has to be selected based on machine operation. Now, important thing is base speed beyond which inverter saturates is different for different dc link voltage. As dc link voltage is higher, higher will the base speed, which can be seen in Fig. 5.6. Hence, base speed is not that much helpful to select machine operational mode or current command. Another way is to observe the i_{qs2}^* and i_{ds2}^* current command. This command has been generated based on crossover of ellipse and constant torque loci, which are inside the current limit circle. Of course this may be on left side of MTPA line or right side of MTPA line. So, based on i_{qs2}^* and i_{ds2}^* current command in q-d plane location on right half or left half of the MTPA

line, switching status is decided. It should be noted that, i_{qs2}^* and i_{ds2}^* current command has generated with consideration of dc link voltage, so, base speed variation based on dc link voltage has been taken in account automatically. The switching of current command selection can also be said as PWM of SW operation selection switch. The q-d axis current command generation and selection switch block diagram is as shown in Fig. 5.8.
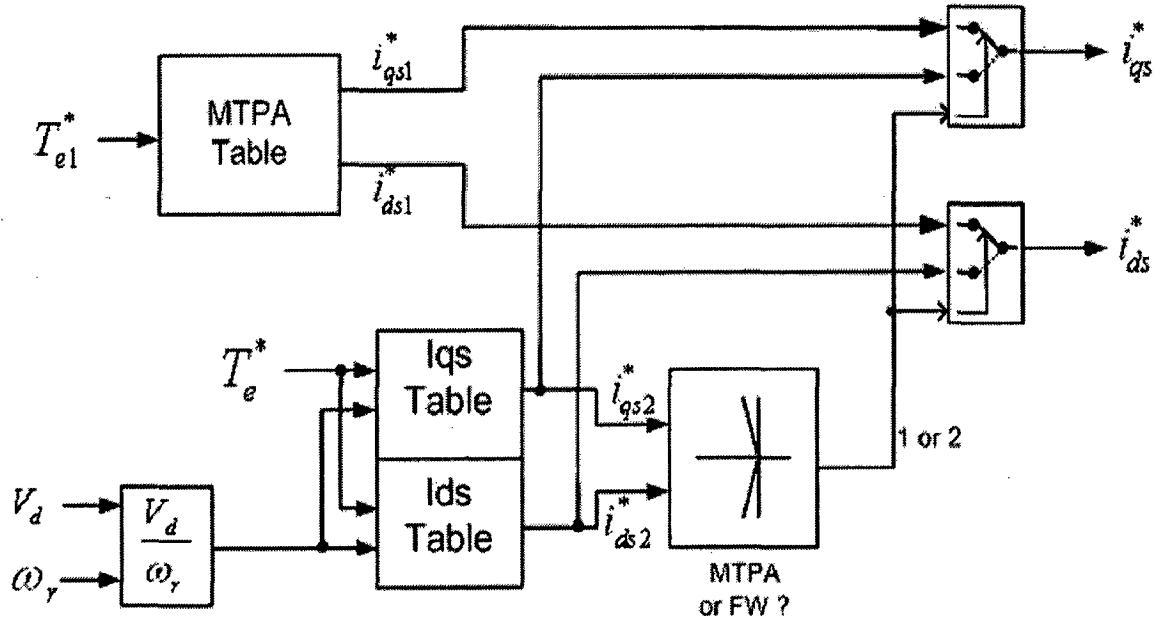

Fig. 5.8 Current command generation and selection block diagram

5.3.3 Current Regulated Inverter Drives

In vector control scheme, the current controlled has direct influence on the drive performance and its design requires special considerations. From above two sections, we can conclude that from speed reference torque command is produced, which is limited with the maximum torque limit envelop (Fig. 5.6). The new torque command is used to produce the q-d axis current command and machine has to run such a way that it should follow the commanded current. This implies the control algorithm adopted here is current regulated vector control inverter drive not the voltage source inverter drives. The main difference in volt-source inverter drives and current regulated drives is in the way in which the gate signals to the individual semiconductors are established.

Current regulated inverters have several distinctive features. First, because torque is function of the machine current, the torque may be controlled with the same bandwidth by which the stator currents are controlled. A second important feature of current regulated drives is robustness with regard to changes in machine parameters. For

68

example, current regulated drives are insensitive to parameter variations in the stator leakage inductance or stator resistance [05]. This drive is also robust to faults.

Fig. 5.9 shows the control of current regulated PMSM drive. Therein, the q- and d-axis current command, i_{qs}^* and i_{ds}^* are formulated based on the commanded torque T_{e1}^*, electrical rotor speed ω_r, and the dc link voltage V_d. Using inverse transformation, the corresponding a, b, c variable current command I_a^*, I_b^*, and I_c^* is determined. In hysteresis band controller, I_a, I_b, and I_c are forced to follow the reference current I_a^*, I_b^*, and I_c^* respectively, within a hysteresis band by switching action of the inverter.
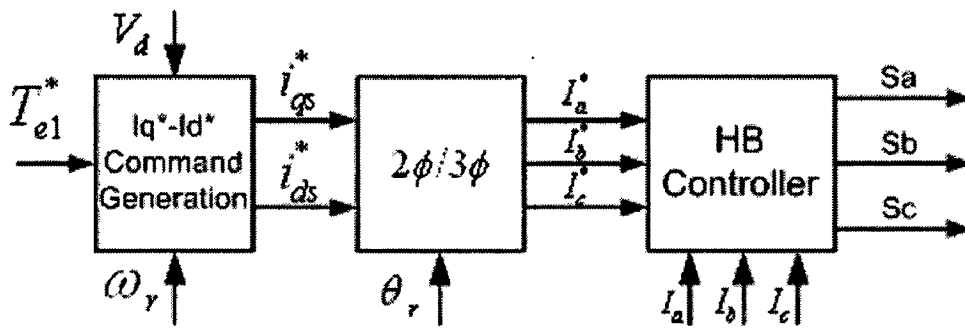
Fig. 5.9 Hysteresis current-regulated drive

Fig. 5.10 on next page shows the complete block diagram of current regulated PMSM drive system and Fig. 5.11 is part of the Fig. 5.10 of the block so called i_{qs}^* and i_{ds}^* command generation block. In this block complete algorithm for the constant torque and flux-weakening is incorporated, which is shown in Fig. 5.11. The flux command λ_L^* is limited with minimum and maximum value considering maximum and minimum dc link value and speed. For i_{qs}^* and i_{ds}^* command generation table, $\left| \lambda_L^* \right|$ is used, which represents an ellipse line for a V_d / ω_r ratio.
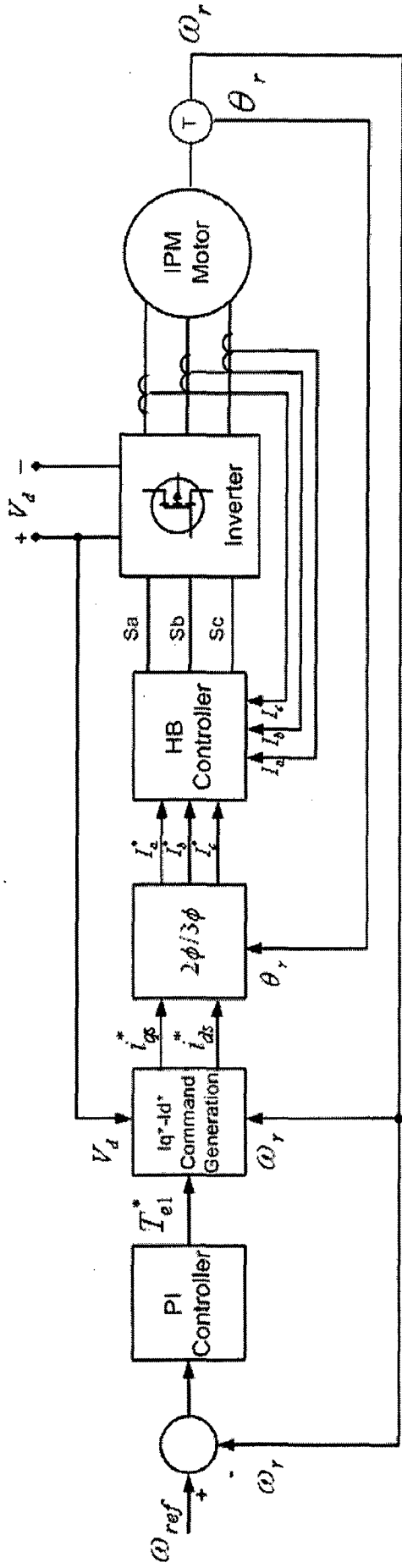
Fig. 5.10 Schematic block diagram of current regulated PMSM drive system
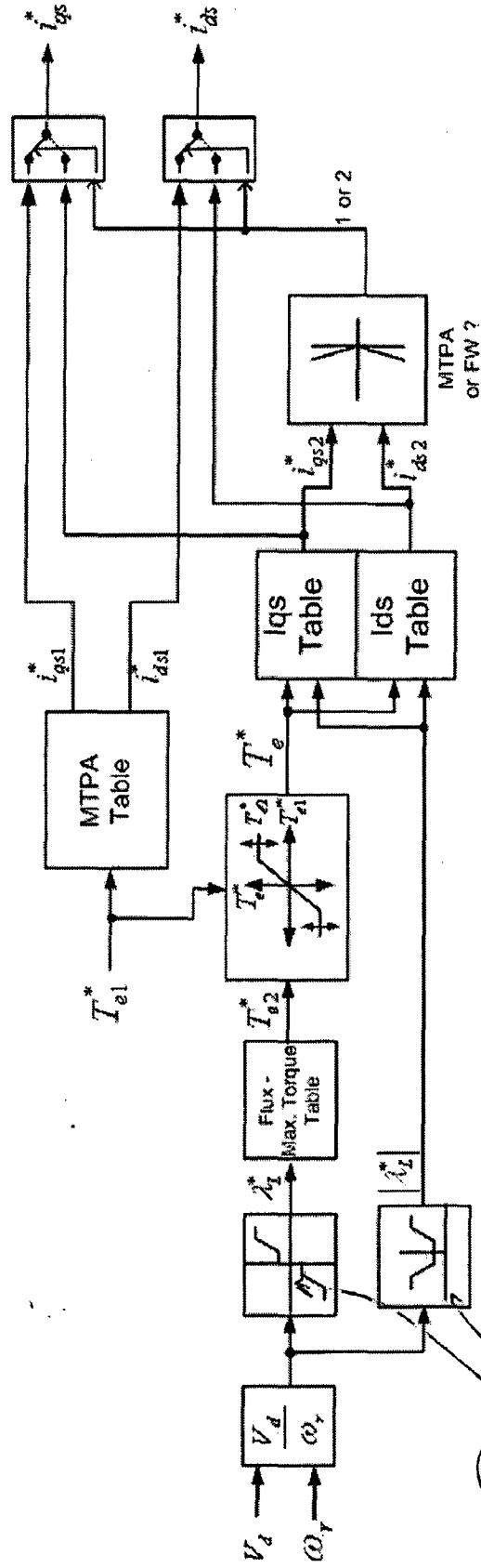
Fig. 5.11 Block diagram of the proposed algorithm

70

5.4　Simulation of PMSM Drive

The PMSM drive, proposed in Fig. 5.10 and Fig. 5.11, is simulated using the software package Matlab/Simulink programming environment, in which machine is modelled with designed machine parameter. The parameter variation is considered based on analytical and FEM calculations and lookup tables have been developed considering the effect of saturation and parameter variation. The speed controller and current regulation with hysteresis band (HB) has been included in the simulation. Every instant of a power device switching on and off is decided with the hysteresis band current controller. Fig. 5.11 shows the block diagram of simulated drive in time domain.
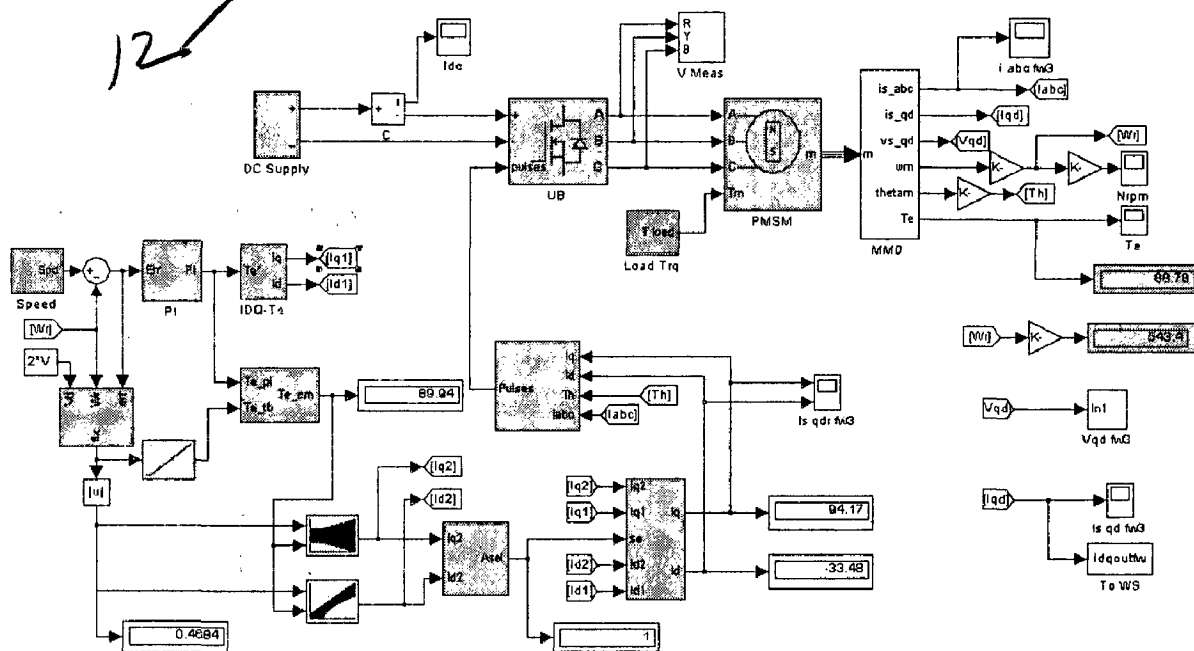
Fig. 5.12 Simulation block diagram

Simulation in Constant Torque Region

Fig. 5.12 shows the simulated response of the drive in constant torque region, where the speed reference given as 3000 RPM. Under this speed, the torque has been varied at different time interval is shown in Fig. 5.13 (b). The q-d axis current has been tracked under the MTPA line, this mode of operation can be seen in Fig. 5.13 (c) and (e). The line current variation is also shown, in which the frequency of line current is changing based on the speed of operation is observed.

71
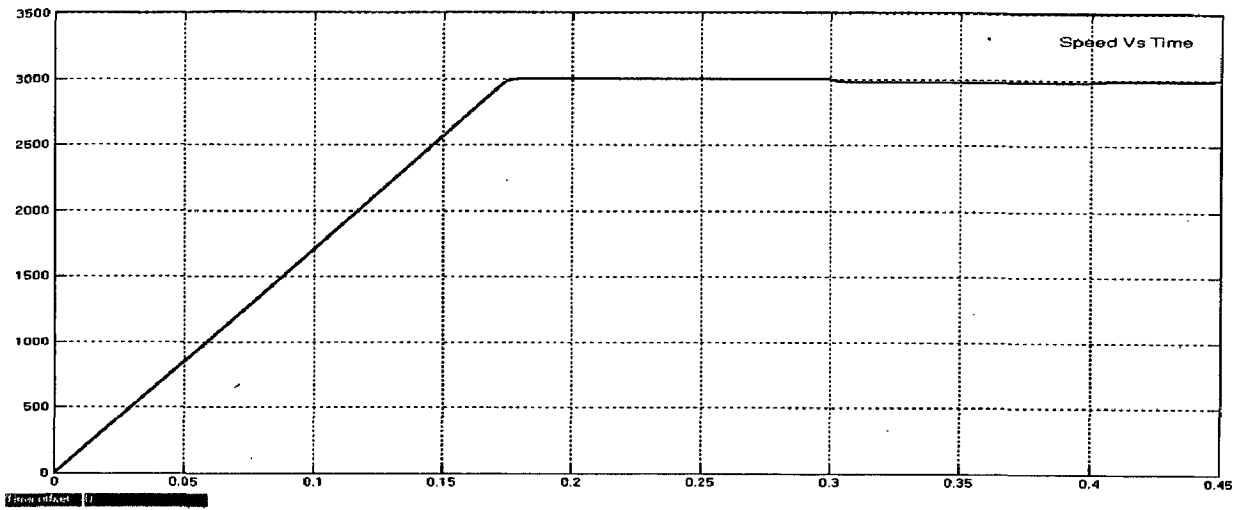
(a) Speed (RPM) Vs Time
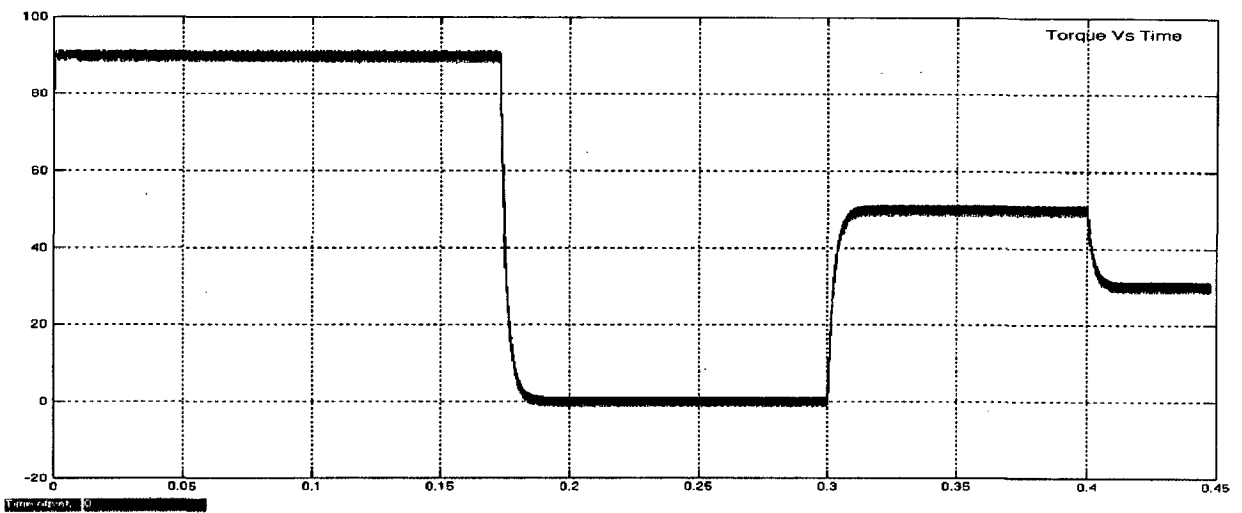
(b) Torque Vs Time
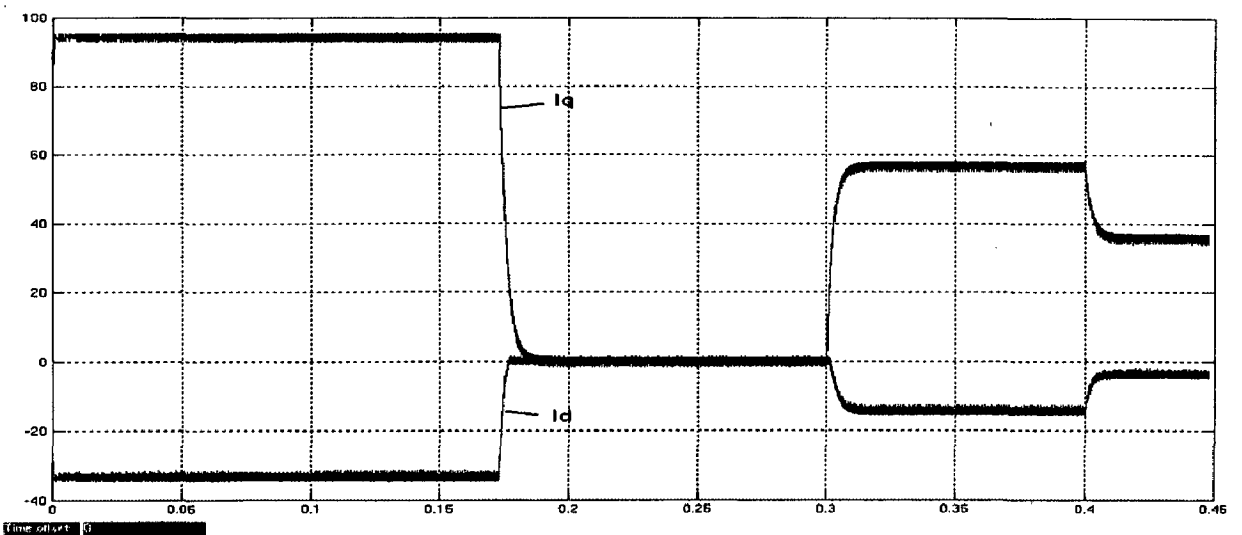
(c) Change in Iq and Id

Fig. 5.13

72
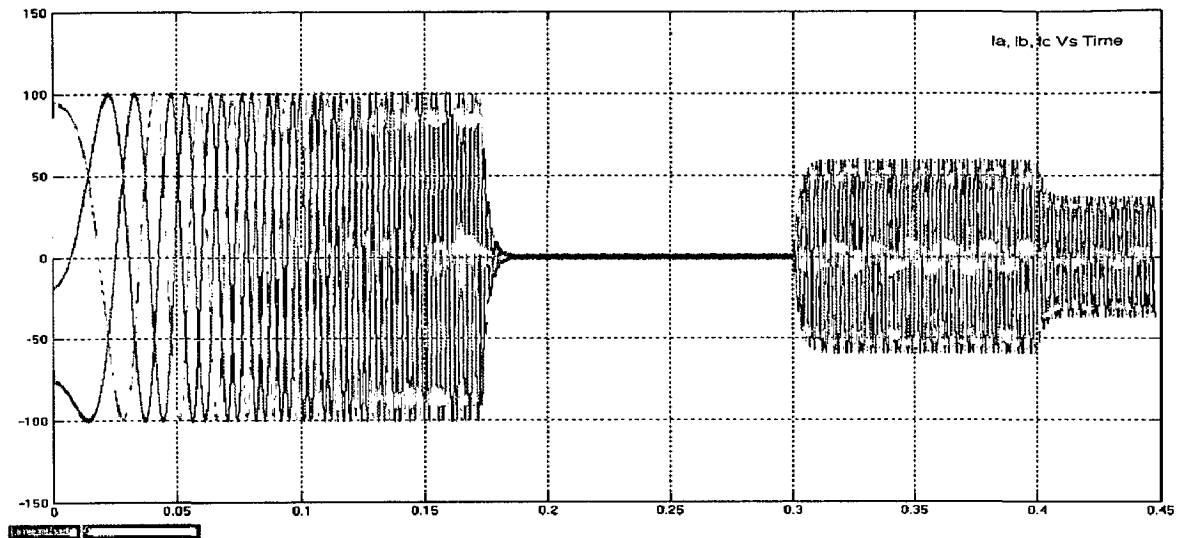
(d) Change in Ia, Ib, Ic
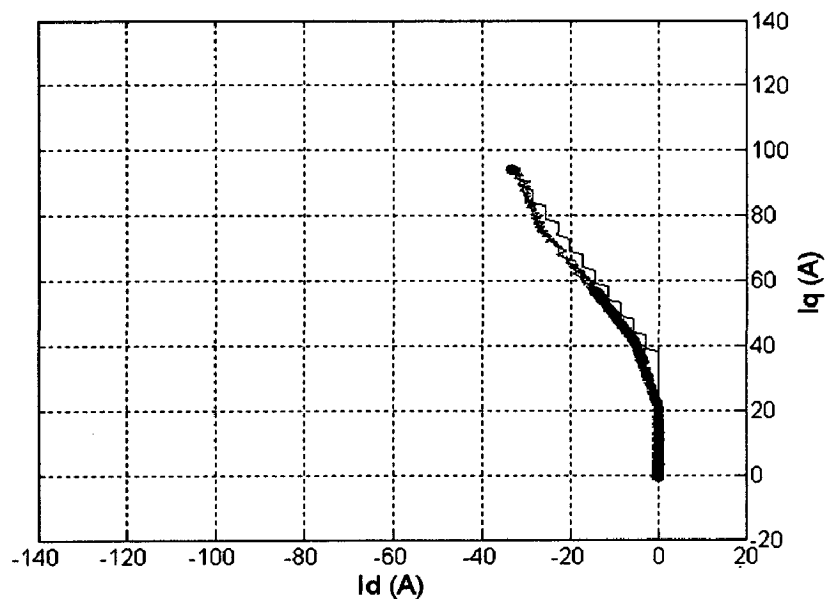
(e) *q, d* current loci

Fig. 5.13 Dynamic performance of drive in constant torque region

Simulation in Flux-Weakening Region

The drive performance under flux weakening region is simulated in proposed scheme and the simulated results is shown in Fig. 5.14. In this case, the reference speed is 7000 RPM, which is more than base speed for applied dc voltage i.e. 500V. Till time 0.45s load torque applied is zero and motor reaches to reference speed, as motor speed is more than base speed and no load torque, in this condition, motor need to draw *d*-axis current only is seen from Fig. 5.14 (c) and (d) and from line reactive current will be

drawn. The changeover from constant torque to flux-weakening can be observed from Fig. 5.14 (b), (c) and (d). As motor enter in the flux-weakening mode, the torque command traces the curve based on Fig. 5.6 and q-d axis current axis command will trace the current limit circle. Further, as soon as motor reaches the reference speed in flux-weakening mode q-d axis current traces the constant voltage ellipse and it will stabilized at crossover points of ellipse of reference speed and torque loci. Fig. 5.14 (e) shows the results from [28] which are compared with simulation results.
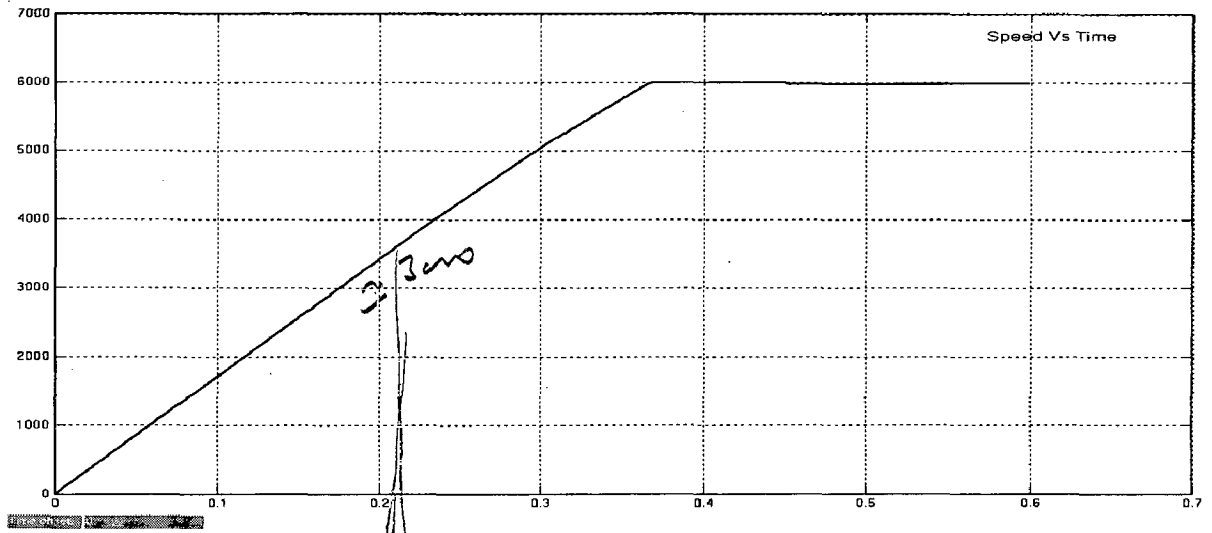
(a) Speed (RPM) Vs Time
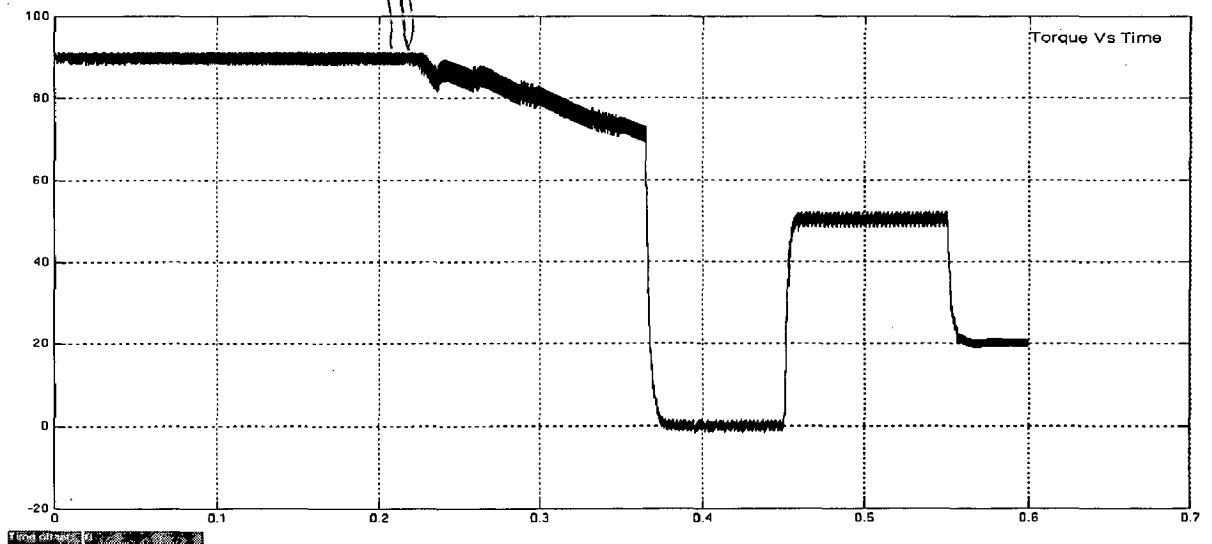
(b) Torque (Nm) Vs Time

Fig. 5.14
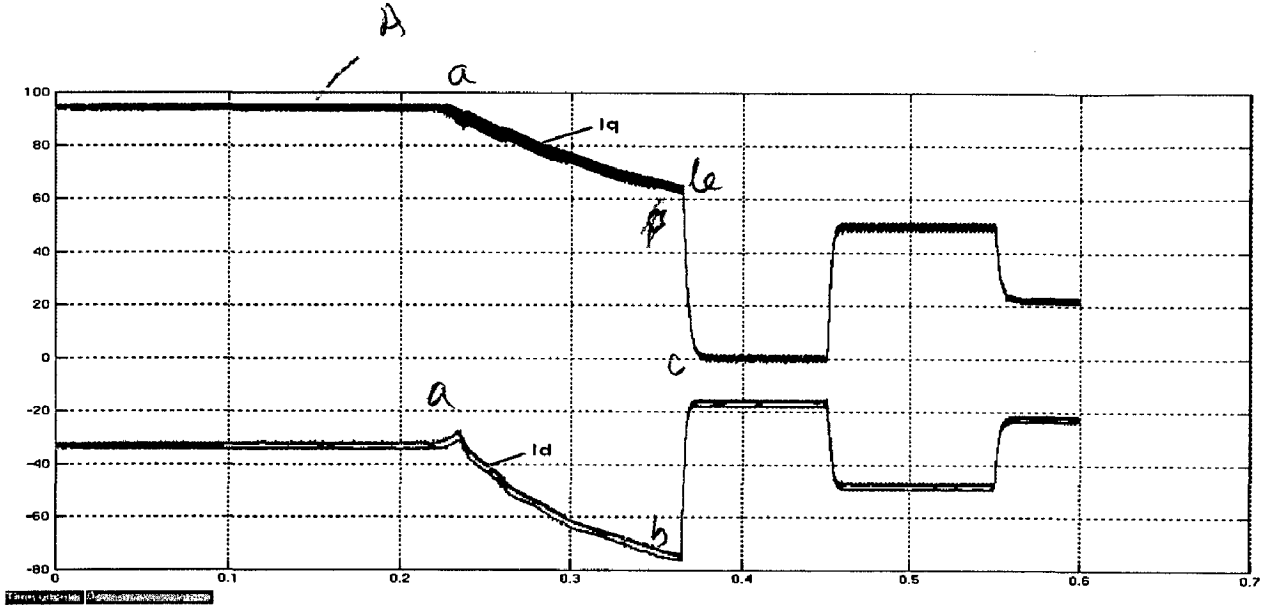
(c) Change in Iq and Id
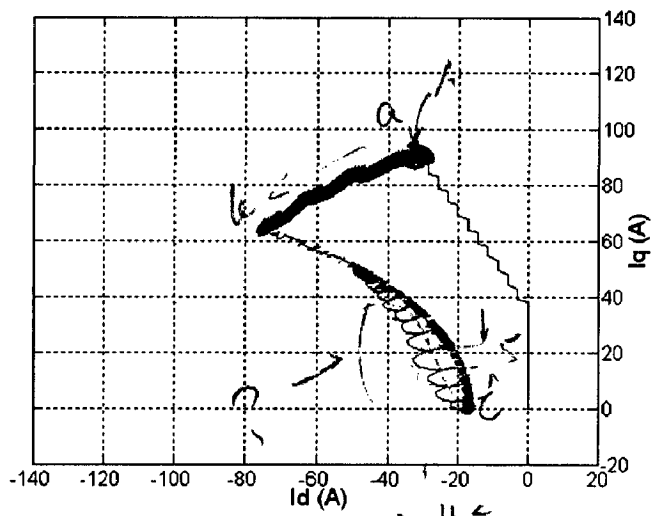
(d) q, d current loci
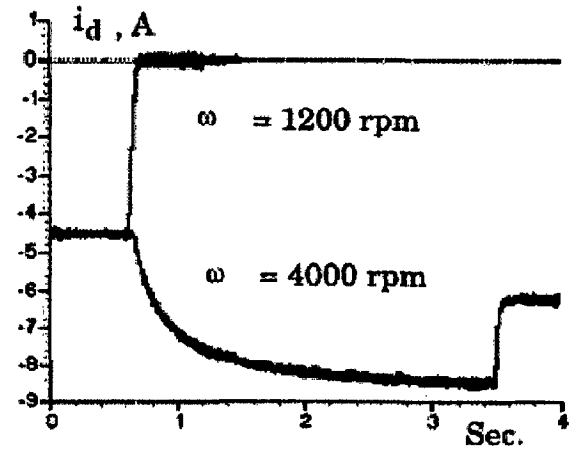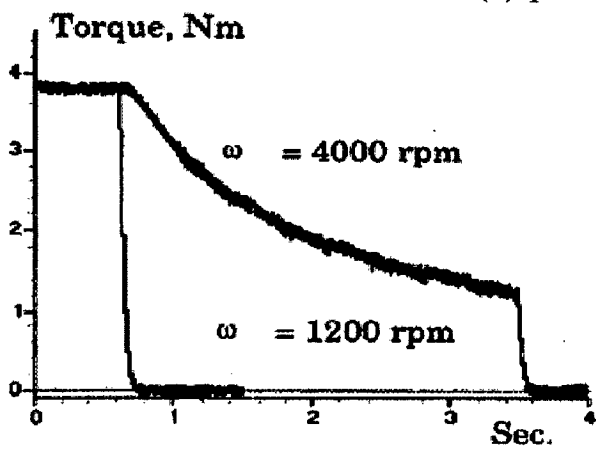
Torque response d-axis current response

(e) Results of reference [28] for comparison of simulation results

Fig. 5.14 Dynamic performance of drive in flux-weakening region

The performance of the drive in the regenerative mode has been observed by reducing the speed reference from higher to lower value. Fig. 5.15 shows the drive operation in the 3rd and 4th quadrant in q-d complex plane where initially motor reached to 7500 RPM, at time 0.65s motor reference has been reduced to 3500 RPM, so, motor operation jumps to 4th quadrant, where both q- and d-axis currents are negative. The current command will trace maximum current circle loci and developed torque capacity increases negatively and speed reduces. At the moment when motor reaches to reference speed and no torque applied than q-d axis current command drops to zero if speed is in constant torque region.
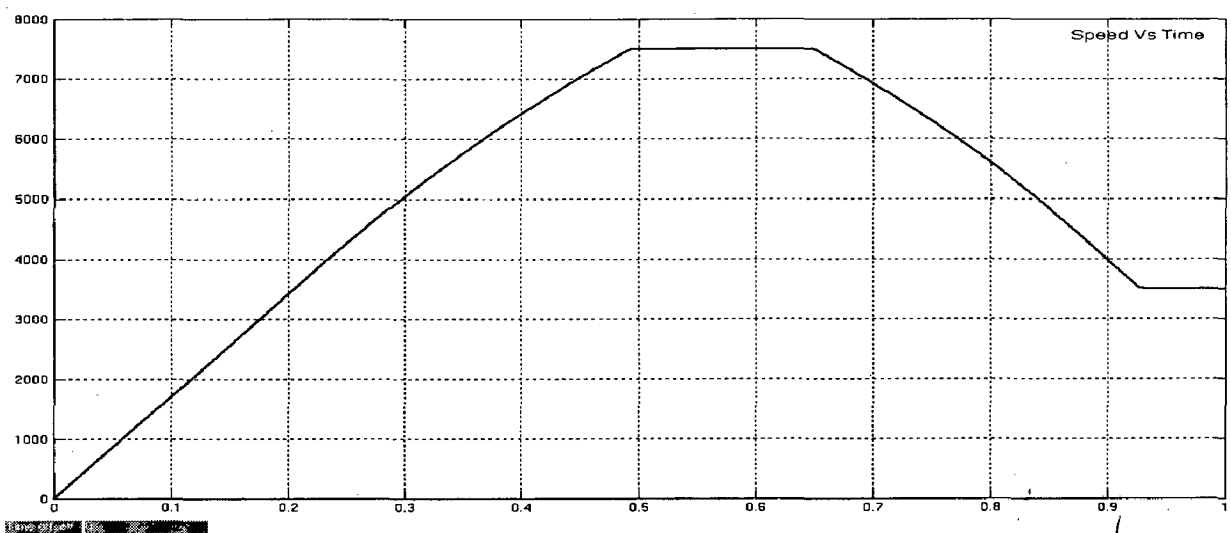
(a) Speed (RPM) Vs Time
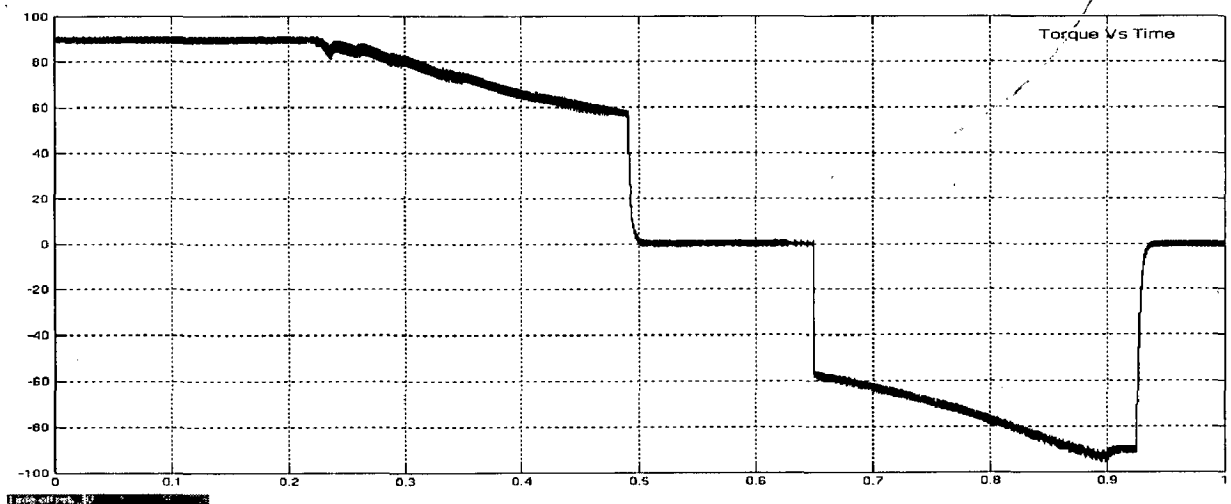
(b) Torque (Nm) Vs Time

Fig. 5.15
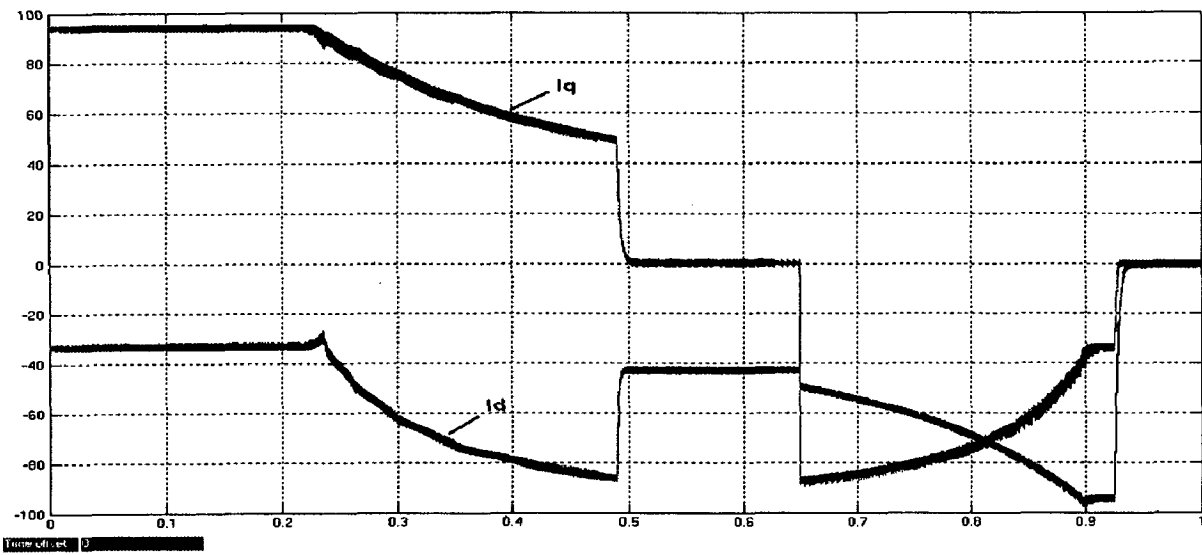
(c) Change in Iq and Id
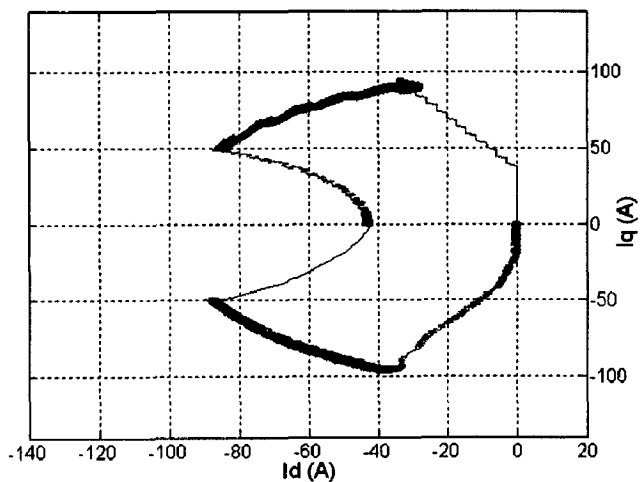
q, d current loci of simulation
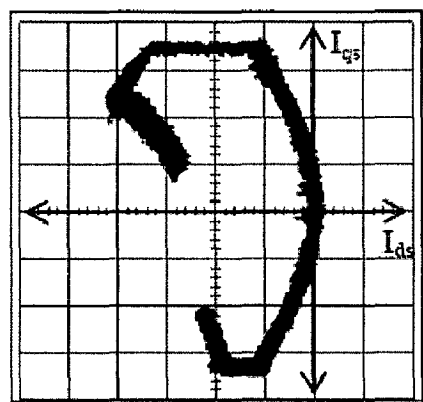
q, d current loci from reference [25]

(e) q, d current loci

Fig. 5.15 Dynamic performance of drive in 3rd and 4th quadrant

From the above figures, it is observed that the theoretical prediction and results with the literature [25, 26, 30] compare favourably, thus verifying that the model and computer simulations program used in this investigation is valid for the machine used.

Chapter 6

Conclusions and Future Work

6.1 Conclusions

The Master's thesis addressed the dimensioning of an electric drive for an electric vehicle. The work is mainly focused on a design of permanent magnet synchronous motor, the design verifications with finite element method and simulation of drives and control with constant torque and flux-weakening region.

The PMSM is designed using analytical software tool, based on existing induction motor stator geometry. The PMSM rotor configuration considered is IPM-spoke type, which is expected to be superior over the SPM. Analytical software is also useful to simulate the machine and drive's static and dynamic behaviour.

Finite element method results give finer variation of flux density in airgap, where slotting and saturation effects are taken in to account. Torque and inductance values are calculated with FEM for different loading conditions, this can be useful to model the machine more precise.

The analytical and FEM tools are interlinked allowing to calculate the same machine in both tools from the same input file. For iterative process and time domain simulation, it is also necessary to interlink with some script, so Matlab is used as the application manager. The modelled parameters of machine are compared. Both results coincide well also with measured values and more thoroughly measurements are still undertaking. The proposed current regulation control algorithm provides drives to operate in constant torque and flux-weakening region with optimum current, which enables drive to operate for EVs. The control adjusts the q- and d-axis current command based on commanded torque considering speed and dc link voltage. Time domain simulation of the behaviour of the drive including inverter with control algorithm is carried out in Matlab/Simulink. The simulations results show the system with such control system can work well and fulfils the targets.

6.2 Future Work

The work presented in this Master's thesis, while promising for a good design of PMSM Drives for EVs, is certainly far from complete. Implementation of the new control strategies must be demonstrated in a physical system in order to fully prove the concepts. Experimental results for the different design and control are given in literature [12, 15, 25-27]. Finally, application to electric vehicles must also be demonstrated.

In order to achieve the best overall drive performance, the proposed control strategy presented in this thesis should be implemented together. However, the initial design also needs to verify with practical machine with all parameters on test bench. The results, from finite element method considering mechanical and thermal effect, also need to compare with physical motor and the model in FEM can be improved with comparison of actual parameters. The primary design simply gives design without considering the thermal effects, where thermal effect also need to take in account with parameter variation and magnet magnetization change with temperature. This will involve a mathematically rigorous study of the steady state and transient behaviour of machine in all different condition.

All the concepts and simulation results given of the drive and control in this thesis were the results of a continuous time domain implementation. In the physical implementation, all of the control will be realized in a digital signal processor. For this reason, discrete time domain implementation of the control strategies should tested in simulations in order to better predict the physical system performance.

Appendix A

Stator and Rotor Steel property:

Steel name: M330-35A

Bs = 1.0000 T;   H@1T = 111.0864 A/m   Density = 7650 kg/m³

Iron-Loss coefficients, W/lb

CfCh = 0.0085; Cfa = 1.308; Cfb = 0.356; CfCe = 2.64E-6

B/H curve

B (T)	H (A/m)	B (T)	H (A/m)
0.0000	0.000	1.1000	156.000
0.1000	29.100	1.2000	211.000
0.2000	39.900	1.3000	342.000
0.3000	47.900	1.4000	785.000
0.4000	55.000	1.5000	2198.000
0.5000	62.200	1.6000	4779.000
0.6000	70.100	1.7000	8466.000
0.7000	79.200	1.733	10000.000
0.8000	90.300	1.797	13328.000
0.9000	105.000	1.825	15000.000
1.0000	125.000	1.888	20000.000

Magnet Property:

Magnet Type: HF 28/26

Remanent flux density, Br	0.38 T
Intrinsic coercivity, Hcj	2.70E+05 A/m
Relative recoil permeability, Murec	1.1642
Temperature coefficient for remanent flux density, Cbr	-0.20 %/^{0}C
Temperature coefficient for intrinsic coercivity, CHcj	0.40 %/^{0}C
Density, DMag	4800.00 kg/m³

Appendix B

Design Sheet:

PC-BDC 6.5 for Windows (6.5.2.8)
E:\S-User\S-Siddhapura\SPPED information\speed prog\spoke\spoke_mate_chg_HF.bd4
Universität Stuttgart
PC-BDC main title
PC-BDC sub-title

```
1 Dimensions:------------------------------------------------------------
```

RotType	Spoke		Embed	Not		Poles	8	
Stator..								
StatorOD	240.000	mm	LamShape	Circle		Slots .	48	
SYoke	12.500	mm	ASD	22.500	mm	SP	6.000	
Rad3	120.000	mm	Rad2	107.500	mm	S-Slot	Flared	
TWS	6.152	mm	SD	22.500	mm	SO	2.300	mm
TGD	0.650	mm	SOang	55.000	mDeg	SWIT	2.300	mm
filSB	1.200	mm	filSO	2.760	mm	Stf	0.970	
Rotor..								
MOH	0.000	mm				Skew	1.600	
RotorOD	168.000	mm	Rad1	84.000	mm	Gap	1.000	mm
LM	12.000	mm	BetaM	147.231	eDeg	pupa	0.818	
RYoke	23.579	mm				RadSH	10.000	mm
Inset	7.685	mm	MagWid	45.000	mm			
DHub	62.058	mm	wNeck	12.716	mm	MslotWid	52.685	mm
MEdge	12.000	mm	LM_min	12.000	mm	dGap	0.000	mm
Slits	None							
wMag	45.000	mm						
Lstk	200.000	mm	Lrotor	200.000	mm	Lstator	201.000	mm

```
2 Magnet Data:----------------------------------------------------------
```

Magnet	HF 28/26							
Br	0.380	T	Hc	270.000	kA/m	MuRec	1.164	
CBr	-0.200	%/DegC	CHc	0.400	%/DegC	DMag	4800.000	kg/m3
BrT	0.383	T	HcT	265.680	kA/m			
Nuisance	0.000	mm	BrTnu	0.383	T	MuRecnu	1.164	

```
3 Control Data:---------------------------------------------------------
```

RPM	750.000	rpm	Vs	500.000	V	Drive	Sine	
ISP	100.000	A	gamma	0.000	deg	Sw_Ctl	ISP_HB	
HBA_act	ISP/8		HB%	12.500		HBtype	Constant	
FixfChop	Yes		fChop	0.000	kHz	fChopAct	2.800	kHz
EMFCalc	BLV/UnBal		dq0	true				
Vq	0.000	V	Rq	0.000	ohm	Vd	0.600	V
t_q	0.000	us				Freq1	50.000	Hz
ISP_Act	100.000	A	Tol_Act	ISP/8		ISLA_Act	1/32	

```
4 Winding Data:---------------------------------------------------------
```

Connex	Wye							
WdgType	Custom							
Offset	4		CPP	1.000				
Tph	32.000		PPATHS	1		SPP	2.000	
Layers	1.000		CSidesPh	16		Z	192.000	
MLT	637.144	mm	LgthOEnd	289.330	mm	Ext	1.000	mm
EndFill	0.500		LaxPack	247.529	mm	Liner	0.200	mm
WireSpec	BareDia		Wire	0.733				
NSH	32		WireDia	0.733	mm	InsThick	1.000E-02	mm
SFg	0.389		SFn	0.567		MaxSFn	0.567	

Aslot	138.649	mm^2	ASlotLL	127.909	mm^2	ACond	13.485	mm^2
GPAslot	140.144	mm^2	ATstick	8.929	mm^2	TopStick	false	
TwjWid	2.000	mm	TwjLeg	3.500	mm	TwjThk	0.000	mm
PhsWid	2.000	mm	PhsLeg	3.500	mm	PhsThk	0.000	mm
ATwj	0.000	mm^2	APhs	0.000	mm^2			
XET	1.000		ETCalc	BDC 6.0		Rext	0.000	ohm
Nse	38.215		X_R	1.000		Axl	54.750	mDeg
T_Wdg	25.000	DegC	Rph0	0.027	ohm	R_LL	0.053	ohm
T_c	20.000	DegC	Rph	0.026	ohm/ph	TFRho	1.000	

Inductances...

SalientP	true		LSlot	0.124	mH	Lendt	0.120	mH
XL	1.000		MSlot	0.000	mH	LDiff	0.119	mH
Lsigma	0.364	mH	Msigma	0.123	mH	XLdiff	1.000	
Lgg	1.663	mH	Mgg	0.000	mH	PCSlot	1.930	
LL_d	1.952	mH	LL_q	3.252	mH	LL0	2.602	mH
Lg_0	0.707	mH	Lg_2	-0.217	mH	Laa_d	0.854	mH
Ld	0.976	mH	Lq	1.626	mH	Laa_q	1.287	mH
Xd	0.307	ohm/ph	Xq	0.511	ohm/ph	Xsigma	0.076	ohm/ph
XCd	1.000		XCq	1.000		Lext	0.000	mH
Gd	0.343		Gq	0.646		XLendt	1.000	
kw1	0.938		Xm0	0.674	ohm/ph			
Ks1	0.971		kp1	1.000		kd1	1.000	
ksg	0.856		fz	1.005		PSSlot	S-Closed	
Saliency	Auto		CalcLdLq	Auto		muPlug	1.000	
il_Ang	65.236	A	i2_Ang	38.636	A	i3_Ang	-103.872	A

4b Unbalanced Winding Data:---

Ax1ED	0.000	eDeg	Ax2ED	120.000	eDeg	Ax3ED	240.000	eDeg
UnB.rms	0.000							
MLT1	637.144	mm	MLT2	637.144	mm	MLT3	637.144	mm
Tph1	32.000		Tph2	32.000		Tph3	32.000	
Rph1	0.027	ohm/ph	Rph2	0.027	ohm/ph	Rph3	0.027	ohm/ph
RTermAB	0.053	ohm	RTermBC	0.053	ohm	RTermBC	0.053	ohm
LTermAB	2.362	mH	LTermBC	2.362	mH	LTermBC	2.362	mH
LSlot1	0.124	mH	LSlot2	0.124	mH	LSlot3	0.124	mH
MSlot12	0.000	mH	MSlot23	0.000	mH	MSlot31	0.000	mH
Lg1	0.826	mH	Lg2	0.826	mH	Lg3	0.826	mH
Mg12	-0.231	mH	Mg23	-0.231	mH	Mg31	-0.231	mH
Lendt1	0.000	mH	Lendt2	0.000	mH	Lendt3	0.000	mH
Lph1	0.950	mH	Lph2	0.950	mH	Lph3	0.950	mH
Mph12	-0.231	mH	Mph23	-0.231	mH	Mph31	-0.231	mH

5 Magnetic Circuit Design:--

T_Mag	25.000	DegC	T_r	16.000	DegC	XBrT	1.000	
BrT	0.383	T	BgOC	0.446	T	Hca	261.822	kA/m
BgAvOC	0.364	T	PhiG	4.834	mWb	BgA/BgOC	0.817	
Bg1OC	0.541	T	PhiM1	4.573	mWb	Bg1/BgOC	1.214	
BmOC	0.290	T	Bm/BrT	0.757		XBtpk	1.000	
HmOC	-63.670	kA/m	Hm/HcT	-0.240		PC	3.623	
Bst	0.821	T	Bsy	0.997	T	Bry	0.513	T
XTw	0.000		XSYoke	0.000		XRYoke	0.000	
kT	0.823	Nm/A	kE	0.956	Vs/Rad	krpmNL	5.537	krpm
kSat	1.000		XSatn	1.000		CalcSatn	Fixed	
SatnTol	0.000							
Xks	0.000		ks	0.000		XTTarc	1.000	
EffWst	6.152	mm	EffLst	18.409	mm	ukCL	0.000	
XBgap	1.000		X_EMF	1.000		k_rpf	1.000	
eLLpk	75.088	V	eTmax	0.541	V	Bslot	9.279E-05	T
IBk	196.371	A	Bk	0.000	T	Hk	-261.822	kA/m
ILR	9591.142	A	BmLR	-16.145	T	HmLR	-1.13E+04	kA/m
IC180	11031.493	A	BmC180	-18.620	T	HmC180	-1.30E+04	kA/m

BHmag	18.457 kJ/m3	Carter	1.070		Xrm	0.500	
Amhp	9000.000 mm^2	Aghp	5428.419 mm^2		Rghp	1.501E+05 At/Wb	
PmO	2.194 uWb/At	Xrl	1.000		prl	0.241	
apEnd	1.000	Pend	0.047		Lme	6.000 mm	
u_LKG	0.000	f_Lkg	0.926		if_Lkg	1.079	
Fringing	ON	XFringe	1.000		XBetaM	1.000	

7 Dynamic design (time-stepping simulation):------------------------------------

OpMode	Motoring	Vs	500.000 V	RPM	750.000 rpm	
Tshaft	82.165 Nm	Pshaft	6453.206 W	Eff	93.823 %	
WCu	394.522 W	WFe	30.363 W	WWF	0.000 W	
WCan	0.000 W	WMagnet	0.000 W	WShaft	0.000 W	
WTotal	424.885 W	TempRise	0.000 DegC	Jrms	5.267 A/mm^2	
IWpk	107.482 A	IWav	63.972 A	IWrms	71.030 A	
ILpk	107.482 A	ILav	63.975 A	ILrms	71.032 A	
IQchpk	108.081 A	IQchav	18.391 A	IQchrm	38.915 A	
IQcmpk	108.081 A	IQcmav	18.391 A	IQcmrm	38.915 A	
IDchpk	108.056 A	IDchav	13.636 A	IDchrm	31.863 A	
IDcmpk	108.056 A	IDcmav	13.636 A	IDcmrm	31.863 A	
IDC_W	14.266 A	WConv	49.089 W	EffDCSh	93.158 %	
IDC_P	13.854 A	WSwitch	0.000 W	Pelec	6878.092 W	
Tgap	82.551 Nm	Tei	82.572 Nm	Trel	-0.020 Nm	
Tloop	82.517 Nm	WFeCalc	OC	CalcVwfm	None	
V1rms	0.000 V	I1rms	70.932 A	phi_1	-0.189 deg	
phV1	90.000 deg	phI1	90.189 deg	phEq1	90.247 deg	
V1d	0.000 V	I1d	-0.233 A			
V1q	0.000 V	I1q	70.710 A			

8 Steady-State Thermal Model:---

TempCalc	DegCW	FixTMag	IterX	Ambient	20.000 DegC	
DegCW	0.000 degC/W	HTCcyl	0.000 W/m2/C	HTCend	0.000 W/m2/C	
TempRise	0.000 DegC	T_c	20.000 DegC	T_r	16.000 DegC	
T_f	20.000 DegC	T_y	20.000 DegC	HeatFlux	1.244 kW/m^2	
SlotPeri	51.401 mm	Liner	0.200 mm	ct_Liner	0.200 W/mC	
SSArea	10280.284 mm^2	C_motor	28.172 kJ/C	ThRSlot	2.027E-03 C/W	
FSArea	3.416E+05 mm^2	ThermTC	0.000 min	R_fa	0.000 C/W	

9 Miscellaneous:--

Weights...

wt_Cu	7.333 kg	wt_Fe	43.930 kg	wt_Mag	4.147 kg	
wt_Tot	55.410 kg	wt_Shaft	0.842 kg	wt_Frame	3.321 kg	
wt_FeS	22.949 kg	wt_FeR	20.981 kg	wt_RSS	33.535 kg	

Inertia components...

RotJ	0.101 kg-m2	RotJSS	0.117 kg-m2	RotJSh	4.210E-05 kg-m2	
RotJFe	0.088 kg-m2	RotJMag	0.013 kg-m2	LShaft	350.000 mm	
sigma	1.350 psi					
Wf0	0.000 W	RPM0	1000.000 rpm	NWFT	1.000	
Fringing	ON	XFringe	1.000	NHx	21	
CanStyle	None					
Ecc	0.000	UMPavg	-3.47E-14 kg	UMPmax	-7.11E-15 kg	
TRFrms	18.372 kg	TRFavg	16.321 kg	TRFmax	23.454 kg	
CForce	113.635 kg			LamThk	0.500 mm	
NLams	388	pcLam	3.000 %	RFei	1.000E+06	

10 Core loss analysis:---

WFeCalc	OC	LossFE	Mech	XFe	1.000
DFekgS	7480.246 kg/m^3	St.Steel	M19 3% Si		
DFekgR	7480.246 kg/m^3	Ro.Steel	M19 3% Si		
DFekgSh	7656.829 kg/m^3	Sh.Steel	shaft-bh		

```
wt_Teeth       9.984 kg      wt_Yoke      12.965 kg      wt_Troot      2.678 kg
Specific core losses...
cFe_E50        0.646 W/kg     cFe_H50       1.976 W/kg    cFe_50        2.621 W/kg
cFe_E_F        0.646 W/kg     cFe_H_F       1.976 W/kg    cFe_F         2.621 W/kg
cFe_T_E        0.473 W/kg     cFe_T_H       0.683 W/kg    cFe_T         1.155 W/kg
cFe_Y_E        0.283 W/kg     cFe_Y_H       0.931 W/kg    cFe_Y         1.214 W/kg
Core loss analysis...
WFe_T_E        5.986 W        WFe_T_H       8.643 W       WFe_T        14.629 W
WFe_Y_E        3.663 W        WFe_Y_H      12.071 W       WFe_Y        15.734 W
```

Appendix C

Experimental Setup:

A picture of the prototype PMSM is shown in Fig. A-01. The PMSM is coupled with DC machine and both machines are controlled through individual drives. A torque and speed sensors are used for each drive for feedback.
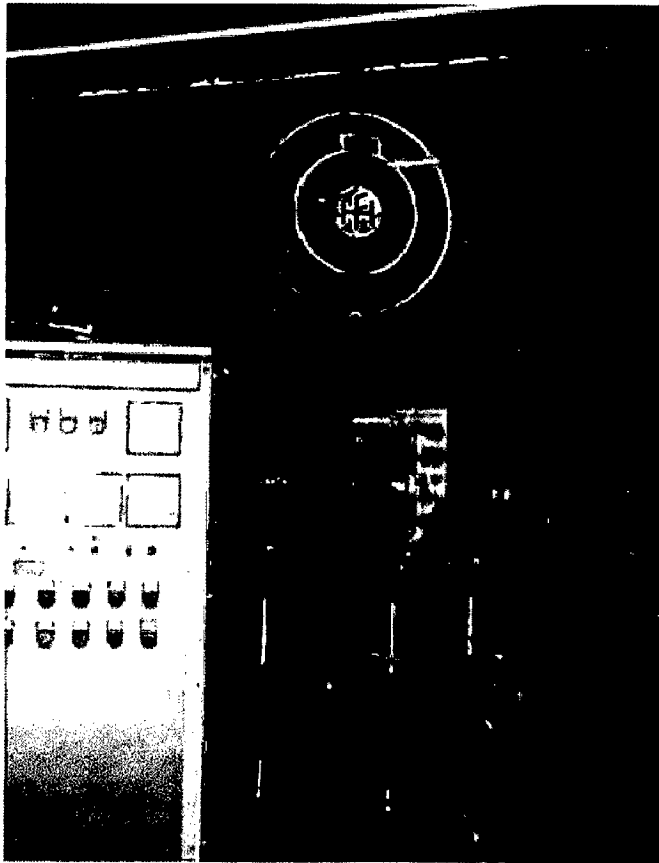
Fig. A-01 Prototype PMSM drive with experimental setup

Determination of q and d reactances:

The parameter of PMSM has been determined without measurement of rotor position sensors [36]. The test procedure adopted here is basically combination of a no-load and a load test. The reading of each tests and calculated parameter for each tests in givent in tables below.

Reading of induced voltage for different speed:

Table A-01

Vtrms (V)	Vpp (V)	Freq. (Hz)
11.28	28.32	20.10
16.75	41.96	29.83
22.78	57.01	40.60
25.54	63.86	45.60
28.41	70.01	50.60
31.77	79.40	56.80
38.74	96.80	69.04
50.18	125.43	89.64
55.19	137.96	98.50
73.07	182.71	130.17
84.23	210.53	150.39

No load test:

Table A-02

No load readings: Freq: 50.025 Hz, Erms: 28.41V, EppL: 70.01V

Sr. No.	Vrms V	Vpp V	Irms A	P1 kW	Qv kVAR
01	31.69	83.60	12.55	0.110	0.380
02	33.13	88.46	16.80	0.12	0.540
03	35.09	94.6	23.30	0.16	0.804
04	36.62	100	27.60	0.187	0.996
05	39.62	109	36.91	0.24	1.445
06	40.71	113.5	40.8	0.26	1.64
07	42.81	120	47.06	0.303	1.992
08	45.72	128.3	56.3	0.327	2.561
09	46.6	131.6	59.9	0.339	2.77
10	47.39	135.6	61.4	0.35	2.88
11	50.55	142.5	74.5	0.492	3.74

Calculation on Table A-02:

Table A-03

Sr. No.	Vrms V	Irms A	P1 kW	Qv kVAR	Θ°	Xd Ω	Ld mH
01	31.69	12.55	0.110	0.380	72.5424	0.2614	0.8319
02	33.13	16.80	0.12	0.540	75.5225	0.2810	0.8943
03	35.09	23.30	0.16	0.804	79.0472	0.2867	0.9126
04	36.62	27.60	0.187	0.996	79.6302	0.2975	0.9469
05	39.62	36.91	0.24	1.445	80.5609	0.3037	0.9667
06	40.71	40.8	0.26	1.64	80.8511	0.3015	0.9596
07	42.81	47.06	0.303	1.992	81.3151	0.3060	0.9740
08	45.72	56.3	0.327	2.561	82.7037	0.3075	0.9787
09	46.6	59.9	0.339	2.77	83.0502	0.3037	0.9666
10	47.39	61.4	0.35	2.88	83.1656	0.3091	0.9840
11	50.55	74.5	0.492	3.74	82.5304	0.2972	0.9460
						Xd=0.2959	**Ld=0.9419**

Load test:

Table A-04

Sr. No.	Vrms V	Irms A	P1 kW	Qv kVAR	Torque (N.m)	Xq Ω	Lq mH	Θ°	δ°	(Θ- δ) °
01	40.8	42.51	0.773	1.56	25	0.49532	1.5766	63.4601	20.4039	43.0562
02	40.8	43.93	0.98	1.503	30	0.50551	1.6091	56.8053	26.6948	30.1105
03	40.8	45.31	1.115	1.469	35	0.50889	1.6198	52.8189	30.3483	22.4706
04	40.8	46.95	1.244	1.444	40	0.51311	1.6333	49.1003	33.8981	15.2022
05	40.8	49.0	1.37	1.43	45	0.50977	1.6227	46.2178	36.5450	9.6728
06	40.8	51.5	1.52	1.41	50	0.51097	1.6265	43.0491	39.8809	3.1682
07	40.8	54.36	1.66	1.42	55	0.5099	1.6231	40.4062	42.9261	-2.5199
08	40.8	57.42	1.80	1.43	60	0.50473	1.6066	38.5000	45.3947	-6.895
09	40.8	60.6	1.91	1.47	65	0.48633	1.548	37.8839	46.3230	-8.439
10	40.8	64.12	2.04	1.512	70	0.48027	1.5288	36.5681	48.6901	-12.122
						0.50248	**1.5994**			

88

References

01   J.R. Hendershot Jr., TJE Miller, "Design of Brushless Permanent-Magnet Motors", Oxford Science Publications, New York, 1994.

02   TJE Miller, "Brushless Permanent-Magnet and Reluctance Motor Drives", Oxford Science Publications, New York, 1989.

03   B.K. Bose, "Power Electronic and Variable Frequency Drives: Technology and Applications", IEEE Press, New York, 1996.

04   Jacek F. Gieras, Mitchell Wing, "Permanent Magnet Motor Technology: Design and Applications", Marcel Dekker, Inc, New York, 1997.

05   P.C. Krause, Oleg Wasynczuk and S.D. Sudhoff, "Analysis of Electric Machinery and Drive Systems", IEEE press, Willey-Interscience Publication, 2002.

06   Sheppard J. Salon, "Finite Element Analysis of Electrical Machines", Kluwer Academic Publishers, Boston, 1995.

07   A.B.J. Reece, T.W. Preston, "Finite Element Methods in Electrical Power Engineering", Oxford Science Publications, New York, 2000.

08   Peter P. Silvester, Ronald L. Ferrari, "Finite Elements for Electrical Engineers", Cambridge University Press, Cambridge, 1996.

09   TJE Miller, "SPEED's Electric Motors", SPEED Laboratory, University of Glasgow, 2004.

10   P. Vas, "Vector Control of AC Machines", Oxford Science Publications, New York, 1990.

11   P. Pillay and R. Krishnan, "Application Characteristics of Permanent Magnet Synchronous and Brushless dc Motors for Servo Drives", *IEEE Transactions on Industry Applicat.*, Vol. 27, No. 5,Sept./Oct. 1991, pp. 986-996.

12   T.J.E. Miller, M. Popescu, C. Cossar, M. McGilp, J.A. Walker, "Calculating the interior-permanent-magnet motor", *IEEE International Electric Machines and Drives Conference (IEMDC'03)*, Vol. 2, pp.1181–1187, 1-4 June 2003.

13   G.R. Slemon, "On the design of high performance of PM motors", *Conference Record of the 1992 Industry Applications Society Annual Meeting*, Vol.1, pp. 279–

285, 4-9 Oct. 1992.

14   Longya Xu, Lurong Ye and Ahmed El-Antably, "A New Design Concept of Permanent Magnet Machine for Flux Weakening Operation", *IEEE Transactions on Industry Applicat.*, Vol. 31, No. 2, March/April 1995, pp. 373 - 378.

15   Yong Li, Jibin Zou and Yongping Lu, "Optimum Design of Magnet Shape in Permanent –Magnet Synchronous Motors", *IEEE Transactions on Magnetics,* Vol. 39, No. 6, November 2003, pp. 3523-3526.

16   N. Bianchi and S. Bolognani, "Unified Approach to the Analysis and Design of an AC Motor Drive for Flux-Weakening Operation", *The 1998 IEEE 33rd IAS Annual Meeting,* Vol. 1, 12-15 Oct. 1998, pp. 95 – 102.

17   W.L. Soong and TJE Miller, "Field-Weakening performance of brushless synchronous AC motor drives", *IEE Proc.-Electr. Power Appl.*, Vol.141, no.6, November 1994, pp. 331-340.

18   Gyu-Hong Kang, et al, "Improved Parameter Modeling of Interior Permanent Magnet Synchronous Motor Based on Finite Element Analysis", *IEEE Transactions on Magnetics*, Vol. 36, No. 4, July 2000, pp. 1867-1870.

19   M.A. Jabbar, H.N. Phyu, Z. Liu and C. Bi, "Modeling and Numerical Simulation of a Brushless Permanent-Magnet DC Motor in Dynamic Conditions by Time-Stepping Technique", *IEEE Transactions on Ind. Applicat.,* Vol. 40, No. 3, May/June 2004, pp. 763-770.

20   M.A. Jabbar, Z. Liu and J. Dong, "Time-Stepping Finite-Element Analysis for the Dynamic Performance of a Permanent Magnet Synchronous Motor", *IEEE Transactions on Magnetics,* Vol. 39, No. 5, September 2003, pp. 2621-2523.

21   Yong Wang, K. T. Chau, C. C. Chan and J. Z. Jiang, "Transient Analysis of a New Outer-Rotor Permanent-Magnet Brushless DC Drive Using Circuit-Field-Torque Coupled Time-Stepping Finite-Element Method", *IEEE Transactions on Magnetics,* Vol. 38, No. 2, March 2002, pp. 1297-1300.

22   Jinyun Gan, K. T. Chau, Yong Wang, C. C. Chan and J. Z. Jiang, "Design and Analysis of a New Permanent Magnet Brushless DC Machine", *IEEE Transactions on Magnetics,* Vol. 36, No. 5, March 2000, pp. 3353-3356.

23   S. L. Ho, H. L. Li, W. N. Fu, and H. C. Wong, "A Novel Approach to Circuit-

Field-Torque Coupled Time Stepping Finite Element Modeling of Electric Machines", *IEEE Transactions on Magnetics,* Vol. 36, No. 4, July 2000, pp. 1886-1889.

24   S. L. Ho, W. N. Fu, H. L. Li, H. C. Wong, and H. Tan, "Performance Analysis of Brushless DC Motors Including Features of the Control Loop in the Finite Element Modeling", *IEEE Transactions on Magnetics,* Vol. 37, No. 5, September 2001, pp. 3370-3374.

25   G. Gallegos-Lopez, F.S. Gunawan and James E. Walters, "Optimum Torque Control of Permanent Magnet AC Machines in the Field-Weakened Region", *Conference Record of the 2004 IEEE 39th IAS Annual Meeting,* Vol. 1, pp. 254-260, 3-7 Oct. 2004.

26   Bon-Ho Bae, N. Patel, Steven Schulz and Seung-Ki Sul, "New Field Weakening Technique for High Saliency Interior Permanent Magnet Motor", *Conference Record of the 38th IAS Annual Meeting,* Vol. 2, pp. 898 – 905, 12-16 Oct. 2003.

27   B.K. Bose, "A High-Performance Inverter-Fed Drive System of an Interior Permanent Magnet Synchronous Machine", *IEEE Transactions on Ind. Applicat.,* Vol. 24, No. 6, Nov./Dec. 1988, pp. 987-997.

28   P. Pillay and R. Krishnan, "Modeling, Simulation, and Analysis of Permanent-Magnet Motor Drives, Part II: The Brushless DC Motor Drive", *IEEE Transactions on Ind. Applicat.,* Vol. 25, No. 2, March/April 1989, pp. 265-273.

29   Jang-Mok Kim and Seung-Ki Sul, "Speed Control of Interior Permanent Magnet Synchronous Motor Drive for the Flux Weakening Operation", *IEEE Transactions on Ind. Applicat.,* Vol. 33, No. 1, Jan./Feb. 1997, pp. 43-48.

30   M.F. Rahman, L. Zhong and K.W. Lim, "A DSP Based Instantaneous Torque Control Strategy for Interior Permanent Magnet Synchronous Motor Drive with Wide Speed Range and Reduced Torque Ripples", *Conference Record of the 1996 IEEE 31st IAS Annual Meeting, IAS '96,* Vol. 1, pp. 518-524, 6-10 Oct. 1996.

31   Z.Q. Zhu, Y.F. Shi and D. Howe, "Influence of DSP controller on performance of a permanent magnet brushless AC drive in flux-weakening mode", Journal of Zhejiang University of Science, 2005 6A(2) : 83-89.

32   S. Marimoto, Y. Takeda, T. Hirasa and K. Tanigughi, "Expansion of Operating

Limit for Permanent Magnet by Current Vector Control Considering Inverter Capacity", *IEEE Transactions on Ind. Applicat.*, Vol. 26, No. 5, Sept./Oct. 1990, pp. 866-871.

33   M. Kadjoudj, M.E.H. Benbouzid, C. Ghennai and D. Diallo, "A Robust Hybrid Current Control for Permanent-Magnet Synchronous Motor Drive", *IEEE Transactions on Energy Conversion,* Vol. 19, No. 1, March 2004, pp. 109-115.

34   User's Manual for PC-BDC 6.5 - PM Brushless Design Simulation Software, SPEED Laboratory, University of Glasgow, 2004.

35   ANSYS reference manual

36   Hans-Peter Nee, Louis Lefevre, Peter Thelin, and Juliette Soulard, "Determination of *d* and *q* Reactances of Permanent-Magnet Synchronous Motors Without Measurements of the Rotor Position", *IEEE Transactions on Ind. Applicat.,* Vol. 36, No. 5, Sept./Oct. 2000, pp. 1339-1335.

37   Nathan Ida, Joao P.A.Bastos, "Electromagnetics and Calculation of Fields", Spinger-Verlag, 1992.

38   B. Kattentidt, "Entwicklung eines elektrischen Antriebssystems mit Brennstoffzelle für Personenkraftwagen", Ph.D. thesis at the University of Stuttgart, 2003.